ISTANBUL TECHNICAL UNIVERSITY ★ GRADUATE SCHOOL

INVESTIGATING THE OXIDATION AND HIGH TEMPERATURE WEAR BEHAVIOUR OF HOT-DIP ALUMINIZED AND DIFFUSION ANNEALED INCONEL 718 SUPERALLOY

M.Sc. THESIS

Ahmet KAVUKCU

Department of Metallurgy and Materials Engineering

Materials Engineering Programme

AUGUST 2021

ISTANBUL TECHNICAL UNIVERSITY ★ GRADUATE SCHOOL

INVESTIGATING THE OXIDATION AND HIGH TEMPERATURE WEAR BEHAVIOUR OF HOT-DIP ALUMINIZED AND DIFFUSION ANNEALED INCONEL 718 SUPERALLOY

M.Sc. THESIS

Ahmet KAVUKCU
(506181401)

Department of Metallurgy and Materials Engineering

Materials Engineering Programme

Thesis Advisor: Prof. Dr. Murat BAYDOĞAN

AUGUST 2021

İSTANBUL TEKNİK ÜNİVERSİTESİ ★ LİSANSÜSTÜ EĞİTİM ENSTİTÜSÜ

SICAK DALDIRMA ALÜMİNYUM KAPLAMA VE DİFÜZYON TAVLAMASI UYGULANMIŞ INCONEL 718 SÜPERALAŞIMININ OKSİDASYON VE YÜKSEK SICAKLIK AŞINMA DAVRANIŞININ İNCELENMESİ

YÜKSEK LİSANS TEZİ

Ahmet KAVUKCU
(506181401)

Metalurji ve Malzeme Mühendisliği Anabilim Dalı

Malzeme Mühendisliği Programı

Tez Danışmanı: Prof. Dr. Murat BAYDOĞAN

AĞUSTOS 2021

Ahmet KAVUKCU, a M.Sc. student of İTU Graduate School student ID 506181401, successfully defended the thesis/dissertation entitled “INVESTIGATING THE OXIDATION AND HIGH TEMPERATURE WEAR BEHAVIOUR OF HOT-DIP ALUMINIZED AND DIFFUSION ANNEALED INCONEL 718 SUPERALLOY”, which he prepared after fulfilling the requirements specified in the associated legislations, before the jury whose signatures are below.

Thesis Advisor : **Prof. Dr. Murat BAYDOĞAN** ....
Istanbul Technical University

Jury Members : **Prof. Dr. Hüseyin ÇİMENOĞLU** ....
Istanbul Technical University

Assoc. Prof. Dr. Cem KAHRUMAN ....
Bursa Technical University

Date of Submission : 10 June 2021
Date of Defense : 17 August 2021

To my family and friends,

FOREWORD

First of all, I would like to thank Prof. Dr. Murat BAYDOĞAN who has always answered my questions, supported me, guided through my studies and showed me alternative solutions.

I also would like to thank Prof. Dr. Hüseyin ÇİMENOĞLU for his guidance and valuable suggestions to complete the study of this thesis.

Additionally, I am also thankful to Lectrurer Dr. Faiz MUHAFFEL for his limitless help and Research Assistant Mertcan KABA for his proactive effort and Research Assistant Doğukan ÇETİNER for sharing his experiences.

I would like to express my gratitude to Prof. Dr. Bogdan Rutkowski for his contribution about oxidation test experiments.

I want to thank to İTÜ BAP office for the contribution to my thesis with a project number of MYL-2020-42731.

I could not pass without giving my thanks to Assoc. Prof. Kemal KORKMAZ, Asst. Prof. Kerem Özgür GÜNDÜZ and Ahmet NAZIM.

Also, I want to give my thanks to my friends especially for Mustafa BELLEK.

Finally, I want to present my thanks to my parents Erdoğan KAVUKCU and İnci KAVUKCU for their humble patience and encouragement.

June 2021

Ahmet KAVUKCU
(Metallurgical and Materials Engineer)

TABLE OF CONTENTS

Page

ABBREVIATIONS

APS	: Atmospheric Plasma Spraying
BCT	: Body Centered Tetragonal
CVD	: Chemical Vapor Deposition
EB-PVD	: Electron Beam Physical Vapor Deposition
EDS	: Energy-dispersive X-ray spectroscopy
FCC	: Face Centered Cubic
GCP	: Geometrically Close-Packed
HAPC	: Halide Activated Pack Cementation
HCP	: Hexagonal Close-Packed
HDA	: Hot-Dip Aluminizing/ Aluminized
HDA+DA	: Hot-Dip Aluminizing/ Aluminized plus Diffusion Annealed
HVOF	: High Velocity Oxy Fuel
IDZ	: Inter Diffusion Zone
LPPS	: Low Pressure Plasma Spraying
PVD	: Physical Vapor Deposition
SEM	: Scanning Electron Microscope
TBC	: Thermal Barrier Coatings
TCP	: Topologically Close-Packed
TGO	: Thermally Grown Oxides
VPS	: Vacuum Plasma Spraying
XRD	: X-Ray Diffraction
YSZ	: Yttria Stabilized Zirconia

LIST OF TABLES

Page

LIST OF FIGURES

Page

INVESTIGATING THE OXIDATION AND HIGH TEMPERATURE WEAR BEHAVIOUR OF HOT-DIP ALUMINIZED AND DIFFUSION ANNEALED INCONEL 718 SUPERALLOY

SUMMARY

Superalloys are quite superior materials that are used in wide range of application fields which have critical importance such as aviation, aerospace, nuclear energy industries. Nickel based superalloys, as a type of superalloy, has advantages of both mechanical strength and oxidation resistance at high temperature. Inconel 718 is nickel-based superalloys that is employable for in hot section of aircraft and steam turbines parts.

One of the main characteristics of Inconel 718 is precipitation strengthened superalloy with γ''-Ni_3Nb phases and utilizable up to 650°C. Additionally, oxidation and corrosion resistance are provided by Chromium that has capability to form protective oxide layer for Inconel 718. On the other hand, above 650°C γ'' phases starts to dissolve and transform detrimental δ phases. Another inevitable limitation of Inconel 718 is protective Cr_2O_3 layer has tendency to transform volatile CrO_3 compound above 1000°C. These kinds of limitation increased coating demand to fulfill requirements such as wear and oxidation resistance. One of the high temperature coating called diffusion coating is attentively applicable for nickel-based superalloy. Hot-dip aluminizing process has numerous advantages such as low cost, easy to apply as well as promoting formation of nickel-aluminides. Nickel-aluminides provides reservoir for aluminum against oxidation and mechanical strength in form of γ'- (Ni_3Al) that is coherent with matrix.

In the open literature, wear behavior studies of different high temperature coatings for Inconel series were commonly located. In particular, the majority of studies focuses on the overlay and thermal barrier coatings, nevertheless, these studies on the wear behaviors of coated Inconel series have not satisfactorily fill lack of literature. Therefore high temperature tribological and oxidation behavior of hot-dip aluminized Inconel 718 were detailly investigated to contribute literature.

In this study, Inconel 718 samples are aluminized at 700°C for 2 minutes by hot-dipping then, some of aluminized sample were subjected to diffusion annealing at 700°C for 10 hours. Wear tests for bare, hot-dip aluminized, hot-dip aluminized and diffusion annealed Inconel 718 samples were performed at 25°C,300°C and 600°C in order to investigate high temperature tribological behavior. Additionally, to determine oxidation behavior of bare, hot-dip aluminized, hot-dip aluminized and diffusion annealed Inconel 718 specimens were subjected to isothermal oxidation tests at 800°C for 100 and 300 hours. Structural analyses were done by using scanning electron microscope, energy dispersive spectroscopy and X-ray diffractometer.

Results has revealed that the wear rate of the hot-dip aluminized and diffusion annealed samples were found to be three times less than only hot-dip aluminized samples for wear test at room temperature. Diffusion annealing became more

necessary after hot-dip aluminizing process according to wear test at 300°C and 600°C. When the worn surfaces are examined with scanning electron microscopy, it is clearly determined that the diffusion annealing prevents the oxidative wear mechanism. Additionally, microstructure of diffusion annealed samples that are subjected to isothermal oxidation tests were relatively found to have proper structure with less defects compared to bare Inconel 718 and only hot-dip aluminized sample.

SICAK DALDIRMA ALÜMİNYUM KAPLAMA VE DİFÜZYON TAVLAMASI UYGULANMIŞ INCONEL 718 SÜPERALAŞIMININ OKSİDASYON VE YÜKSEK SICAKLIK AŞINMA DAVRANIŞININ İNCELENMESİ

ÖZET

Üretim proseslerinin gelişmesi ve stratejik açıdan birçok saf metal veya alaşıma nazaran üstün özelliklere ve çalışma performansına sahip süperalaşımlar, çalışma performansını ve mekanik dayanım potansiyelini yüksek sıcaklık uygulamalarının çeşitli alanlarında sürdürebilen, üstün korozyon ve oksidasyon dirençleri ile öne çıkan alaşım gruplarıdır. Tipik olarak matrisleri östenitik yüzey merkezli kübik (YMK) kristal yapıya sahip elementler olarak nikel (Ni), demir (Fe) ve kobalt (Co) bazlı olarak üç ana gruba ayrılmaktadır. İçeriğinde yüksek oranlarda krom (Cr), nispeten düşük oranlarda alüminyum (Al), titanyum (Ti), molibden (Mo) ve niyobyum (Nb) gibi elementlerin faz dönüşümleri ile hem katı çözelti hem de çökelti sertleştirmesi gibi mekanizmalarıyla dayanımı artırılmış malzemelerdir. Jet ve roket motorlarının parçalarında, nükleer enerji santrallerindeki eşanjörlerde kullanım alanı bulabilen, kullanım ortamında sürünme, aşınma, korozyon veya oksidasyon gibi dış etkenlere maruz kaldığında yüksek sıcaklıklara rağmen çalışma koşullarını optimum düzeyde kararlı olarak sürdürebilen bu malzemelerin kullanım alanı havacılık, uzay ve enerji gibi endüstrilerde yoğunlaşmaktadır.

Nikel bazlı süperalaşımların çoğunluğunda bulunan NiCrFe matrisli yapılar, katı çözelti sertleştirme mekanizmasına sahip olmakla birlikte, içeriğinde bulundurduğu topolojik ve geometrik olarak sıkı paket kristal yapıya sahip fazlara ek olarak karbürlerin varlığı ile yüksek dayanım özellikleri göstermektedirler. Nikel bazlı süperalaşımlardan biri olan Inconel 718, bulundurduğu geometrik sıkı paket (GSP) yapıya sahip koherent γ’ fazı, içerdiği Ni_3 (Al, Ti) çökeltileri ile malzemeye süneklik ve sertlik sağlamaktadır. Genellikle demir içerikli negatif etkileri bulunan topolojik sıkı paket (TSP) fazları mekanik özellikler açısından tercih edilmemektedir. Öte yandan, malzemenin içeriğinde bulunan γ’ fazı ile koherent olan, GSP yapıya ve Ni_3Nb kompozisyonuna sahip γ’’ fazları ile yaşlandırılma yeteneğine sahip olan Inconel 718 süperalaşımları yüksek sıcaklıklarda yüksek dayanım performansı sergileyebilmektedir. Ancak belirli sıcaklıklar üzerinde (650°C) malzemenin içeriğindeki γ’’ fazlarının çözünmeleri sonucunda matrisle koherent özellik göstermeyen δ (Ni_3Nb) fazına dönüşmesi yüksek sıcaklıklarda mekanik özellikleri negatif olarak etkilemektedir. Ek olarak Inconel 718 içerisindeki kromun, Cr_2O_3 fazıyla koruyucu oksit tabaka oluşturarak malzemeye oksidasyon ve korozyon direnci sağlamaktayken 1000°C üzeri sıcaklıklarda CrO_3 uçucu fazına dönüşerek yüzeyden malzeme kaybına sebep olması nedeniyle nispeten yüksek sıcaklık uygulamaları için kaplamayı zorunlu hale getirmektedir.

Difüzyon, overlay (yüzeyüstü) ve termal bariyer gibi korozyon ve oksidasyon direncini artırmaya yönelik yüksek sıcaklık kaplama çeşitleri, süperalaşımların

mekanik ve fiziksel olarak dış etkenlere maruz kalması durumunda süperalaşımlar için stratejik öneme sahip olmakla beraber yapıya kazandırdıkları kararlı yüzeyler ile uygun niteliktedir. Kaplama ve altlık arasındaki uyuma bağlı olarak difüzyon kaplamaları nikel bazlı süperalaşımlar için tercih edilebilmektedir. Özellikle nikel bazlı süperalaşımlara uygulanan, difüzyon mekanizmasına dayanan alüminyum kaplamalar, oluşturdukları nikel-alüminat fazlarıyla malzemeye yüksek yüzey kararlığı ve oksidasyon direnci sağlamasıyla öne çıkmaktadır. Nikel bazlı süperalaşımlar üzerine alüminyum kaplama ile içe doğru difüzyon-yüksek aktivite ve dışa doğru difüzyon-yüksek aktivite mekanizmaları ile oluşturulan nikel-alüminat fazları, yüksek sıcaklık ve oksidatif ortamda kaplamanın yüzey kısmında alüminyumun oluşturduğu koruyucu Al_2O_3 tabakası için rezervuar görevini üstlenmektedir.

Kutu sementasyon, kimyasal buhar biriktirme ve sıcak daldırma kaplama (hot-dip coating) gibi difüzyon kaplama yöntemleri maliyet ve uygulanabilirlik bakımından çeşitli faydalara ve eksikliklere sahiptir. Örneğin kimyasal buhar biriktirme düşük biriktirme hızına, kutu sementasyon yüksek biriktirme hızına sahip olmasıyla öne çıkmaktadır.

Sıcak daldırma yönteminde dikkat edilmesi gereken unsurlardan biri olan sıcaklık, faz dönüşümlerini etkilemesiyle zaman ve daldırma ortamı gibi diğer parametrelere nazaran bir adım daha öne çıkmaktadır. Diğer bir önemli parametre olan ergiyik banyo kompozisyonu faz dönüşümleri ve interdifüzyon bölge için önem arz etmektedir. Difüzyon tavlaması ile kontrollü olarak oluşturulmak istenen fazlar fırınının sıcaklık, zaman ve atmosferine bağlı olarak değişiklik gösterebilmektedir.

Literatürde farklı yöntemlerle kaplanmış Inconel serisi için aşınma çalışmaları güncel olarak yer almaktadır. Özellikle çalışmaların çoğunluğu yüzeyüstü (overlay) ve termal bariyer kaplamalar olarak karşımıza çıksa da Inconel serisi için difüzyon mekanizmalı kaplamaların aşınma davranışları üzerine yapılan bu çalışmalar literatür eksikliğini giderecek birikim sağlamamıştır. Ek olarak, difüzyon mekanizması ile sıcak daldırma yöntemi kullanılarak kaplanan Inconel 718 süperalaşımının yüksek sıcaklık aşınma davranışı daha önce çalışılmamış bir konu olması ile literatüre eklenerek genişletilmesi ve katkı sağlaması önem arz etmektedir.

Bu çalışma kapsamında, sıcak daldırma yöntemi ile Alüminyum kaplanan Inconel 718 süperalaşımının, oda sıcaklığında ve yüksek sıcaklıkta aşınma davranışlarına ek olarak izotermal oksidasyon testi ile sıcak daldırma yönteminin devamı niteliğinde olan difüzyon tavlamasının etkileri incelenerek araştırılmıştır.

Bu çalışmada, Inconel 718 numuneleri, 700°C'de 2 dakika tutularak sıcak daldırma yöntemi ile alüminyum-silisyum ötektik alaşımı kaplanmıştır. Alüminyum ile kaplanan Inconel 718 numuneleri 700°C'de 10 saat difüzyon tavlanmasına tabii tutulmuştur. Elde edilen numuneler ile Inconel 718 numuneleri 25°C'de, 300°C'de ve 600°C'de olmak üzere aşınma testlerine ve 800°C'de 100 ve 300 saat olmak üzere izotermal oksidasyon testlerine tabii tutulan numunelerin yapısal karakterizasyon işlemleri gerçekleştirilmiştir.

Çalışmanın deney kısmında, Inconel 718 numuneleri silindirik 8 mm kalınlığında kesilerek 120, 240, 320 ve 400 numara disklerle zımparalanarak sıcak daldırma prosesi için hazırlanmıştır. Alüminyum-silisyum ötektik alaşımı (%12 ağ.) banyosuna daldırılmak üzere, numuneler 2 mm kalınlığında paslanmaz çelik tel ile eğimli yüzeylerden sarılarak hazırlanmıştır. Farklı kaplama çeşitleri için de büyük önem arz eden kaplanacak olan malzemenin yüzey temizliği, seyreltilmiş HCl çözeltisi içerisinde ultrasonik dalgalarla temizlendikten sonra etanol ile yüzey silindi ve su ile durulanarak daldırma işlemine hazır hale getirilerek sağlanmıştır. Al-Si ötektik alaşım ingotlar potaya uygun ölçülerde kesilmiş olup, fırın istenilen sıcaklığa geldikten sonra yaklaşık 1 cm3 KCl ve NaCl karışımı olan flaks eklenerek ergiyik üzerindeki cüruf elimine edilmiştir. Temizlenen numuneler 700°C'de 2 dakika olacak şekilde grafit potanın orta kısmına doğru daldırıldı. Asılarak oda sıcaklığında soğumaya bırakılan numuneler için kaplama işlemleri gerçekleştirilmiştir. Sıcak daldırma işlemine ek olarak örnekler 700°C'de 10 saat difüzyon tavlamasına tabii tutulmuş ve fırında soğutma işlemleri gerçekleştirilmiştir. Sıcak daldırma ile kaplanmış numuneler ve difüzyon tavlaması uygulanmış numunelerin mikroyapı incelemeleri Philips XL30 SFEG marka taramalı elektron mikroskobu (SEM) ile nokta, çizgi, haritalama EDS analizleri gerçekleştirilmiştir. Aşınma izlerinin görüntüleri Hitachi TM1000 model (SEM) ile alınmış olup, sertlik değerleri Wilson Tukon 1102 Microhardness cihazı ile ölçülmüştür. Aşınma deneyleri CSM-High temperature unidirectional ball-on disc tribometer ile gerçekleştirilmiştir. İzotermal oksidasyon testi kapalı döngü düzenek ile PRC 110M/GWP model teçhizat ile uygulanmış olup karakterizasyon analizleri Philips XL30 SFEG marka taramalı elektron mikroskobu (SEM) ile nokta ve haritalama EDS analizleri gerçekleştirilmiş olup XRD analizleri GBC MMA 027 model 10°-100° 1°/dk ile gerçekleştirilmiştir.

Kaplanmış ve difüzyon tavlanmış numunelerin aşınma davranışlarının incelenmesi için üç farklı sıcaklıkta tribometre kullanılarak alümina bilyeye karşı aşınması testleri gerçekleştirilmiştir. 2N yük altında aşınma testine tabii tutulan numunlerin tek yönlü çalışan disk üzerinde sürtünen bilya (ball-on-disc) ile aşınma davranışları incelenmiştir. 2-D temaslı yüzey profilometre ile aşınma yüzeyinde oluşan izler analiz edilmiş olup, aşınmanın yüzeyde hangi mekanizmalarla gerçekleştiğine dair analizler taramalı elektron mikroskobu ile gerçekleştirilmiştir. Ayriyeten, aşınma testleri esnasında kullanılan alümina bilyelerin yüzeyi optik mikroskop ile incelemeye alınmıştır.

Elde edilen aşınma testi sonuçlarının verilerine göre, 25°C sıcaklıkta difüzyon tavlanmış numunelerin aşınma oranı sadece sıcak daldırma ile kaplanmış numunelere göre üç kat, işlem görmemiş Inconel 718 numunelerine göre 4 kat daha az olduğu saptanmıştır.

300°C'de ve 600°C'de gerçekleştirilen testlerde, kaplanmış numuneler için difüzyon tavlamasının göreceli olarak gerekliliği ön plana çıkmıştır. Aşınma yüzeyleri taramalı elektron mikroskobu ile incelendiğinde difüzyon tavlamasının oksidatif aşınma mekanizmasını engeller nitelikte olduğu görülmektedir. 800°C'de gerçekleştirilen izotermal oksidasyon testleri sonucunda difüzyon tavlamasının yapısal olarak gerekliliği aşınma testlerinde olduğu gibi öne çıkmıştır.

1. INTRODUCTION

Definition of superalloys can be expressed as nickel, iron and cobalt based chromium alloyed materials that has capability to sustain its performance with excellent mechanical durability, good surface stability, superior resistance against aggressive environment at high temperature.

Nickel-based superalloys have been mostly used in the aviation and aerospace industries due to excellent mechanical resistance based on precipitation and solid solution strengthening mechanism in addition to resistance against oxidation and corrosion despite high temperature exposure.

Inconel 718 is a type of nickel-based superalloy that has strengthened with the precipitation of γ’’ – (Ni_3Nb) phases. Content of Cr in Inconel 718 is in charge of oxidation and corrosion resistivity. Above 650°C, transformation of γ’’ to δ by dissolving decrases mechanical strength. On the other hand, protective Cr_2O_3 layer has tendency to transform volatile compound of CrO_3 above 1000°C.

Various types of coating methods are applied to superalloys to provide the requirements of different environmental conditions. Every process has its own advantages and disadvantages concerning applicability and cost. One of the diffusion coating methods commonly used for high-temperature parts is hot-dip aluminizing (HDA). For that purpose, the HDA method is applied to improve surface properties of Inconel 718 Nickel-Based Superalloys. Inconel 718 samples subjected to HDA with different time and temperature processes have been investigated by microstructural and mechanical examination.

In this study, Inconel 718 samples are aluminized at 700°C for 2 minutes by hot-dipping then, some of aluminized sample were subjected to diffusion annealing at 700°C for 10 hours. Wear tests for bare, hot-dip aluminized, hot-dip aluminized and diffusion annealed Inconel 718 samples were performed at 25°C,300°C and 600°C in order to investigate high temperature tribological behavior. In addition to wear test, samples were subjected to isothermal oxidation test at 800°C for 100 and 300 hours to comprehend oxidation behavior. Structural analyses were done by using scanning electron microscope, energy dispersive spectroscopy and X-ray diffractometer.

This study mainly focuses on investigation of high temperature wear and oxidation behavior of bare, hot-dip aluminized, hot-dip aluminized and diffusion annealed Inconel 718 superalloy.

2. SUPERALLOYS

In the beginning era of "superalloy" term , metallurgical committees and designers had needed more corrosion-oxidation resistant materials for application of high temperature. Concurrently, gas turbines took significant role to invent alloys during World War 2. Moreover, limited properties of materials that used in aircraft engine parts were increasing tendency to invent new alloy group [1] . The term of "super" had become more popular among societies. According to normal of that era, possibly, the "superalloy" term has been inferenced by popularity of comic book character superman [2].

Definition of superalloys is expressed as nickel, iron and cobalt based chromium alloyed materials that has capability to sustain its performance with excellent mechanical durability, good surface stability, superior resistance against aggressive environment at high temperature.

Basically, superalloys have three main characteristics that are distinguished from other types of alloys. The first desirable characteristic property is having ability to withstand heavy loads despite operating close to its melting point. Second one is capability to significant resistance to mechanical degradation over extended periods of time. Lastly, appropriate tolerance stands out even if the parts that are made of superalloys subjected to operate at harmful environments such as corrosive conditions [1].

2.1 Properties of Superalloys

2.1.1 Atomic and crystal properties

Mainly crystal structure of superalloys is typically face-centered cubic (FCC) which includes alloys of groups such as Hastelloy, Inconel, Rene etc. In addition, superalloys were generally produced as single-crystal that provide creep resistance to material [2][3]. Both solid-solution and precipitation strengthening mechanisms form the nature of superalloys by alloying with different elements. Carbides and gamma prime secondary phase precipitates have capabilities to create optimal conditions in behalf of superalloys. Furthermore, elements in superalloys such as aluminum and chromium have advantages to increase oxidation or corrosion resistance.

2.1.2 Properties and effects of elements

Base matrix of superalloys has been formed by nickel, cobalt and iron. Chromium element in superalloys provides corrosion and oxidation resistance by forming an oxide layer. Aluminum is known as the main γ' former that enhance the strength of material by precipitation hardening. Moreover, the protective oxide layer of aluminum has the capability to resist at higher temperatures more than chromium oxides. Titanium is desirable for precipitation strength mechanism due to form γ' phases. Forms of carbon as carbide are the strengthening phases in absence of γ' phases. Boron and zirconium support the strength of grain boundaries. Yet, they are not essential in single crystal turbine blade applications due to the absence of grain boundaries. Niobium can form γ'' strengthening phase which desirable below 700°C temperature. A small addition of Rhenium, Tungsten, Hafnium, Molybdenum and Tantalum tend to provide solid solution strengthening and carbide formation as refractory metals in superalloys.

In the first instance, iron and nickel-based superalloys were investigated. Nickel-based superalloys have key roles to draw a way for examining structure properties rather than iron-based. Afterwards, phases in cobalt-based superalloy will be introduced to complete phases section.

Generally, three types of intermetallic phases are presented in the nickel-base superalloys. They are known as carbides, geometrically close-packed (GCP) and topologically close-packed (TCP) phases. Although phases exist as beneficial to increase strength and creep rupture life as well as fatigue properties, nevertheless some of them have a negative tendency to affect mechanical properties. The disordered FCC matrix should chiefly exhibit proper structure to prepare the background for solid solution and precipitation strengthening mechanisms.

2.1.2.1 Carbides

Carbides in the structure of MC, $M_{23}C_6$ and M_6C (M=metal) are in the form of rounded cubes, spheres or platelets and coherent with FCC structure. They provide stabilization of grain boundary and dispersion strengthening in nickel-based superalloys.

2.1.2.2 Geometrically close-packed (GCP) phases

Geometrically close-packed (GCP) γ' phase is coherent with the matrix in form of $Ni_3(Al, Ti)$. γ' is the main strengthening phase with the $L1_2$ (ordered FCC) structure.

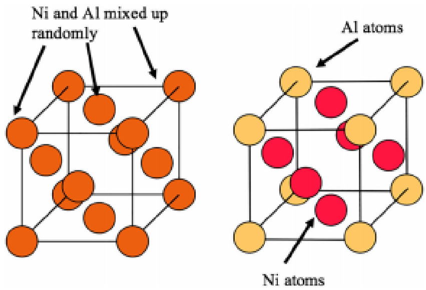

Figure 2.1 : $L1_2$ (ordered FCC) structure [4].

Additionally, other type of GCP phase is in form of $D0_{22}$ structure Body-Centered Tetragonal (BCT). In superalloys, this BCT $D0_{22}$ structure can be referred as γ" (Ni_3Nb) that appear like very small disks. It has coherency with main precipitation strengthener γ' phase but dissolves at high temperature relative to main γ' phase. On the other hand, after γ" (Ni_3Nb) phase dissolves, it transforms into not close-packed orthorhombic δ (Ni_3Nb) phase. δ phase appears acicular (needle-like) and can intentionally be added to refine grains. Depending on quantity and morphologies, it has been indicated that δ phase ,situated on grain boundary of IN-718 alloy, increases tensile strength and fatigue properties [5].

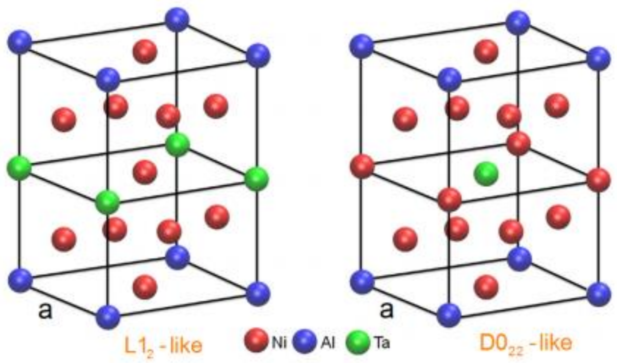

Figure 2.2 : Two crystal structures of $Ni_3Al_{0.5}Ta_{0.5}$ [6].

Another GCP phase can be referred as η with the $D0_{24}$ ordered Hexagonal close-packed (HCP) Ni_3Ti. Appearance of η is like cellular and it does not have advantage of strong precipitate as good as γ'. Yet, η can be used to optimize grain boundaries.

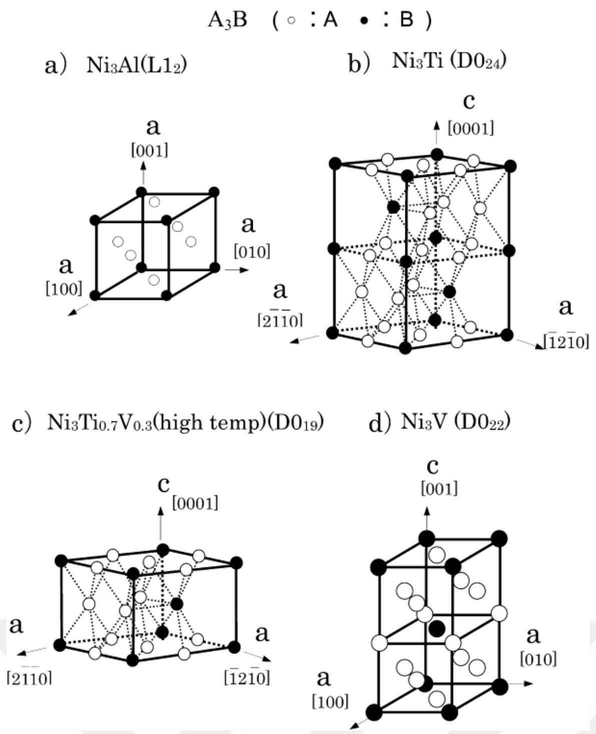

Figure 2.3 : Crystal structures of GCP phases [7].

2.1.2.3 Topologically close-packed (TCP) phases

Frank and Kasper have first investigated Topologically Close-Packed (TCP) phases that are often deleterious due to not completely close-packed and brittle properties. According to precipitation of TCP phases studies, TCP phases preferentially precipitates into dendrites. TCP phases direction is not consistent with the matrix phase. It is difficult to precipitate among inter-dendrite and grain boundary which cause to segregation [8].

Generally, TCP phases in superalloys are divided into three groups given in table below [9]. An example illustration of TCP phases is shown in Table 2.1.

Table 2.1 : List of TCP phases in superalloys [10].

Phase	Structure	Composition	Appearance
σ	Tetrahedral	FeCr, FeCrMo, CrCo	Elongated globules
μ	Hexagonal	Fe_2Nb, Co_2Ti, Fe_2Ti	Globules or platelets
Laves	Rhombohedral	$(Fe,Co)_7(MoW)_6$	Coarse Widmanstätten platelets

TCP phases are generally considered undesirable phases that has negative effects on mechanical properties for superalloys. Incoherency between TCPs and matrix reflects undesirable properties. Sharp plate or need-like morphologies usually triggers cracks.

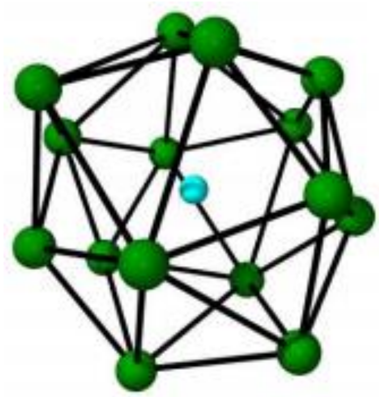

Figure 2.4 : The atoms in topologically close-packed phases [11].

<u>σ phase</u>

FeCr, CrCo and FeCrMo are example of σ phases. Effect of σ phase has been mostly unfavorable for tensile and impact strength, corrosion properties. Also, it should be avoided in duplex stainless steels which is studied by researchers [12]. TEM micrograph of σ phase is shown in Figure 2.5 referenced from study about phase transformation in a Ni-based superalloy [13].

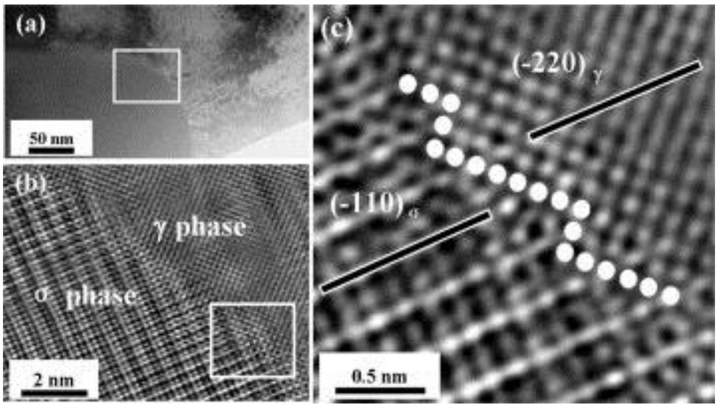

Figure 2.5 : TEM micrograph of σ phase [13].

<u>μ phase</u>

μ phase can be defined as an intergrowth of tetrahedrally close-packed sheets. Fe_2Nb, Fe_2Ti are two examples of μ phase. One of the studies has indicated that μ-phase exhibits a high density of sub-unit cell twins [14]. Also, behavior of μ TCP phase in nickel-based superalloy has been investigated. Excessive precipitation of μ phase negatively effects mechanical properties of the alloy [15]. TEM observations of μ phase nucleating is given in Figure 2.6 from a precious study about μ-phase behavior in a cast Ni-base superalloy [13].

Laves phases

Detrimental Laves phases occurs in inter-dendritic regions of materials when heat applied for instance welding. Laves phase takes places due to segregation that leads components failure during service [16].

Arranging optimal distribution becomes more important in point of balance between GCP and TCP phases.

Phases in cobalt-based superalloy were listed below.

Gamma (γ): This phase represents matrix similar to nickel-based superalloys.

Gamma Prime (γ'): It is usually geometrically close-packed (GCP) with a $L1_2$ structure of Co_3Ti or FCC Co_3Ta. For stabilizing at high temperature, elements like Ta, Nb, and Ti are effective for γ' phase [17]. This stabilization is reasonably important especially for Co-based superalloys [18]. Similarly, carbides provides strength with precipitation, like in Ni-based superalloys [19]. Topologically close-packed phases have been existed in co-based superalloys with the negative effects for other types of superalloys.

2.2 Classification of Superalloys

Superalloys have been classified under three major categories that depends on predominant metals, these are:

1. Nickel Based Superalloys
2. Iron Based Superalloys
3. Cobalt Based Superalloys

Chromium have been mostly existed in the composition of superalloys. Also, it stands out with the great advantages of oxidation and corrosion resistance due to forming chromia.

2.2.1 Ni-Based superalloys

Historically, developed countries had started to look for more durable gas turbine engine parts in 1905. Demands for high-temperature material have been increasing, while austenitic stainless steels had been using in gas turbine parts. Concurrently, austenitic stainless-steel alloys were being used to respond requirements of high temperature application between 1910-1915. Nickel-chromium alloys became more important by adding Al and Ti by 1929. By this way, coincidentally, metallurgists have developed the main strengthening phase geometrically close-packed $Ni_3(Al, Ti)$ FCC precipitates that have coherency with FCC matrix and supply good mechanical property.

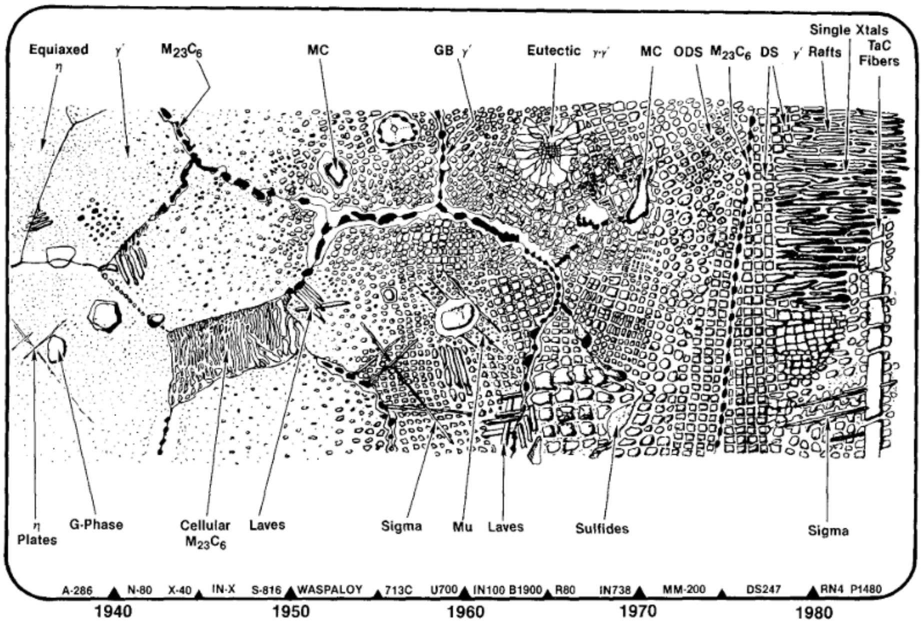

Figure 2.6 : Panoramic image of useful and deleterious phases in nickel superalloy microstructure [20].

Moreover, chromium can protect materials from corrosion and oxidation up to 1000°C in the form of Cr_2O_3. Afterwards, oxidation resistance of aluminum with the phase of Al_2O_3 has emerged despite its limitation against corrosion. Compared to other types of iron and cobalt-based superalloys that are mostly strengthening by carbides and solid-solution, nickel-based superalloys have surpassed them.

2.2.2 Fe-Based superalloys

In the early years, iron and its alloys were consisting sufficient chromium for oxidation resistance. Besides iron carbides, concurrently, the small amounts of aluminum, titanium, and/or columbium have been firstly added to steels in 1929 to produce coherent creep-resisting phase as precipitate. Unconsciously harmful incoherent phases have been obtained by these kinds of experiment [20]. Conventionally, iron has wide usage area for many fields due to cumulative literature and long-term experience, especially for high-temperature application. Stepwise, iron element in composition has started to disappear, while major content of nickel and chromium increased in behalf of oxidation and corrosion resistance.

For iron-based superalloys, austenitic iron (FCC) plays important role for coherent secondary phases that includes Al, Cr, C, B, Co, Mo, Ni, Nb, Si, Ti, W and Y. Precipitation strengthening mechanism provided by proper balance of addition Al, Ni, Ti and Nb elements like in the nickel-based superalloys. On the other hand, high weight fraction of aluminum led to stabilize ferritic BCC matrix which is undesirable superalloys microstructure [21].

The major types of oxide layer have been applied by forming chromia and alumina layer on the surface in behalf of enhancing resistivity against oxidation and corrosion for iron-based superalloys. Alumina has thermodynamically advantage to facilitate oxidation resistance more than chromia. Yet, when nickel-aluminide precipitates ,that are responsible to supply reservoir through surface, require stabilization with the addition of Nb and Cr elements that helps to increase precipitate volume fraction of nickel-aluminides.

2.2.3 Co-Based superalloys

Similarly, mechanical properties of cobalt-based superalloys depend on solid-solution and precipitation strengthening particularly with carbides [18]. Furthermore, cobalt-based superalloys have gained substitution opportunity in several significant fields against nickel-based superalloys where higher temperature stability is needed [22].

There are many precious studies about Co-Al-W precipitation hardened Co-based superalloys by Sato et al. which opened new aspects for cobalt-based superalloys [17].

2.3 Inconel 718 Nickel-Based Superalloy

The Inconel series are mainly member of the Ni-Cr based superalloys group that has ability to show perfect mechanical properties in the wide range of composition. Ni and

Cr have capability to improve the resistance of oxidation and corrosion even if they are subjected to high temperature exposure. Moreover, cryogenic, fatigue and creep behavior properties are the main characteristics of Inconel series. Generally, adding elements such as Fe, Al, Ti, Nb, Mo, Co, Cu, W can be desirable to increase mechanical and chemical properties [23].

Inconel 718 was first produced in 1960s and started to be used in 1965 to fulfill rising demands for developing high-strength nickel alloys.

Inconel 718 is a precipitation-hardenable nickel alloy with outstanding corrosion resistance in many usage areas. Significant amount of Cr, Fe, Nb, Mo and minor contents of Al, Ti are present in composition. Alloy 718 is employed in gas turbines, rocket engine parts, turbine blades where good corrosion and high mechanical properties are needed despite high temperature conditions .

2.3.1 Physical properties

Its melting range is 1260–1336°C, and it has a density of 8.22 g/cm^3.

Temperature dependent thermo-physical properties of Inconel 718 were shown in the Figure 2.9.

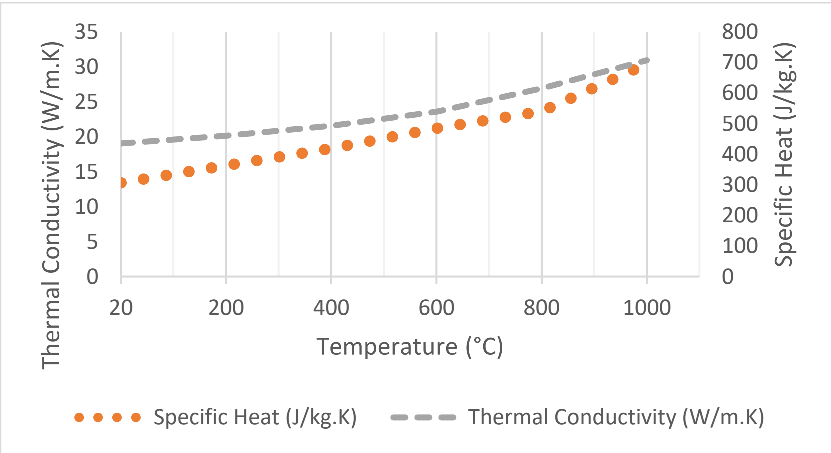

Figure 2.7 : Temperature dependent thermo-physical properties of Inconel 718 [24].

2.3.2 Mechanical properties

Inconel 718 superalloy contains γ''-Ni_3Nb phases that has significant effect on strength different from other type of superalloys. Also, these phases are coherent with γ' GCP phases like $Ni_3(Al, Ti)$. But there is an inevitable fact that γ''-Ni_3Nb phases has tendency to dissolve above 650°C, then, transforms into δ phases that has possibility to show weak mechanical properties. In the Figure 2.10, decrease in yield strength were clearly seen above 650°C. For this case, coating demands to use the Inconel 718 at high temperatures, particularly above 650°C, has been increasing.

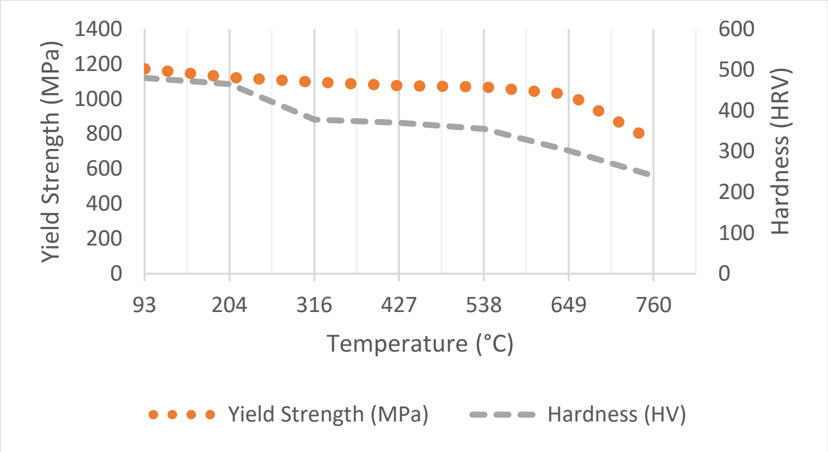

Figure 2.8 : Temperature dependent yield strength and hardness measurements of Inconel 718.

2.3.3 Chemical properties

Inconel 718 containing Ni and Cr contribute to increase corrosion resistance of this material. They crystallize as a γ phase (face centered cubic). Cr element is the primary corrosion and oxidation resistance adjacent. Also, it is resistant to sulphur compounds. Chromium content 17-21 wt.% in Inconel 718 allows the development of protective surface chromia scale in most atmosphere. On the other hand, chromia-based alloys like Inconel 718 are limited in their high temperature use due to protective oxide scale is decomposing into CrO_3 that shows volatile properties approximately above 950°C. Also, high shear stress between Cr_2O_3 scale and carbides beneath surface leads to scale cracks and internal corrosion [23][25].

3. COATINGS OF SUPERALLOYS

Surface engineering has consistently played considerable role to develop coating technology for high temperature plants that includes generation of energy, chemical processing or component heat treatment. Therefore, demands for improved mechanical properties with longer service lives at higher temperature became more important for desires [26]. Many high temperature components are coated or surface modified to achieve for their requirements during service [27].

Characteristics of coating layer of substrate has correlatively been used as a key for classification with respect to chemical, physical and mechanical properties of surface. Firstly, the high temperature coatings have been investigated that are divided into three groups as types of coatings that are listed below [26,28].

1. Diffusion Coatings
2. Overlay Coatings
3. Thermal Barrier Coatings (TBC)

Secondly, there are different types of methods about coating especially for Ni-based superalloys such as chemical vapor deposition (CVD) [29], physical vapor deposition (PVD) [30], high-velocity oxy-fuel (HVOF) spraying [31], cold spraying [32], thermal spraying [33] and plasma spraying [34] and Hot-Dip Aluminizing (HDA) [35,36]. All the coating methods has been supported by types of coatings like diffusion, overlay etc.

In this section, coatings of superalloys were mainly divided into two groups as types of coating and methods of coating. Surface properties of coatings types has regularly been associated with methods of coating.

3.1 High Temperature Coatings

High temperature coating that applied to substrate should have the significant requirements which are:

- Oxidation and corrosion resistance in hazardous environments.
- Compatibility with substrate in point of thermal expansion and conductivity.
- Costly-applicable and technologically-feasible.

Thermal barrier coatings stand out as resistivity against high-temperature compared to other types of coatings. Nevertheless, when all the high temperature coatings have been taken into accounts, they have variable distinctive properties according to working condition, efficiency and feasibility in their fields.

Materials, coating types and process methods has been developed in many applications.

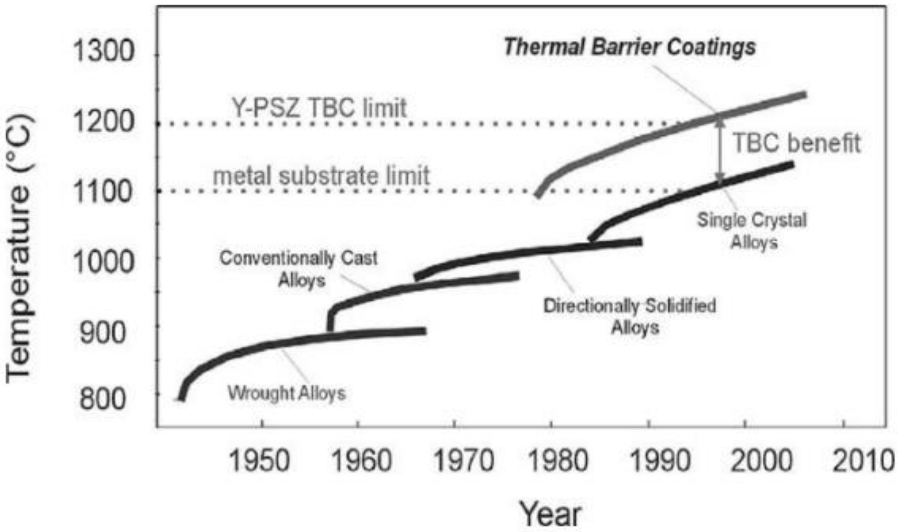

Figure 3.1 : Increase in operational temperature of turbine components [37].

3.1.1 Diffusion coatings

Diffusion coating mechanism has partly emerged as popular with aluminum diffusion coatings. Aluminum diffusion coatings on superalloy have been firstly used for gas turbine aerofoils in the early 1960s, to increase oxidation and corrosion resistance [38]. In 1970s, renewed trend about diffusion coating with combining silicon interest concurrently became popular in meaning of novel approach [39].

High temperature diffusion coatings have been developed to enrich surface of an alloy with at least one of the elements that are aluminum, chromium or silicon. Combination of these elements were used according to requirements for high temperature applications [26]. Physical and mechanical properties such as thermal conductivity, thermal expansion and thermal fatigue were adjustable by changing composition of coating material and coating method parameters.

Generally, aluminum, chromium and silicon elements of diffusion coatings have been used for many years to investigate [40]. Mechanism of diffusion have been selected and inferred by aluminizing in the last few decades. There are two types of mechanisms for diffusion coating of aluminum on nickel-based superalloy. First one is inward diffusion of aluminum from surface to substrate. High activity of aluminum in proper conditions, in the point of temperature and time, has advantages to form nickel-aluminides. However, in case of inward aluminum diffusion, heat treatments were usually performed to form desirable NiAl phases that particularly play significant role with respect to physical and mechanical properties. Second one is outward diffusion of nickel from substrate to surface to stabilize NiAl phases that adequately allow to create compatible reservoir for aluminum. On the other hand, parameters and processes of diffusion coating should be attentively investigated to not led to Kirkendall effects that causes pores, cracks and these types of defects [41]. Both mechanisms have strongly depended on elemental activities which is changing with diffusion parameters such as temperature and time.

Examples of aluminum diffusion coatings on nickel-based superalloys stands out ,as a guide to comprehend the mechanisms, were gathered from literature. There is a precious study about hot-dip aluminizing of Inconel 718 as a diffusion, coating. Cross-sectional and top surface SEM image of coating microstructure with XRD pattern results were shown in Figure 3.2 [34].

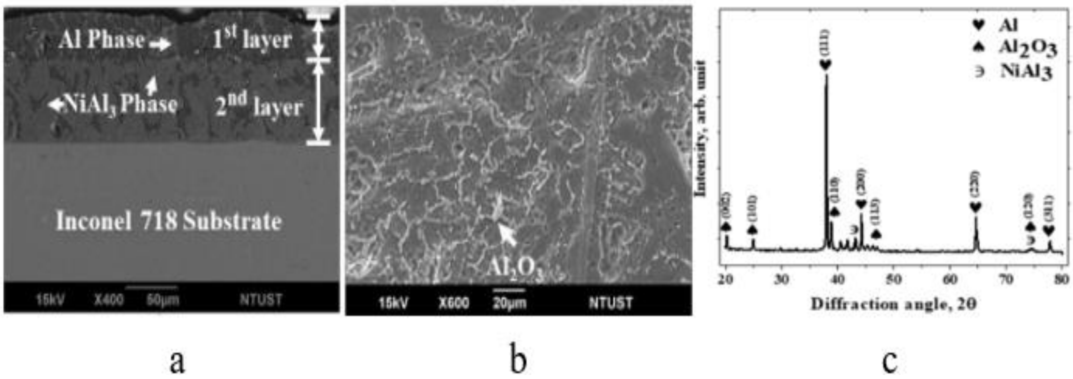

Figure 3.2 : a) Cross-sectional SEM image of HDA Inconel 718, b) SEM Image of top surface, c) XRD pattern of HDA Inconel 718 [34].

3.1.2 Overlay coatings

Overlay coatings specifically has been mostly applied in form of MCrAlX [M=Ni and/or Co, occasionally Fe metals, X=Oxygen Reactive Elements (Y, Hf, Si, Zr etc.)] with advanced technological coating methods.

Overlay coatings have cumulatively been developed while number of researches about high temperature coatings increased. Addition of oxygen reactive elements were patented in 1937 by Griffiths and Pfeil which has capability to enhance thermal cycling [42]. Lustman has summarized knowledge about active elements prior to 1950. In 1964, FeCrAlY emerged from General Electric nuclear programs. This composition was not practically useful for Ni-based substrate due to formation of NiAl. Similarly, NiCrAlY types showed limitation about hot corrosion resistance. Next series was CoCrAlY which has hot corrosion and oxidation resistance, yet this series had no capability to fulfill requirements of ductility. Combination of these composition that is NiCoCrAlY has relatively showed better properties. Now at least 40 patented variations existed[43].

In modern overlay coatings the composition of the M-Cr-Al-X system is selected to improve materials oxidation resistance and corrosion resistance. Oxidation resistance and hot corrosion resistance are provided by Ni-Cr-Al-Y and Co-Cr-Al-Y coatings, respectively [26]. Also, incompatibility between substrate and coatings could possibly be neglectable regarding reactions among both structures [44].

3.1.3 Thermal barrier coatings

In the past, Thermal Barrier Coatings (TBC) were first successfully tested by part of gas turbine engine section in the 1970s. Concurrently, two process methods were used to apply coatings by plasma spraying and physical vapor deposition (PVD). There was fact that the both process methods, especially for PVD coatings, embraced the success in many high temperature coating fields [45].

Compared to other high temperature coating approaches, TBCs stand out due to many types of mechanisms. Structure of TBC takes a shield role against tough working condition like high-temperature environments. Basically, TBCs are thermal shield system that include ceramic topcoat, thermally grown oxide and bond coat. Coating structure of TBCs were illustrated in Figure 3.3.

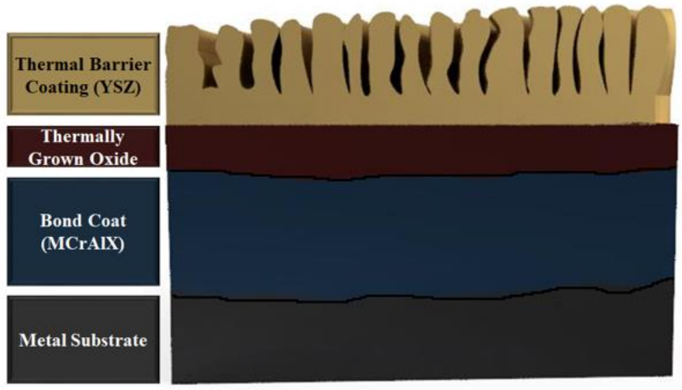

Figure 3.3 : Illustration of TBC's layers.

All the layers have tough duties one by one. In ceramic topcoat, yttria stabilized zirconia is used to provide low thermal conductivity and stabilization at high temperature as a thermal insulator. The other layer extends beneath ceramic topcoat called thermally grown oxides (TGO). TGO layer inhibits oxidation of the bond coat that in charge of forming diffusion barrier against elements that are coming from substrate. Reversely, TGO has another duty through ceramic topcoat for oxygen stability. Likewise, a dense bond coat improves protection of substrate against oxidation and hot-corrosion cracks by adhering strongly to the substrate. TBCs often require porosity between columns that provides strain tolerance. These porosities have advantage of reducing thermal conductivity . Considerably, TBC are sensitively designed and optionally arrangeable system with four layers of through substrate to topcoat.

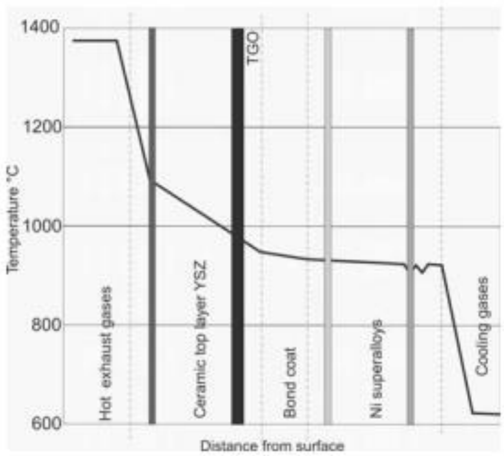

Figure 3.4 : Temperature Distribution of TBC's layers [46].

Basically, the TBC structure on coated materials is based on four layers through substrate to topcoat which are:

Ceramic Topcoat: The ceramic topcoat typically consists of ZrO_2 stabilized with Y_2O_3 (YSZ – Yttria Stabilized Zirconia), that has a low thermal conductivity, shows inert properties, has a compatible thermal expansion coefficient with Ni-base superalloys. Outer ceramic topcoat zone has been called TBC due to requirements of build durable barrier against high temperature, but there is fact that ceramic zone could not be well-to-do independently [44].

Coating thickness in the range of about 1-200 μm is effective to reduce the surface temperature up to 200K. The temperature decrease rate between thermal conductivity and thickness of TBC is approximately 1 °C/μm. Usually, the thickness of TBC is within a range of 250-500μm. There is an inevitable fact that YSZ TBC slowly starts to degrade above 1300°C. For solution, while a well-engineered TBC system has been planned to carry out in the meaning of the thickness-related temperature, thermal properties of the substrate should have been considering for whole surface engineering [21].

There are many types of TBC coatings with different materials and coating methods. YSZ is the most widely studied and used for TBC applications due to excellent performance in usage component such as diesel engines and gas turbines. Limitation of operating temperature has been expressed by phase transformation [47]. Mullite is a compound of alumina and silica and exhibits thermal stability at high temperature, low thermal conductivity, corrosion and oxidation resistance. On the other hand, limitation of mullite are volume contraction and crystallization above 800°C that leads to delamination and cracking. High hardness and chemical stability are major properties of alumina.

Thermally Grown Oxide (TGO): A thermally grown oxide (TGO) layer is formed at the interface of bond coat/top coat [48]. Beneath the ceramic topcoat, thermally grown oxide (TGO) extends parallelly to inhibit oxidation of bond coat. Oxidation of bond-coat leads to form TGO with the effect of high-temperature. Formation of TGO is inevitable case for various types of high temperature applications, therefore TBCs should have been designed by taking account of TGO layer that must grow uniformly and slowly [48]. Oxygen is mutual element of topcoat and TGO, Zr_2O_3 has tendency to penetrate its oxygen into TGO with proper condition. This case leads to thicken TGO, so some kinds of spallation and catastrophic failure occurs for TBCs.

Bond Coat: The bond coat provides adhesion between thermal barrier coating and substrate. Additionally, the bond coat stands out with the function of oxidation protection and diffusion barrier. There are five major types of bond coats, the aluminides, the platinum-aluminides, MCrAlX (M=Ni and/or Co, X= minor elements), cobalt-cermets, and nickel-chromium [49]. MCrAlY bond coat is commonly applied by plasma spraying. The chromia in bond coat are desirable for oxidation and hot-corrosion resistance. Alumina is effective to control oxidation while yttrium provides oxide- substrate adhesion [50].

Substrate: Generally, TBC coatings are applied onto the superalloys that has advantage of proper substrate and perfect resistance of thermo-mechanical load for high temperature coatings. Figure 3.5 shows that materials used in TBC layers and their functions.

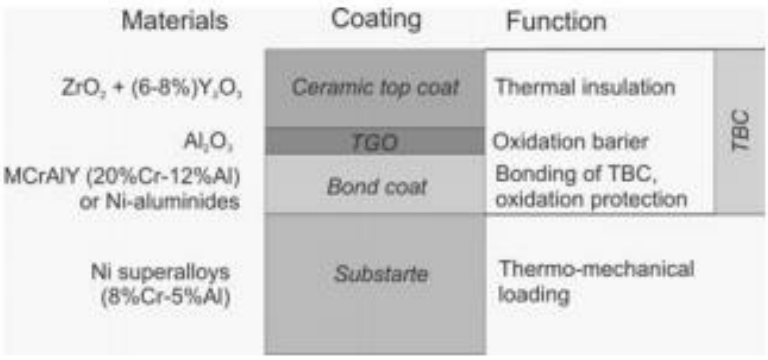

Figure 3.5 : Scheme of coating construction of barrier layers and a role of individual sub-layers [51].

There are cross-sectional microstructures images of TBC were shown in Figure 3.6 .

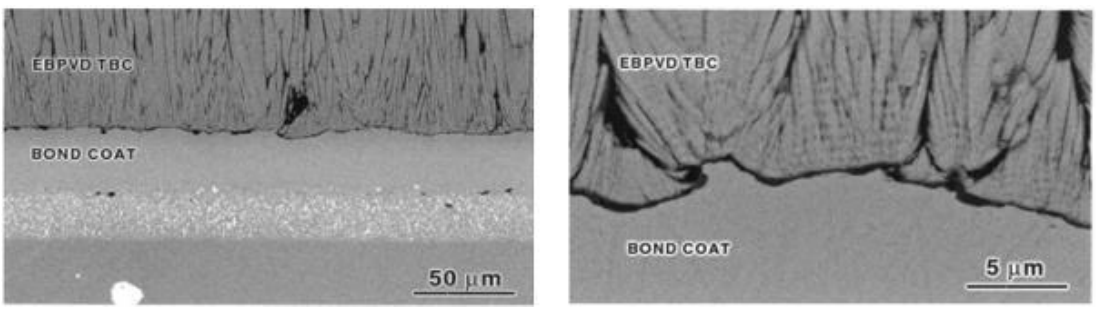

Figure 3.6 : Cross-sectional micrographs showing a typical TBC system [52].

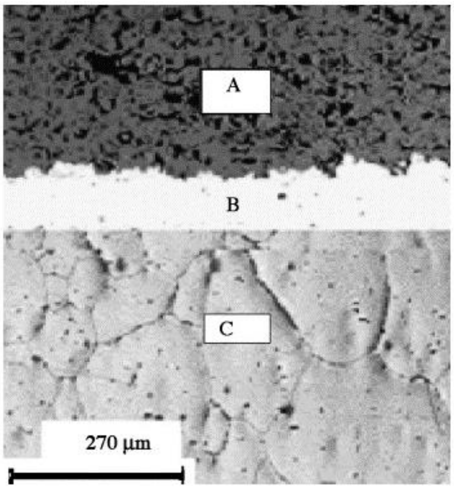

Figure 3.7 : Typical light optical photomicrograph of the thermal barrier coated Superni C263 alloy. A) TBC, B) Bond coat, C) Substrate (Superni C263 alloy) [53].

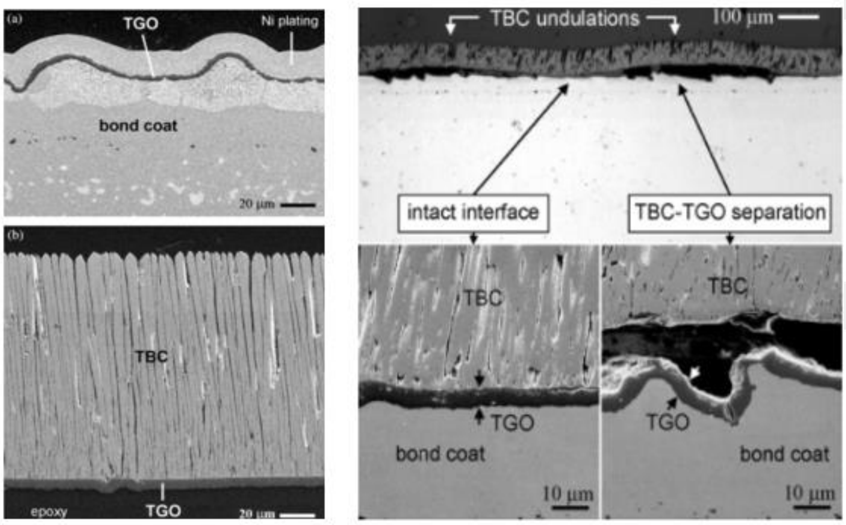

Figure 3.8 : TBC coating image of EB-PVD [53].

3.2 Methods of High Temperature Coatings

Schematic illustration of coating methods was shown in Figure 3.9.

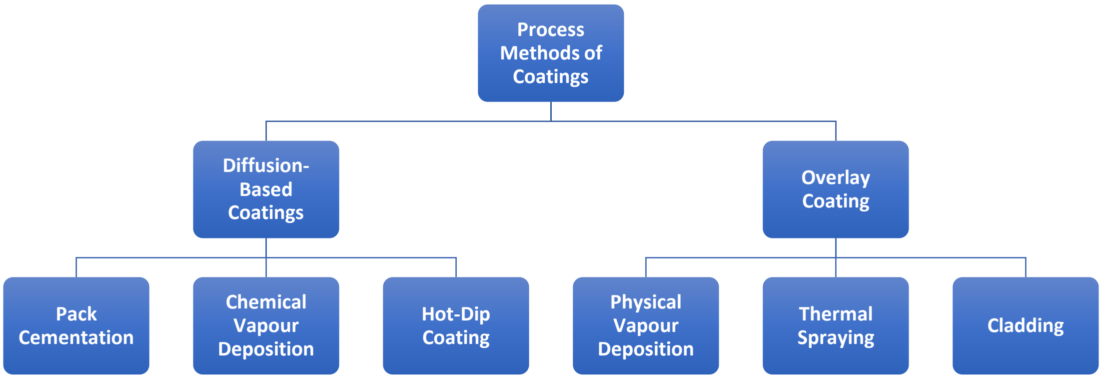

Figure 3.9 : Schematic illustration of coating methods.

3.2.1 Diffusion coatings process methods

3.2.1.1 Pack cementation

Pack cementation is an efficient coating method that includes advantages of diffusion mechanism with the help of heating. Substrate is embedded to box with specifically aluminum basis powder mixture according to desired surface properties. The mixture of powder contains donor for aluminum sources, halides activators and inert fillers such as alumina. After that the box or retort is heated up between 600-1100°C from 2 to 24 hours. The halogen reacts with aluminum to form aluminum halides due to decomposition of halide activator. Those aluminum halides are transported to the surface of the substrate and react with the substrate. Advantages of this coating methods are cheap, reproductible and high deposition rates. On the other side, it has limitation in accordance with coating composition, thickness and pack particles.

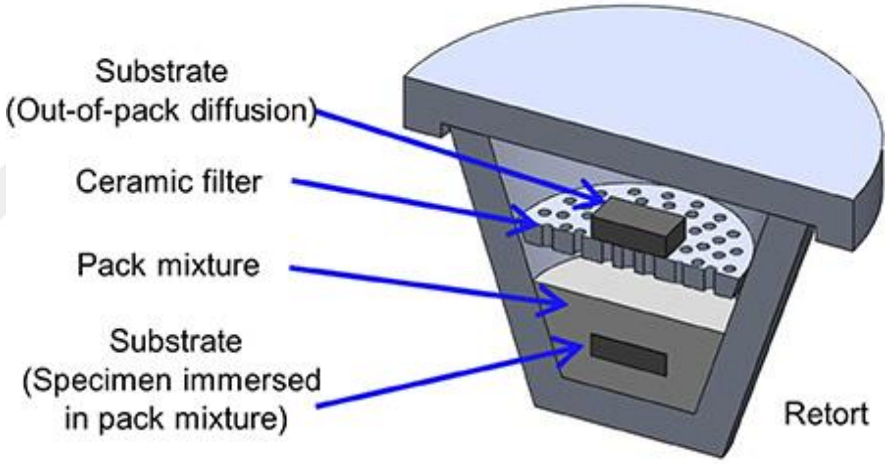

Figure 3.10 : Illustration of pack cementation types [54].

Studies about coating with pack aluminizing has played important role to discover diffusion mechanism and nickel-aluminides coatings behavior to obtain protective oxide layer against harmful environments [36,37,38].

Examples of some studies' microstructural analyses of coated samples that are subjected to pack cementation were shown below.

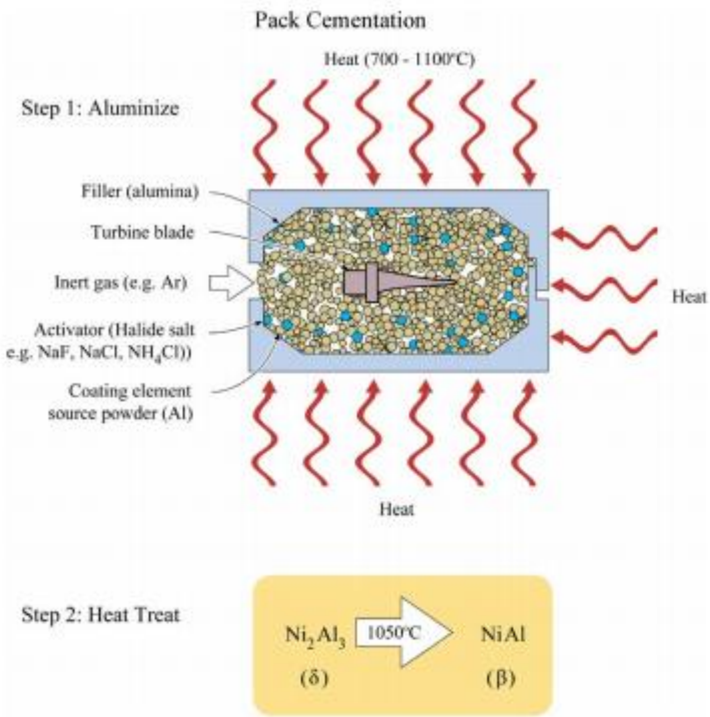

Figure 3.11 : A schematic illustration of the pack cementation process [58].

The cross-sectional microstructure image of scanning electron microscope and linescan energy-dispersive X-ray spectroscopy analyses were shown in Figure 3.12. Commercial nickel-base superalloy Mar-M246 were coated via halide activated pack cementation (HAPC) with using a powder mixture of 25 wt.% pure Al as master alloy and 75 wt.% Al_2O_3 as inert filler. Sample subjected to 700°C for 9 hours. The pack was activated using anhydrous NH4Cl [59]. In this study, oxidation behavior of pack cementation, as a diffusion coating depending on coating temperature and nature of elements in composition, were investigated on account of coating thickness, phase transformation, defects etc.

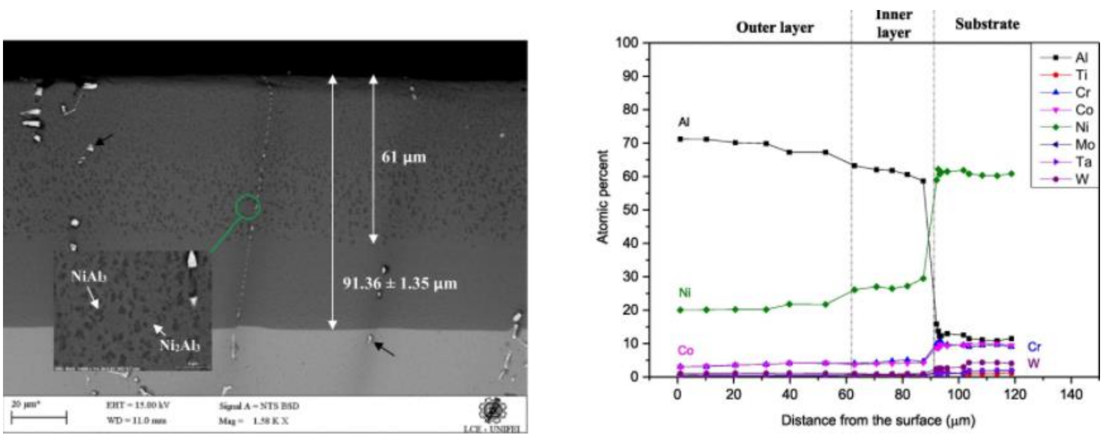

Figure 3.12 : SEM micrographs (left) and corresponding profiles of the alloy elements across the coating by EDS analysis (right) [59].

There is another study about low-temperature formation of aluminide coatings on Ni-based superalloys by pack cementation process. Cross-sectional microstructure image of pack aluminized Ni-based superalloy named K3 were shown in Figure 3.13 [60].

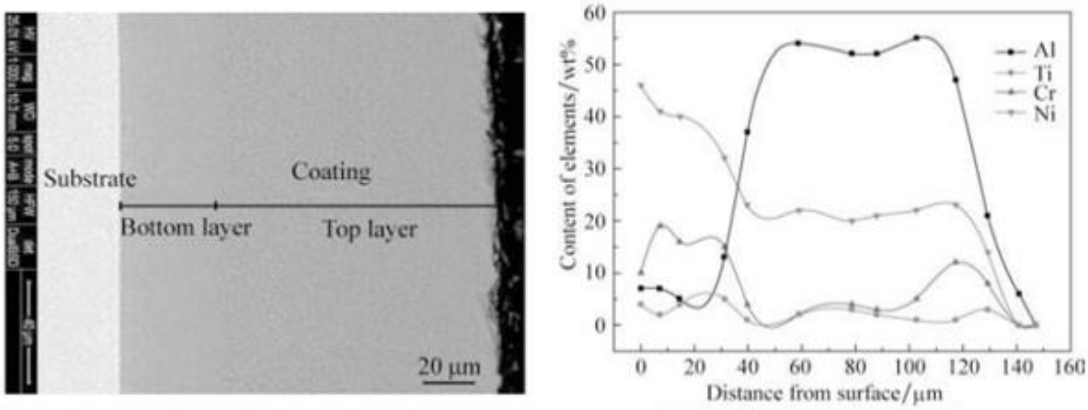

Figure 3.13 : The cross-sectional microstructure image of scanning electron microscope (left) and linescan energy-dispersive X-ray spectroscopy analyses (right) [60].

3.2.1.2 Chemical vapor deposition

Chemical vapor deposition (CVD) is a process to coat substrate by solid material, nanowire a with reactive species in the gaseous phase [61]. Typical CVD system is schematically shown in Figure 3.14.

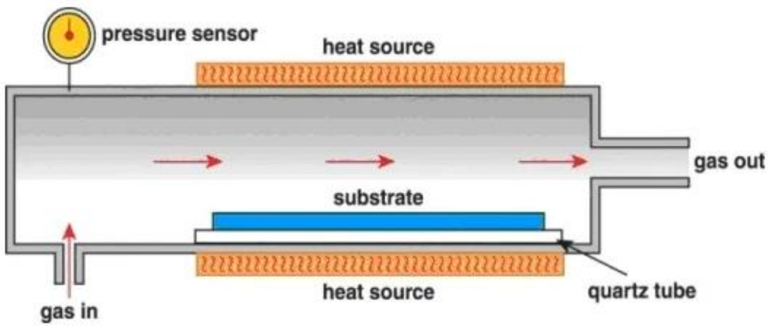

Figure 3.14 : Typical CVD reactor [61].

CVD process has good advantages like, good control on coating thickness, no requirement of additional heat treatments due to ability of post coat heat treatment in reactor which leads to low activity behavior. On the other side, it has disadvantages like, requirement of external source, slow deposition rates and high cost [61]. CVD processes generally differ in how chemical reactions are initiated. Basically, CVD process can be classified operating conditions, physical characteristics of vapor, type of substrate heating, plasma methods etc.

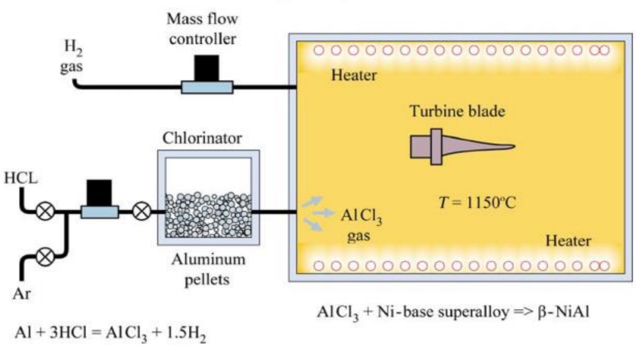

Figure 3.15 : Illustration of the low-activity CVD process [58].

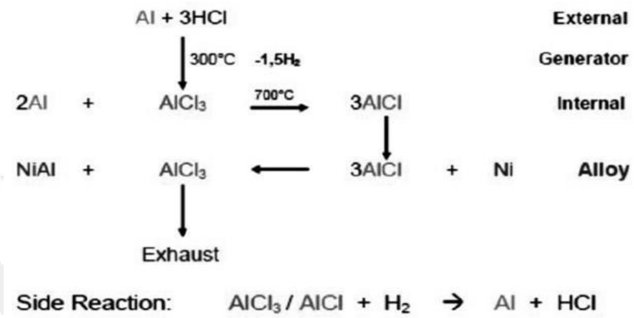

Figure 3.16 : A schematic illustration of the low-activity CVD process [58].

Examples of some studies microstructural analyses of coated samples that are subjected to CVD were shown below.

This study is about oxidation behavior of aluminide deposited by CVD nickel-based superalloys.

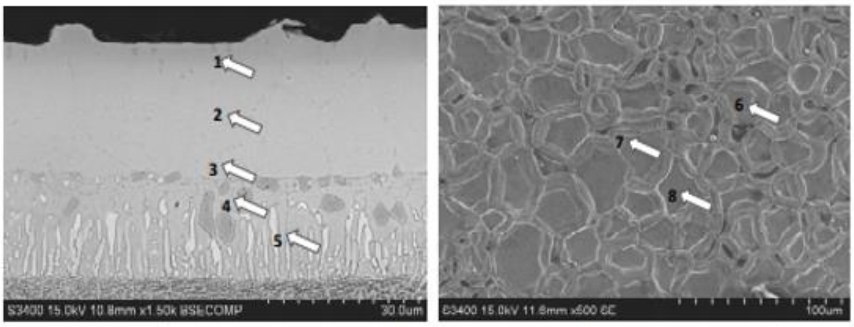

Area	Elements content, % at					
	Al	Ti	Cr	Mo	Ni	Pt
1	40.16	-	2.50	0.41	52.51	4.42
2	32.32	-	6.62	0.71	50.22	10.13
3	30.41	0.49	8.96	0.65	50.52	8.97
4	25.55	0.48	17.38	2.36	44.40	9.83
5	29.03	1.10	9.27	1.02	52.36	7.22
6	40.47	-	1.30	0.32	55.88	2.03
7	41.04	-	1.40	0.13	54.48	2.95
8	38.75	-	2.58	0.23	56.26	2.18

Figure 3.17 : Microstructure CVD aluminizing process on Inconel 713 LC Ni-base superalloy with point EDS analysis [62].

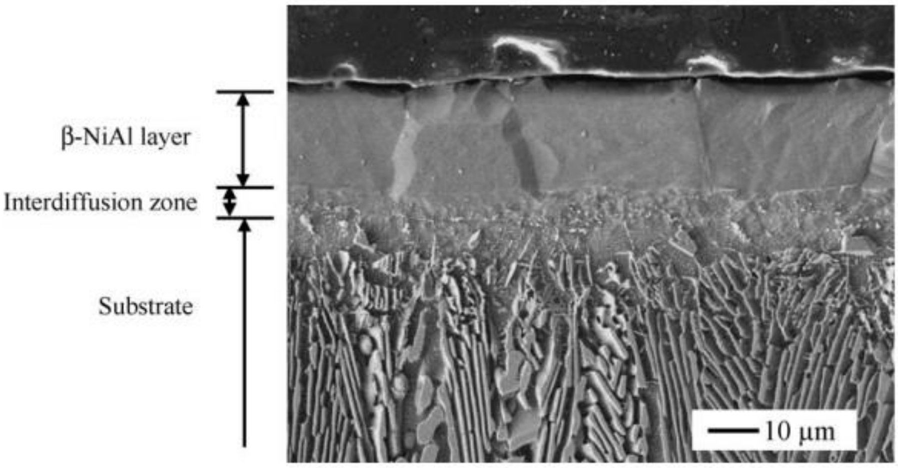

Figure 3.18 : SEM image of NiAl coating deposited at 1000°C [58].

3.2.1.3 Hot-Dip coating

Different types of traces have been come out throughout history of hot-dip coating. First precursor traces have been indicated that hot-dip coating has been developed to protect steels from harmful environments by immersing the steel to molten zinc until 18^{th} century.

Hot-dip coating method were basically carried out by immersing substrate to molten bath. Molten metal bath for hot-dip coating contains different types of metals (i.e. aluminum, zinc). Aluminum application of molten bath is to be referred as hot-dip aluminizing. Hot-dip aluminizing (HDA) is a popular type of hot-dip coating method which has a wide usage area of coating superalloys. Figure illustrates processes of hot-dip coating.

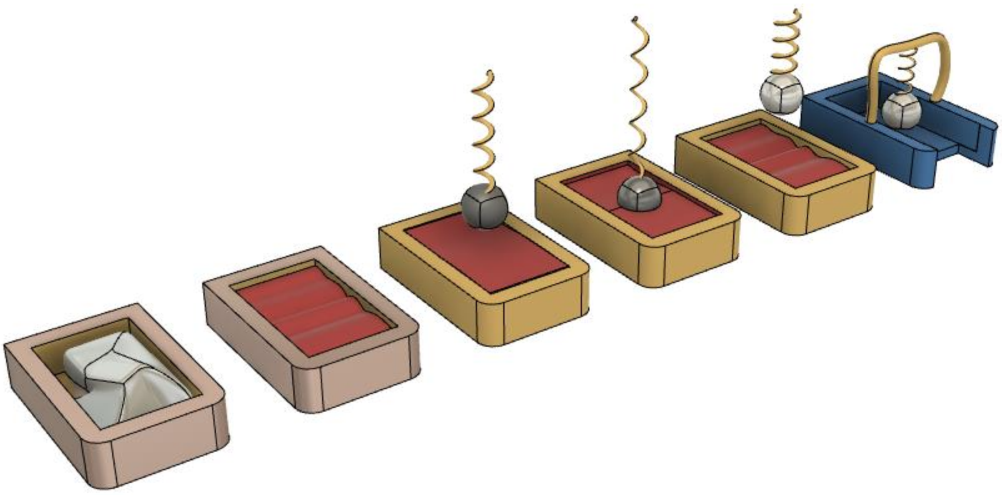

Figure 3.19 : Steps of hot-dip coating.

Steps of hot-dip coating were sorted in Figure 3.19 and 3.20. Steps are ingots melting, preparing bath (with fluxes), sample preparation, dipping, cooling and finishing process from left side to right side.

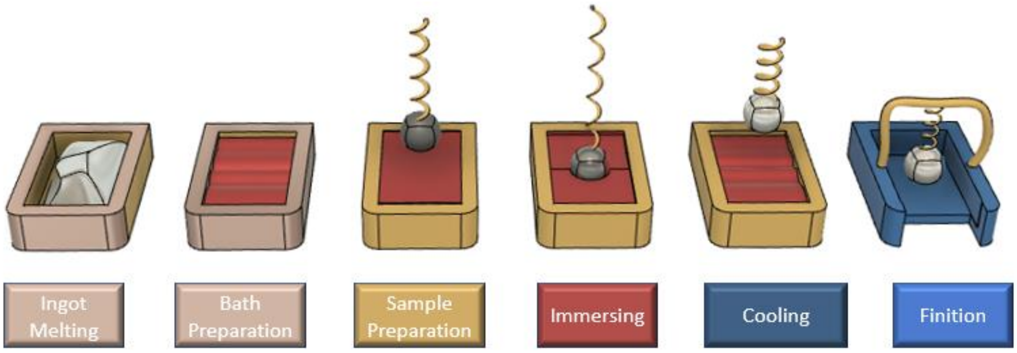

Figure 3.20 : Step Names of hot-dip coating.

There is an inevitable fact that aluminum takes advantage of nickel-aluminide phases, especially for Ni-based superalloys. Also, the applicability of low melting point and adjustable composition of molten bath has both exhibited distinctive properties. Moreover, Al has not the only capability to form a protective aluminum-oxide layer on the surface, but also create proper structure on the surface with the help of diffusion mechanisms. These kinds of coating tend to improve surface properties corresponding to diffusion, overlay and thermal barrier coating. Advantages of hot-dip aluminizing could simply be summarized as low capital and operating cost, large parts applicable, competitive speed of coating and thick coating for longer resistance. On the other hand, it has limitations such as the danger of high temperature and shrinkage of aluminum during solidification. Requirement of heat treatment stands out to improve surface quality after hot-dipping as long as modification were needed by diffusion mechanism.

There are many precious studies about HDA on nickel [63], chromium [64], titanium[65][66], iron[67] and their alloys [68][69]. Additionally, HDA of Ni-based superalloys has been studied in the last few decades [34][35].

Various types of microstructure based on diffusional mechanism coating for aluminizing by hot-dipping were shown below.

In the Figure 3.21, hot-dip aluminized Inconel 718 cross-section and surface morphology images were given with XRD patterns.

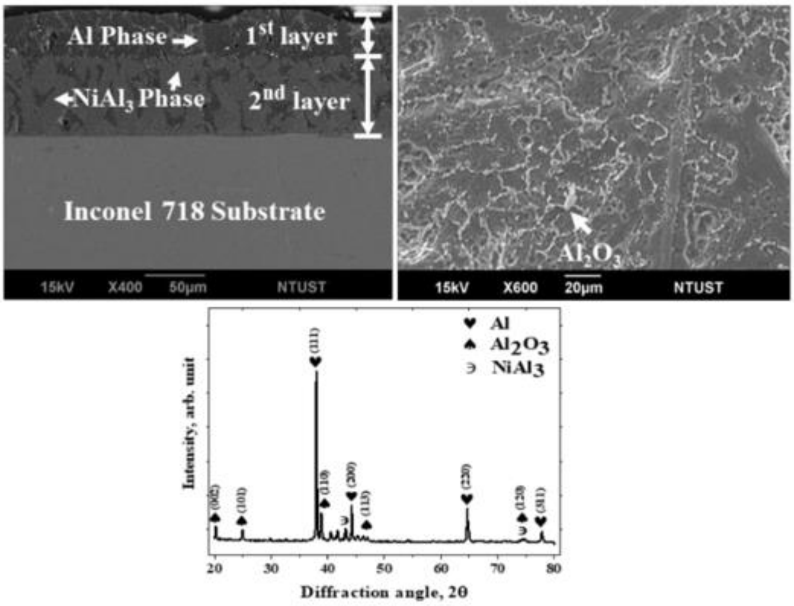

Figure 3.21 : SEM image of cross-section, surface morphology and XRD pattern of hot-dip aluminized alloy IN 718 [36].

Figure 3.22 shows cross-sectional microstructure of hot-dip aluminized Inconel 718 from another study about HDA that is presented below [35].

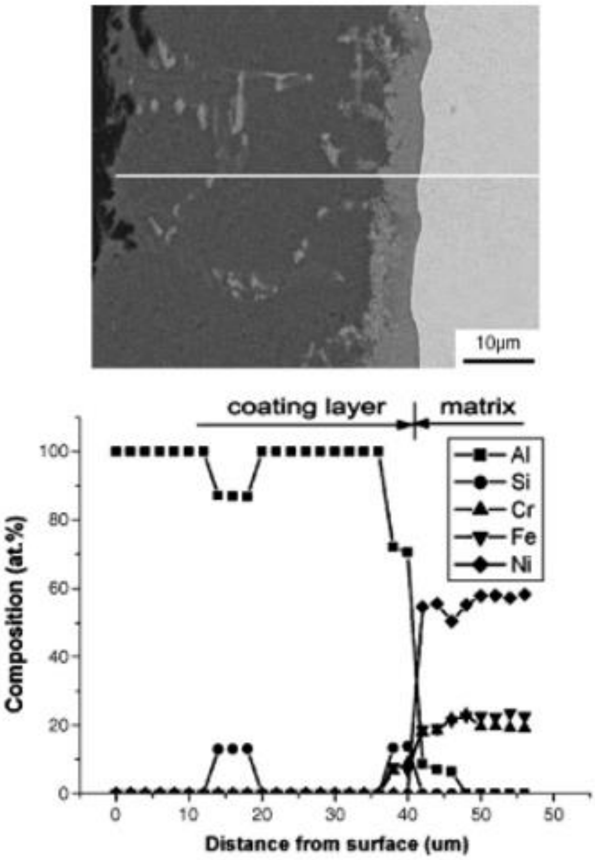

Figure 3.22 : The cross-sectional microstructure and compositional profile of the aluminide layer [35].

3.2.2 Overlay coatings process methods

Overlay coatings are mainly produced by physical vapor deposition and spraying methods. There are some methods that are used for applying the overlay coatings such as electron beam- physical vapor deposition (EB- PVD) and thermal spraying techniques.

3.2.2.1 Physical vapor deposition

The physical vapor deposition (PVD) is a coating method by evaporating or splashing material using the cathodic arc source of the solid coating material in a vacuum chamber. Although PVD coating are widely used to improve hardness, wear resistance and corrosion resistance, some disadvantages such as high operation cost, low coating rate and limited coating area can be obstacle for this method. PVD system is schematically shown in Figure 3.23.

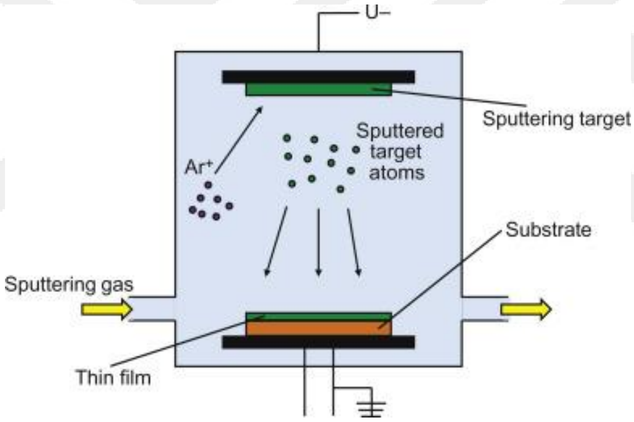

Figure 3.23 : Schematic illustration of the physical vapor deposition process [44].

Electron beam- physical vapor deposition (EB- PVD) method is used for high-quality coatings. Figure 3.24 shows that EB-PVD coating structure, columns has advantage to reduce radiative heat transfer and thermal conductivity [70].

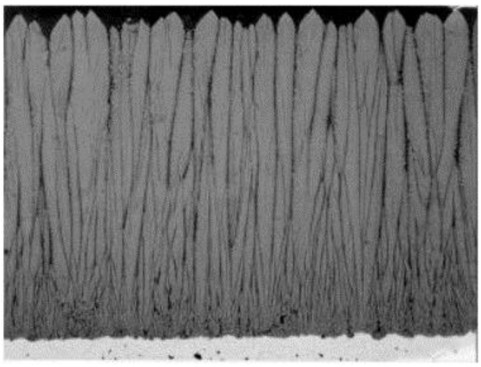

Figure 3.24 : EBPVD coated microstructure [70].

3.2.2.2 Thermal spraying

Thermal spraying is a coating technology for a wide range of materials and components [71]. This method has capability to enhance resistance to wear, erosion, corrosion, abrasion or heat. There are significant advantages about thermal spraying process that are low heat input, versatility, processing speed. On the other hand, thick coatings are difficult to achieve as well as low degree of adhesion (spray efficiency) on small substrates and substrates with small curvature.

There are some specific coating process methods for thermal spraying techniques to obtain MCrAlX structure such as atmospheric plasma spraying (APS), vacuum plasma spraying (VPS), high- velocity oxy fuel (HVOF) and low-pressure plasma spraying (LPPS). Different thermal spraying method were studied. Comparison of microstructure of CoNiCrAlY bond coatings prepared by different thermal spray processes are given in Figure 3.25. The mass gain by isothermal oxidation test 100 hours in air at 1100°C is indicated that LPPS<HVOF<<APS[72].

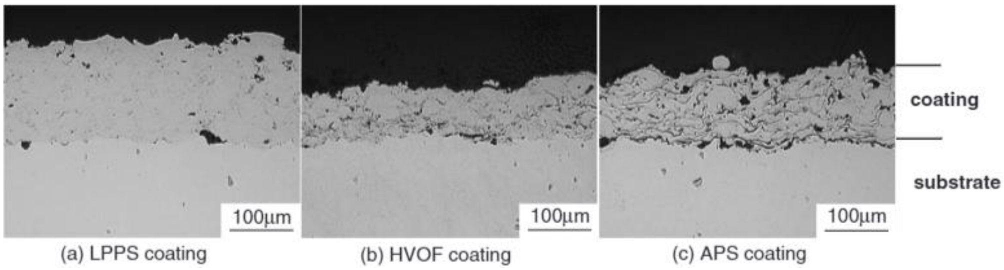

Figure 3.25 : Different microstructures of thermally sprayed substrates [72].

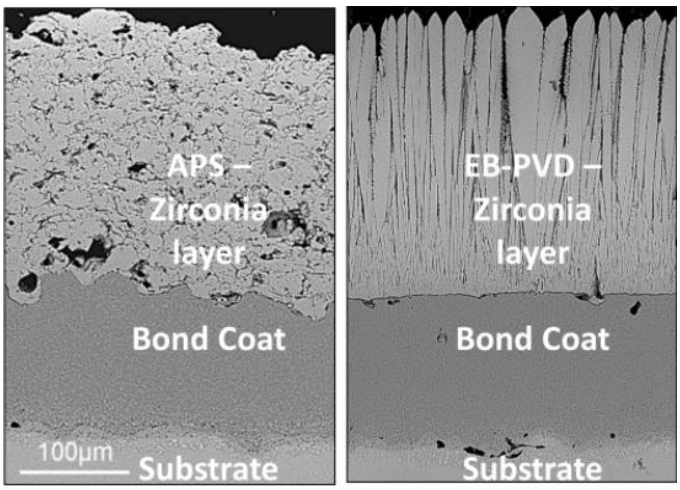

Figure 3.26 : Comparison of TBC systems which are APS-sprayed zirconia (left) and EB-PVD zirconia (right). The bond coats were made by spraying for APS and pack-cementation for EB-PVD [44].

4. TRIBOLOGY AND HIGH TEMPERATURE OXIDATION

Since official introduction of the word “tribology” in the 1960s, tribologists has urgently been focused on the urgent industrial problems. Concurrently, wear and friction mechanisms, surface technologies, lubricants and lubrication methods has been studied to improve. Largely thanks to tribology, the motor vehicles fuel consumption has nearly halved with twofold power increase in the last few decades [73].

Recently, according to researches by various organizations, one third of the energy produced in the world is destroyed by friction-induced losses, which leads to economic losses [74]. In order to prevent these losses, the components that make up the tribological system that is running are well recognized and necessary measures should be taken.

In various industries of engineering components material loss based on wear is significantly high. To enhance the service life of several engineering components, surface modification techniques are applied to improve their wear resistance [71].

Tribology is a branch of science and engineering disciplinary that mainly focuses on interacting surfaces in relative motion including academic fields such as physics, chemistry and material science. In the nature of tribology, there are several characteristic keys to understand tribology systems that are friction, lubrication and wear.

When two surfaces are in contact move relative to each other, friction between surfaces leads to transformation of kinetic energy to thermal energy. Although high friction force is needed for some applications, limitation of friction force must attentively be determined to design systems.

Lubrication is a common way to reduce friction and keep wear mechanism under control by adding any fluid material that is characterized by viscosity, even such as air and water.

Wear is simply defined as material loss resulting from transferring of material from a surface to another surface or the formation of wear parts. Material loss through a solid piece may be in the form of a physically separation of atoms and/or chemical degradation.

Basically, wear types are mainly examined in four different groups: adhesive wear, abrasive wear, fatigue wear, corrosive and erosive wear.

4.1 Wear Mechanisms

4.1.1 Adhesive wear

Adhesive wear is a mechanism resulting from the contact of asperities on the surface Adhesive wear mechanism, showed in Figure 4.2, is usually observed as transition from soft material to hard material [75].

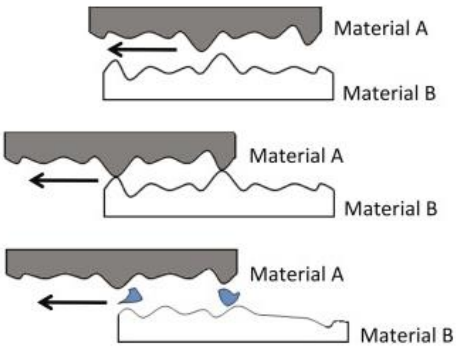

Figure 4.1 : Adhesive wear mechanism illustration [10].

Adhesive wear can be decreased with presence of solid lubricants, lower loads, harder rubbing materials.

4.1.2 Abrasive wear

Abrasive wear occurs when a harder material removes material from a softer material by rubbing. Abrasive wear not only occur between two rough metal surfaces as two body wear but also come about with trapped hard particle that ruptured from hard metal in the form of three body wear [75][76]. Illustration of abrasive wear mechanism were shown in Figure 4.3.

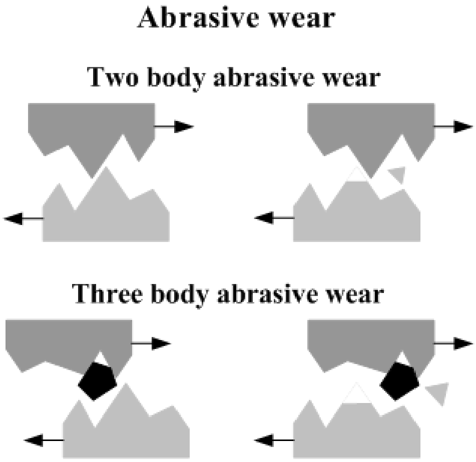

Figure 4.2 : Abrasive wear illustration [10].

4.1.3 Fatigue wear

Fatigue wear initiate with the formation of internal cracks in the surfaces of the materials that exposed to repeated periodic loads in the subsurface and surface area. The fatigue wear is not generally considered as detrimental as abrasive and adhesive wear although there is a wear based on stress. Fretting is one form of fatigue wear resulting from a cycling sliding in a small amplitude. Other form of fatigue wear is caused by crack propagation through the intermediate layer leading to total removal of the overlay [76].

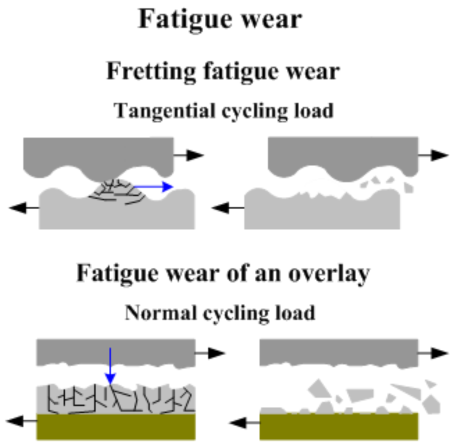

Figure 4.3 : Fatigue wear mechanisms illustration [71].

4.1.4 Corrosive wear

Oxidation may occur along surface with the effect of heat resulting from wear and friction. Oxidized hard particles removed from surface can increase the wear rate when they are between the sliding surfaces, and this is called three body wear. When the metal beneath the oxide layer is low or the load is relatively high, plastic deformation occurs on the metal below the oxide layer [71]. Figure 4.5 shows corrosive wear mechanism.

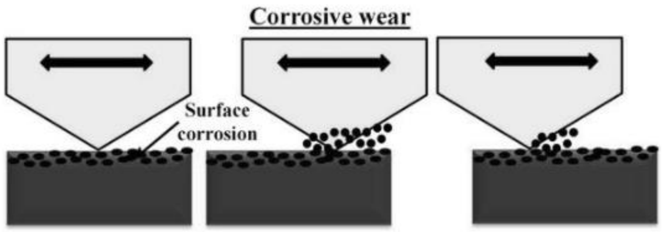

Figure 4.4 : Corrosive wear mechanism illustration [71].

4.1.5 Erosive wear

Erosive wear is caused by impact of the particles to the surface, and removal of materials in the form of fragments from the surface [76]. Erosive wear is affected by many factors including hardness and shape of the particles, impact velocity and angle. [71]. Erosive wear mechanism is schematically given in Figure 4.6.

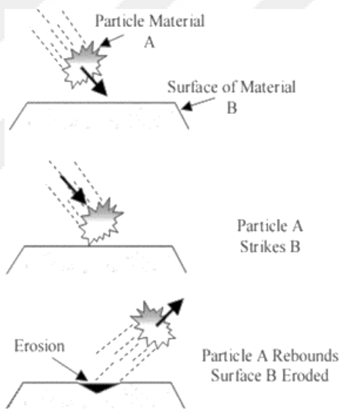

Figure 4.5 : Erosive wear mechanism [71].

4.2 High Temperature Oxidation

Oxidation of metals or alloys occurs when they are heated in highly oxidative atmosphere such as air or oxygen. Basically, oxidation is an interaction between metal and oxygen that forms an oxide. Material degradations at high temperatures take place when temperature increases with the chemical interaction of metal with the environment as well as due to loss in mechanical properties [77]. During high-temperature oxidation, scale forms at the surface in a gaseous environment, and corrosion phenomena takes place between the metal and the oxygen in air at high temperatures [78].

Density of oxide scales on the surface can increase oxidation resistance of superalloys. According to literatures, it is obvious that thermodynamically stable Al_2O_3,Cr_2O_3 and SiO_2 are required during oxidation process that should generate these oxides [35]. With the increase of working time and temperature, many oxide scales that are subjected to oxidation tend to lead spallation. Internal oxidation forms acicular morphology inner oxides during high temperature oxidation. For this reason, it was widely reported that internal oxidation causes crack initiations [79,80]. Some oxides that tend to become larger as the temperature increases could be hazardous due to reducing bonding strength.

4.2.1 Types of oxide layers

Pilling Bedworth ratio (P-B ratio) is a basic ratio to comprehend how elements reacts when they exposed to oxidation. It is a simple ratio between the volume of oxide to metal. Depending of their P-B ratio, oxides can be classified as protective and non-protective oxides. Protective oxide scales are non-porous in structure and can prevent penetration of oxygen to the metal surface, while non-protective oxide scales can give easy access for oxygen transportation due to their porous structures. Simply, adherent and non-porous protective oxide occurs when volume of metal is not more than the volume of oxide form of metal. However, when the oxide has a volume more than two times that of metal, compressive stresses can be generated to form cracks in the oxide structure, which can lead to rapid penetration of oxygen.

4.2.2 Internal oxidation

Oxidation of an element in an alloy is called as internal oxidation. Internal oxidation occurs when matrix oxygen diffusivity is greater than that of the alloying element, which has higher oxygen affinity than the matrix metal. Internal oxidation is important to comprehend oxide scale microstructures of materials such as metals, alloys and composites. Internal oxidation is critical to understand material life by detecting oxidation products and their impact. In order to develop materials for high-temperature engineering applications and optimize the combination of electrical, mechanical and other functional properties, it is analytical to design materials.

5. EXPERIMENTAL PROCEDURES

For this study, Inconel 718 superalloy was used as a substrate. Samples are were firstly coated with hot dipping process in Al-12%Si (wt. %) eutectic alloy bath followed by cooling to room temperature in air. After coating, samples were diffusion annealed in an atmospheric furnace to alter the structure of the coating. Finally, coated and diffusion annealed samples were subjected to sliding wear test and isothermal oxidation tests. As a part of experimental procedures, quantitative and qualitative analyses were done for characterization of processed samples.

5.1 Sample Preparation

Inconel 718 rod were cut to the samples that have 15 mm diameter and 8 mm thickness using a water-cooled abrasive cut-off wheel. Cylindrical samples were abraded to 400 grit SiC papers obtain adequate surface roughness for better adhesion. For dipping, 2 mm diameter stainless steel wire were wrapped around cylindrical samples. Afterwards, samples ultrasonically cleaned with the mixture of 5 vol% HCl in water 2 minutes, dried with ethanol and washed with water. Chemical composition of the Inconel 718 was given in Table 5.1.

Table 5.1 : Chemical composition of the Inconel 718 (wt.%) [81].

Ni	Cr	Fe	Nb	Mo	Ti	Co	Al	Others
52,07	24,14	15,73	5,58	0,98	0,47	0,26	0,24	0,53

5.2 Hot-Dip Aluminizing Process

5.2.1 Aluminum-Silicon eutectic alloy bath

Bare Inconel 718 samples were subjected to hot-dipping process in Al-12Si (wt. %) bath at 700°C for 2 minutes. Temperature parameter of bath was selected to obtain optimal coating thickness [64]. Coating time was adequately chosen to provide smooth and homogeneous surface according to last studies about HDA of Ni ,Cr alloys [63]. MF-1000 electrical furnace, used to melt Al-Si alloy ingots, was shown in Figure 5.1.

HDA temperature and holding time parameters were optionally selected according to recent studies and experiences about nickel-based superalloys [33,34,62]. Aluminum-silicon alloys, with the form of ingot, were used to provide fluidity and perfect surface for bath [35]. After that samples were cooled to room temperature in air. Immersion temperature, holding time and cooling time were arranged according to recent studies about hot-dip aluminizing [64].

Figure 5.1 : MF-1000 electrical melting furnace.

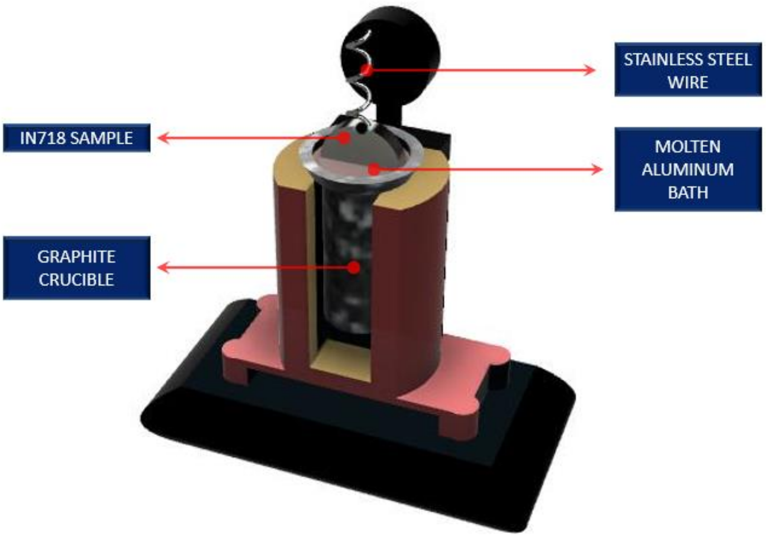

Figure 5.2 : Illustration of parts that used for HDA process.

Molten bath was prepared by using commercial aluminum-silicon eutectic alloy. Prior to melting ingots, 1 cm^3 mixture 40 vol% KCl and 60 vol% NaCl of fluxes were added into crucible to remove slags. The molten Al-Si alloy bath temperature were kept at

700°C. Samples were vertically dipped by hand, then held in center of crucible for 2 minutes. Slags were cleaned before coated samples were taken out.

5.3 Diffusion Annealing

Diffusion annealing process was performed in atmospheric furnace shown in Figure 5.3. Diffusion annealing process were done at 700°C for 10 hours. Afterwards, samples were furnace cooled to room temperature.

Figure 5.3 : Protherm PLF 120/5 annealing furnace.

5.4 Microstructural Examinations

Microstructural images were obtained with Philips XL30 SFEG scanning electron microscope (SEM) equipped with Energy-dispersive X-ray spectroscopy (EDS) analyses for mapping, linescan, frame and point for hot-dip aluminized and diffusion annealed samples. Hitachi TM1000 model SEM were used to analyze wear traces. SEMs were shown in Figure 5.4.

Figure 5.4 : Philips XL30 SFEG (left), Hitachi TM1000 (right) scanning electron microscope.

5.5 XRD Analysis

X-ray diffractometer analyses were performed in GBC MMA 027 model XRD device using CuKα shown in Figure 5.5.

Figure 5.5 : GBC MMA 027 model XRD device.

5.6 Microhardness Measurements

Microhardness measurements were done with using a force of 25 g as Vicker's Hardness Tests (HV 0.025) . The microhardness device is shown in Figure 5.6. For each region, at least 5 measurements were taken, their average was reported.

Figure 5.6 : Wilson Tukon 1102 Microhardness Test Device.

5.7 Surface Roughness

Surface roughness of HDA and HDA+DA samples were measured by Mitutoyo Surftest SJ-400 surface roughness tester that shown in Figure 5.7.

Figure 5.7 : Mitutoyo Surftest SJ-400.

5.8 Wear Test

Ball-on disc tribometer (CSM-High Temperature) were used to carry out wear tests shown in Figure 5.8. Linear speed was arranged as 5 cm/s. Ball dimension was 6 mm diameter. Wear test were carried out in air atmosphere with the 25% humidity.

Figure 5.8 : CSM-High Temperature.

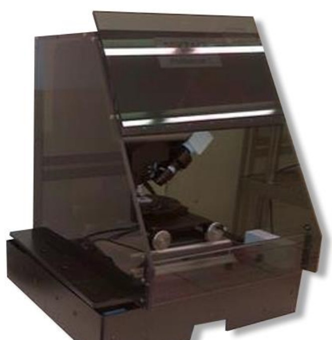

Figure 5.9 : Veeco Dektak 6M.

2-D stylus type surface profilometer (Veeco Dektak 6M) is used to analyze width, area and depth of wear and shown in Figure 5.9. Additionally, the worn surface of the samples was investigated by SEM (Hitachi TM1000). Optical microscope (OM, Leica DM750M) was used for the investigation of the contact surface of the alumina ball counterface.

Table 5.2 : Parameters of high temperature tribometer.

Parameters	Ball-on-disc
Counterface	Alumina ball (6 mm in diameter)
Total Sliding Distance	100 m
Testing Load	2 N
Testing Temperature	25°C, 300°C, 600°C

5.9 Oxidation Test

Prepared samples were subjected to high temperature oxidation test in steam and carbon dioxide in a specially designed, closed loop test rig PRC 110M/GWP (Czylok, Jastrzębie Zdrój, Poland). Steam flow were arranged as 50 g/h. Argon -18% CO_2 flow rate was arranged as 0.026 l/h. Figure shows that illustration of the steam oxidation rig used for the oxidation experiments.

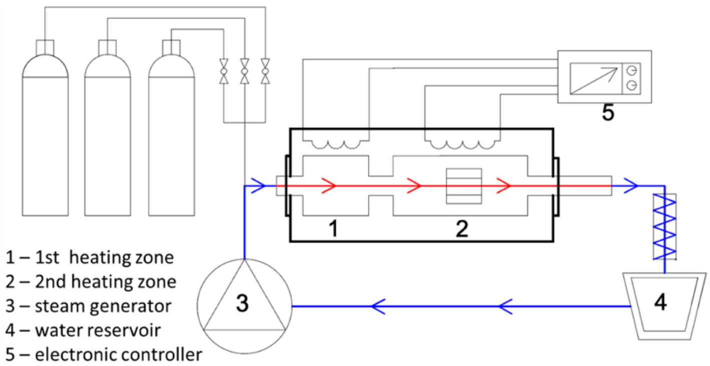

Figure 5.10 : Illustration of the steam oxidation rig.

6. RESULTS AND DISCUSSIONS

In this part, quantitative and qualitative analysis results on hot-dip aluminized (HDA), hot-dip aluminized plus diffusion annealed (HDA+DA) and Inconel 718 samples (BARE) were presented. Microstructural images of optic microscope and scanning electron microscope (SEM) with Energy-dispersive X-ray spectroscopy (EDS), X-Ray Diffraction (XRD) pattern and hardness measurements were obtained.

6.1 Hot-Dip Aluminized Sample

6.1.1 Microstructural examinations

Cross-Section microstructural image of SEM was show in Figure 6.1. Basically, various type of zones can be seen due to diffusion mechanism such as interdiffusion layer, middle layer and outer layer. Thickness of outer layer, middle layer and inter-diffusion zone were approximately measured as 20-25 μm, 20-25 μm and 8-10 μm respectively. Average total coating thickness and interdiffusion zone thickness were measured approximately 50μm.

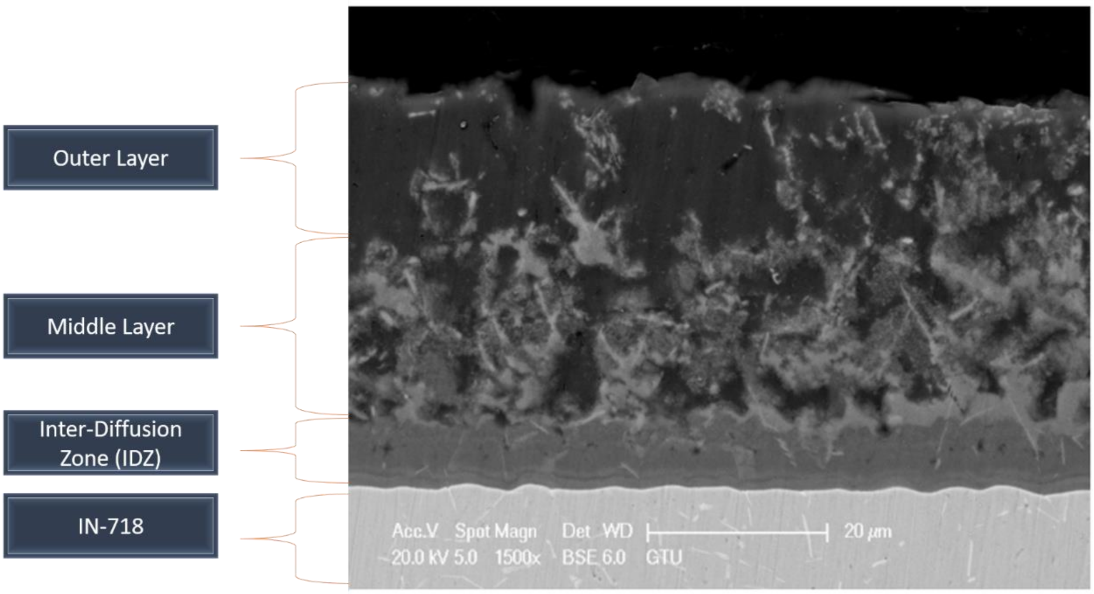

Figure 6.1 : Cross-sectional scanning electron microscope image of hot-dip alumized sample.

Microstructural characterization of HDA samples were done by SEM with back scattered electron mode. According to image, there can be respectively seen three zone which are IN718 substrate, inter-diffusion zone, middle and outer layer from bottom to top. Movement of interface between coating and substrate became drastically significant to understand the diffusion mechanism phenomena of elements with variable time and temperature. According to similar studies, coating thickness and inter-diffusion zone were observed compatible [35]. It was observed that higher silicon content draws attention in gray colored region. Using silicon in aluminum coating for hot-dip aluminizing is beneficial in the meaning of fabricability and drawability [82]. The Al-Si coating provides better thermal oxidation resistance than that of the pure Al coating due to the formation of a more compact Al_2O_3 layer [83]. Additionally, silicon in aluminum coating tends to promotes formation of Al_2O_3 [84].

There is a simple technique that allow to observe interface movement. Half part of sample was vertically dipped into Al-Si eutectic molten bath and held as illustrated in Figure 6.2. Blue object referred cylindrical sample that will be dipped. Red part illustrated molten bath for dipping. Outer gray layer referred graphite crucible.

Figure 6.2 : Illustration of half-part dipping.

Figure 6.3 shows that cross-sectional microstructure image of half-part dipped sample. All the layers and zones were clearly indicated. As a fact, there can be easily seen the inter-diffusion zone (IDZ) between coating and substrate that follows the coating interface.

IDZ has drastically exhibited that there is a compatible balance about inward diffusion of Al and outward diffusion of Ni atoms. Movement of interface ,between coating and substrate, will be expected to penetrate directly into substrate after diffusion annealing of HDA samples with appropriate temperature and time. IDZ were appeared beneath the substrate meaning that inward diffusion of aluminum occurred.

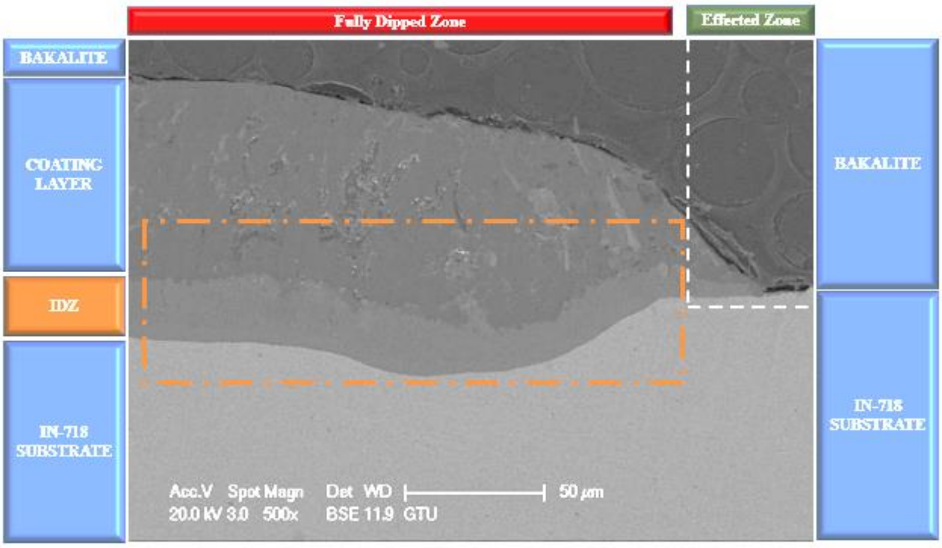

Figure 6.3 : Half-part dipped samples SEM image

6.1.2 Energy dispersive X-Ray spectrometry analyses

EDS analyses of the hot-dip aluminized sample was shown in Figure 6.4, 6.5 and 6.6.

<u>Point EDS analyses</u>

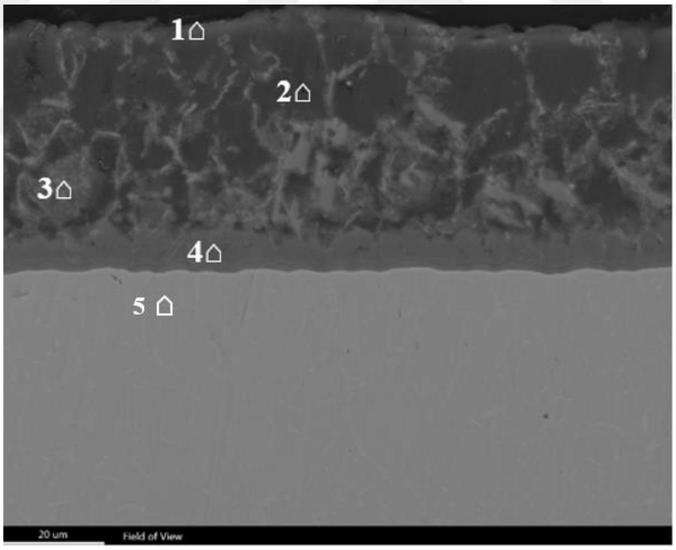

Chemical Composition (in at. %)

Point	Al	Ni	Cr	Si	Fe	Nb	Mo	Ti	O
1	95,2	0,3	0,1	2,4	0,1	0,1	0,1	0,1	1,6
2	94,7	0,3	0,2	3,9	0,1	0	0,1	0,2	0,5
3	76,9	4,6	3,5	12,5	0,4	1,5	0,6	0,9	1,2
4	56,6	8,1	8,7	12,6	6,8	1,0	0,8	0,7	0,7
5	1,2	51	31,4	1,5	18,4	2,6	1,3	1,3	1

Figure 6.4 : Point EDS analyses of hot-dip aluminized (HDA) sample.

According to analyses, dark regions (Location 1) mainly contain Al with presence of Si. In the middle layer of coating homogenous distribution of elements (Al, Si and Cr) was observed even if spot points exhibit low content of Mo, Nb and other elements coming from substrate. Outward diffusion was proven with the data of point EDS analysis. Al is the main element to supply oxidation resistance for hot-dip aluminized sample due to content of Cr have not exhibit proper composition in coating, particularly on the top of surface. It was observed that, IDZ zone (Point 4) contains mainly Al, Ni, Cr, Si, Fe elements as expected.

Linescan EDS analyses

Figure 6.5 show linescan EDS analyses. Results showed that content of Al is nominally decreasing from top of coating surface to substrate. Major contents of Al were observed in the outer layer, likewise contents of Si were higher close to middle layer. Linescan analysis were compatible with the study about hot-dip aluminizing of Inconel 718 especially for elemental content of regions [35].

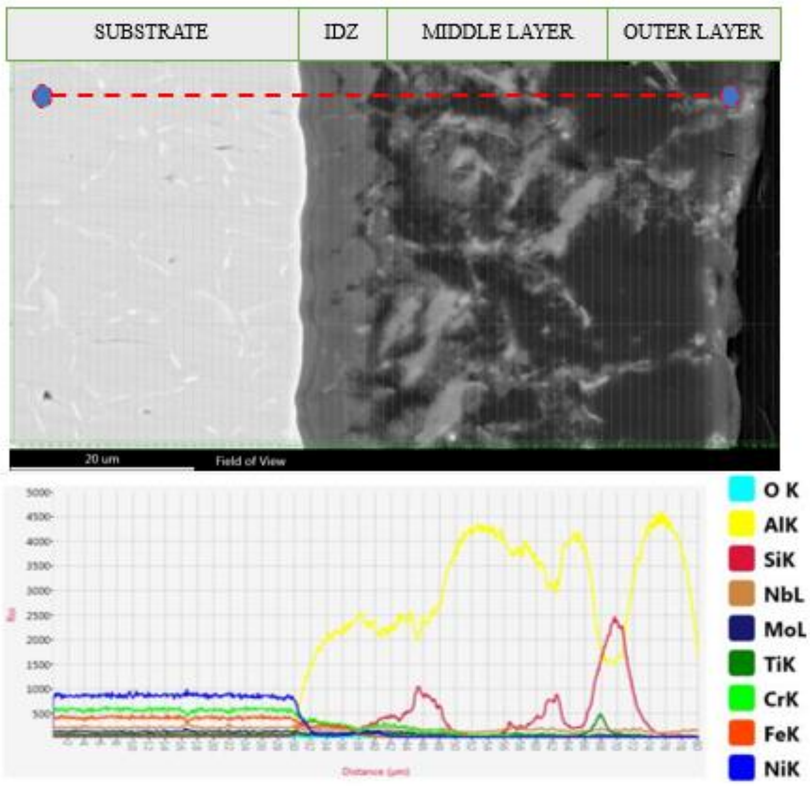

Figure 6.5 : Linescan EDS analyses.

According to intensity of elements, minor content of Cr is observed in middle layer. Nickel contents were not show up in the outer and middle layer, yet minor contents of nickel close to interdiffusion zone were detected.

Mapping EDS analyses

Elemental EDS mapping analyses were given in Figure 6.6. According to EDS results of elemental mapping of the hot dip aluminized sample, Al was mostly found in outer and middle layer. Intensity of Ni and Fe did not provide certain information because they are mainly found in substrate, but intensity of Ni and Fe in inter-diffusion zone is not neglectable. Cr has showed up among coating layers that has possibility to affiliate to Aluminum. Mapping EDS analyses were relatively found to be compatible with the point and linescan EDS analyses.

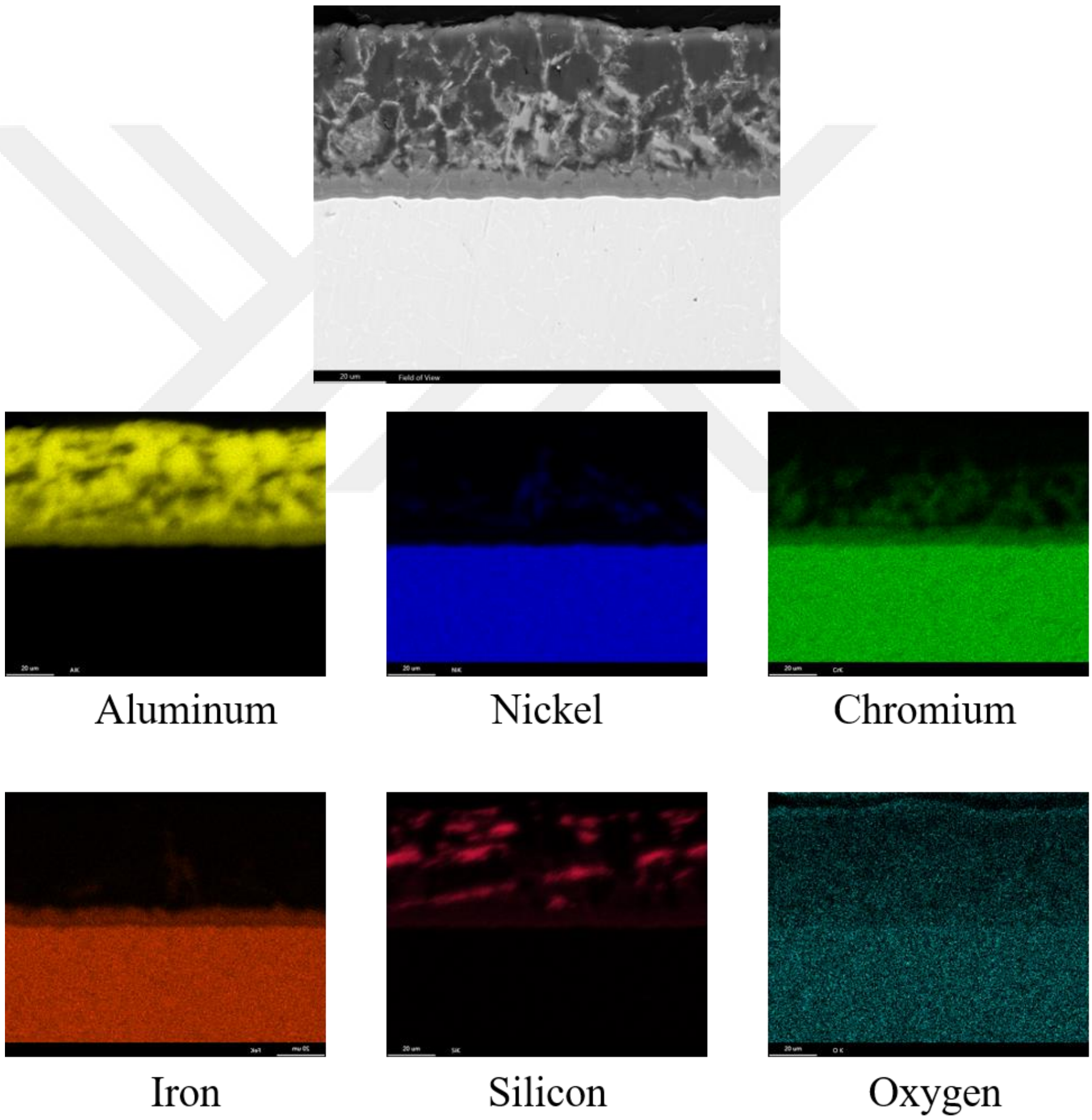

Figure 6.6 : Elemental EDS mapping analyses.

6.1.3 X-Ray diffraction analyses

XRD analyses results of bare Inconel 718 and as-aluminized sample were shown in Figure 6.7. In the XRD pattern, solid solution peaks belonging to substrate are clearly shown. XRD results proved that outward diffusion of Ni to coating surface has occurred composed of Ni_2Al_3 and $NiAl_3$. As expected, although Al elements were mainly detected in the peaks, outward diffusion of chromium were showed up with silicon in form of Cr_3Si.

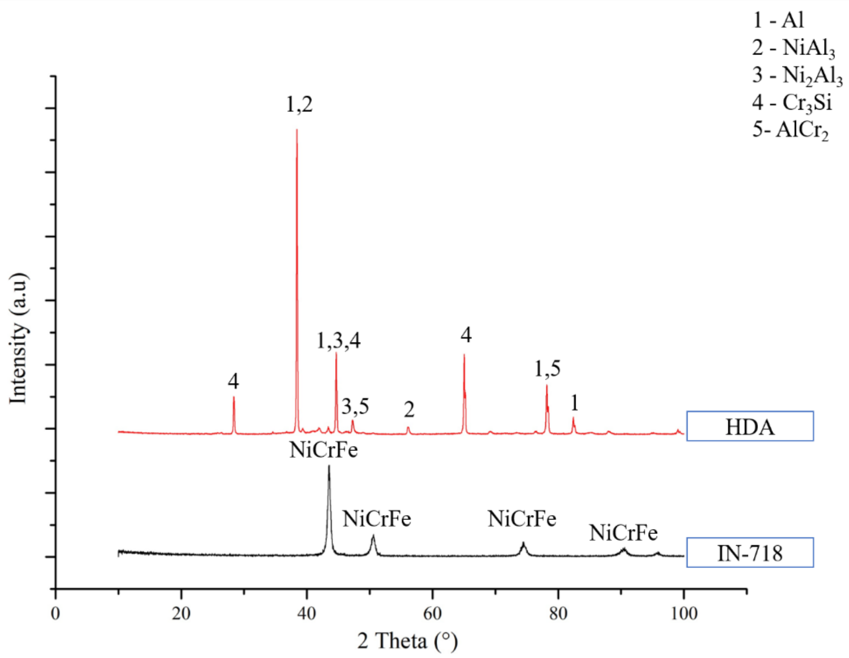

Figure 6.7 : XRD patterns of bare Inconel 718 and hot-dip aluminized sample.

SEM images and EDS analyses has supported that the main idea of diffusion coating occurring with the adequate temperature and sufficient time. XRD results has consistently showed hot-dip aluminizing has rapid diffusion mechanism compared to other types of coating methods.

6.1.4 Microhardness measurements

Hardness values of each zone were measured at least 5 times which was showed in Figure 6.8. Outer and middle layer of coating were expected low hardness value compared to interdiffusion zone (IDZ) and IN718 substrate. While the hardness test has been carried out, the IDZ has been detected to scarcely measured due to thinner thickness compared to other layers. Therefore, the load was properly decreased to measure fittingly.

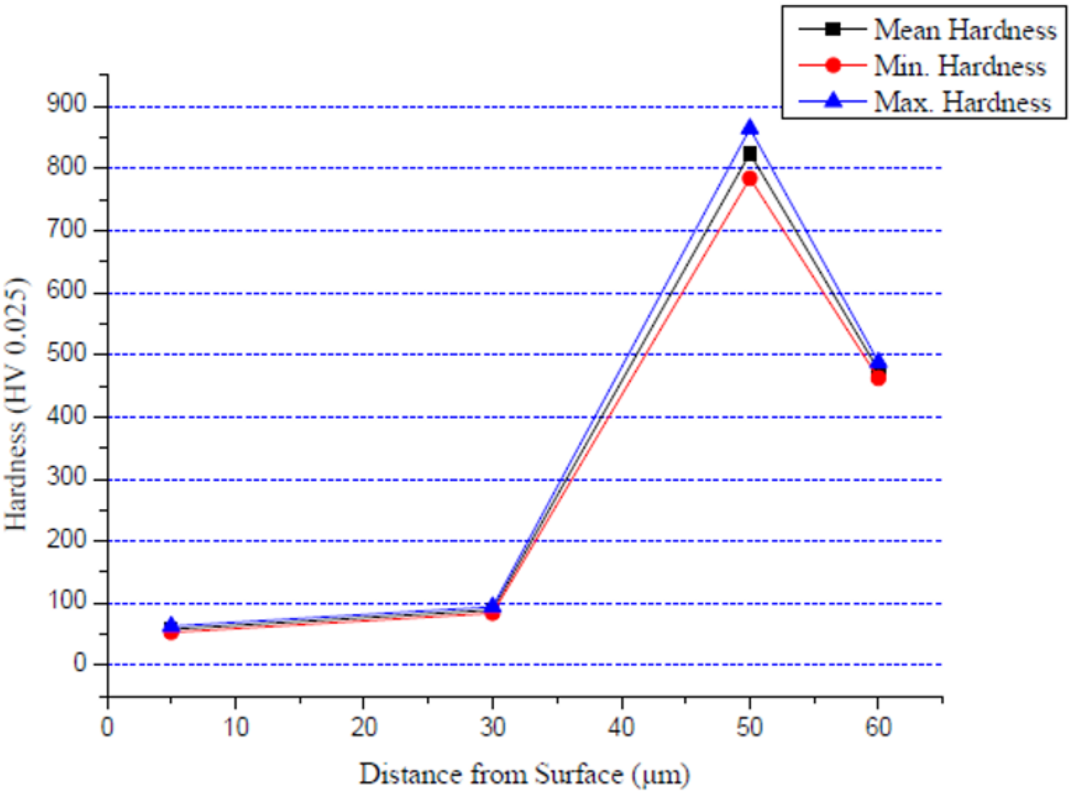

AREA	HV 0.025
Outer Layer	58,5±5
Middle layer	89±5
Inter-Diffusion Zone	824±40
IN718 substrate	475±13

Figure 6.8 : Hardness results of hot-dip aluminized sample.

Reasonably, different types of phases formation such as presence of $NiAl_3$ phases and Al-Cr intermetallics has caused to increase hardness values as a result of diffusion mechanism with time and temperature. Solidification and growth direction of aluminum has minimally effected hardness measurements according to grain size and distribution [85].

6.2 Aluminized and Diffusion Annealed Sample

Aluminized samples were put into furnace to be heated 700°C for 10 hours then furnace cooled to room temperature. Furnace heating rate was measured as 12°C/min.

6.2.1 Microstructural examinations

Cross-Sectional SEM image of hot-dip aluminized and diffusion annealed sample (HDA+DA) was shown in Figure 6.9. There can be seen different types of layer from substrate to top of coating. Cumulatively and directionally dispersion of elements that are coming from the substrate have capability to increase number of layers with respect to various types of properties via diffusion annealing temperature and time. Thickness of coating were measured approximately 200 μm.

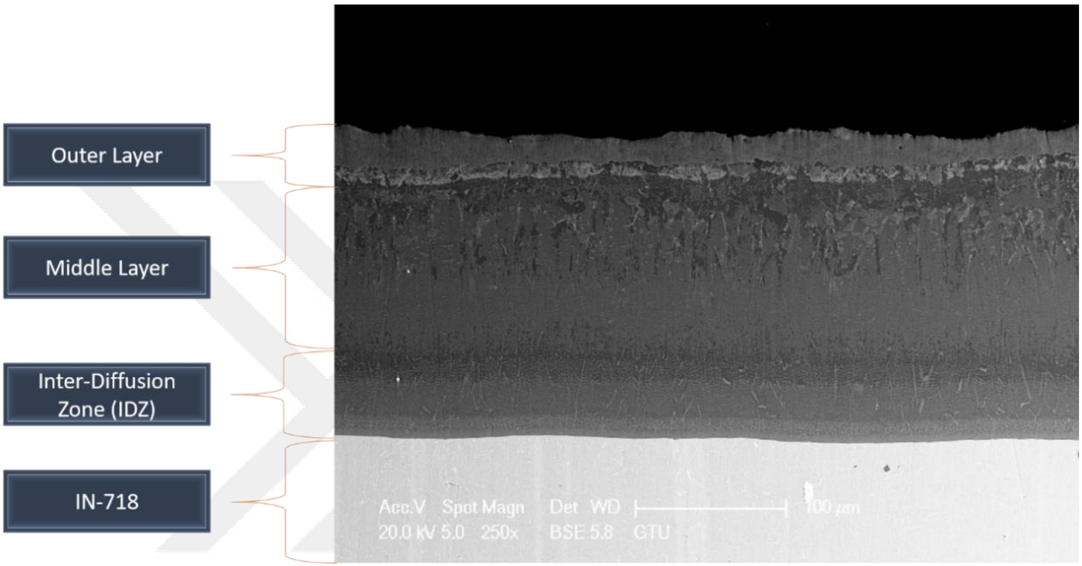

Figure 6.9 : Cross-sectional scanning electron microscope image of hot-dip alumized and diffusion annealed (HDA+DA) sample.

Kirkendall porosities are usually observed beneath original interface in case of faster outward diffusion of Ni than inward diffusion of Al [86]. Yet, after diffusion annealing process, porosities were not observed in areas close to inter-diffusion zone.

6.2.2 Energy dispersive X-Ray spectrometry analyses

EDS analyses of the hot-dip aluminized sample was shown in Figure 6.10, 6.11 and 6.12.

Point EDS analyses

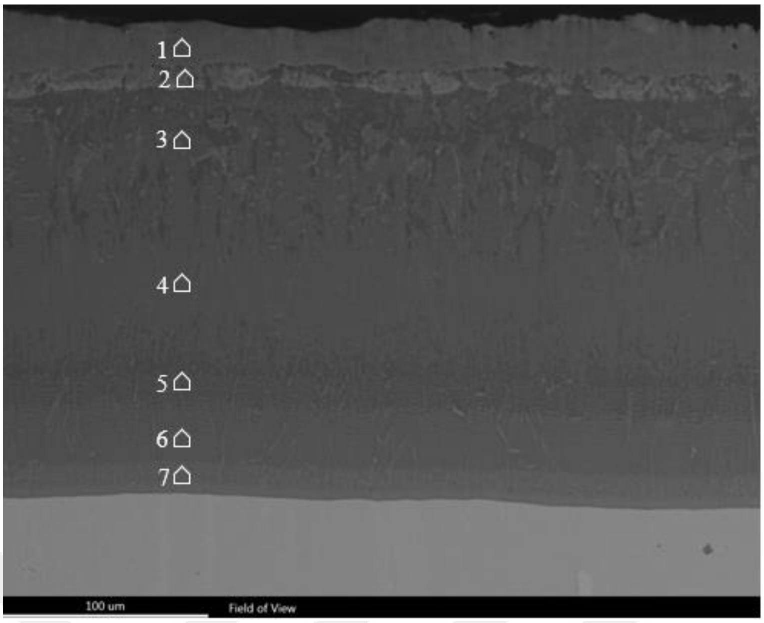

Chemical Composition (in at. %)

Point	Al	Ni	Cr	Si	Fe	Nb	Mo	Ti	O
1	12,4	0,6	38,6	40,1	0,6	0,2	4,4	1,7	1,4
2	46,3	2,9	20,2	16,9	5,6	1,8	1,9	3,3	1,1
3	57,7	12,5	12	5,5	10,1	0,5	0,5	0,4	0,8
4	48,8	25,3	6,4	9	8,2	0,8	0,2	0,5	0,8
5	53,3	22,6	7,9	4,7	7,7	1,9	1	0,5	0,4
6	49,3	23,1	9,3	4,7	9,3	2,3	1,2	0,5	0,3
7	45,7	28,0	10,2	1,8	10,0	2,4	1,2	0,6	0,1

Figure 6.10 : Point EDS analyses of hot-dip aluminized diffusion annealed (HDA+DA) sample.

According to point EDS analysis, distribution of elements has showed various layer. In the inter-diffusion zone, Cr content is low compared to outer layer due to high value of diffusion coefficient. Mullite is a alumina-silica compound and offers high temperature stability, low thermal conductivity, corrosion and oxidation resistance. On the other hand, limitation of mullite are volume contraction and crystallization above

800°C that leads to delamination and cracking [87]. In outer layer Cr, Si, Al contents is higher compared to other zones. Al has preferentially showed up in middle layer of coating and where Ni elements present mostly. Major content of Si atoms is observed in the surface that leads to formation mullite layer to protect layer against oxygen penetration. IDZ contains mostly Al, Ni, Fe.

Linescan EDS analyses

Linescan EDS analyses of HDA+DA was given in Figure 6.11. Analyses showed that outward diffusion of Ni, as a reservoir for aluminum, has relatively been proved according linescan EDS. Similar to nickel, intensity of another element Cr that comes from substrate were mostly detected in near surface. Additionally, Si were observed in areas close to surface.

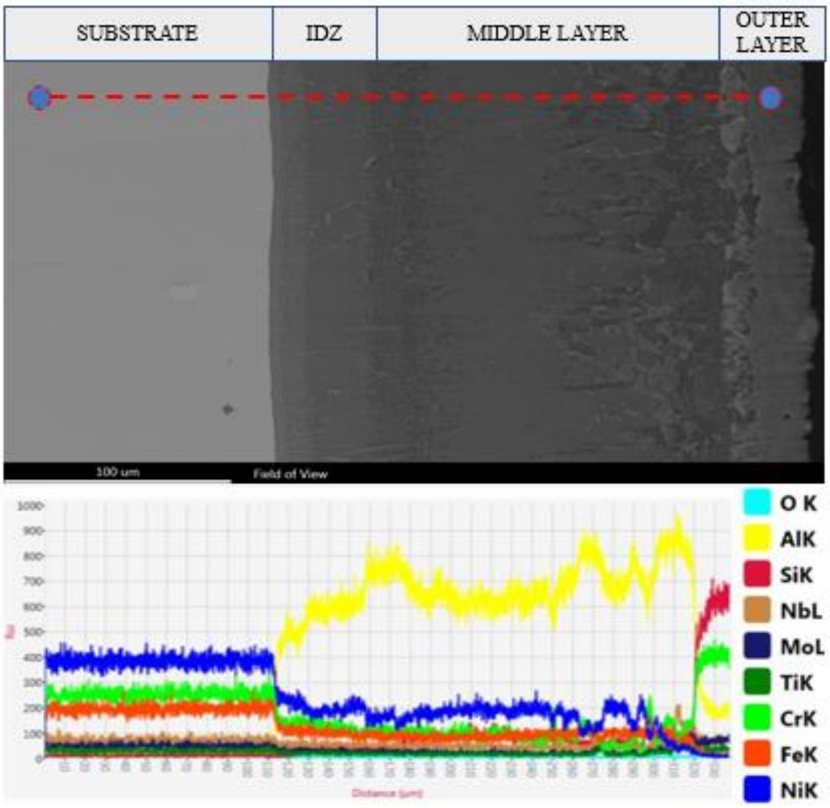

Figure 6.11 : Linescan EDS analyse results.

Nickel, in charge of providing reservoir, has successfully exhibited proper contents with homogeneous distribution through coating layer except in outer layer.

Mapping EDS analyses

According to elemental mapping EDS analyses shown in Figure 6.12, it was observed that Cr and Si has preferentially existed in outer surface. Homogeneous distribution of Si is obtained after diffusion annealing. Nb elements were mostly detected beneath outer oxide layer. In middle layer elemental distribution is seen homogeneous. It was observed that Al and Cr has not tendency to distributed in similar areas.

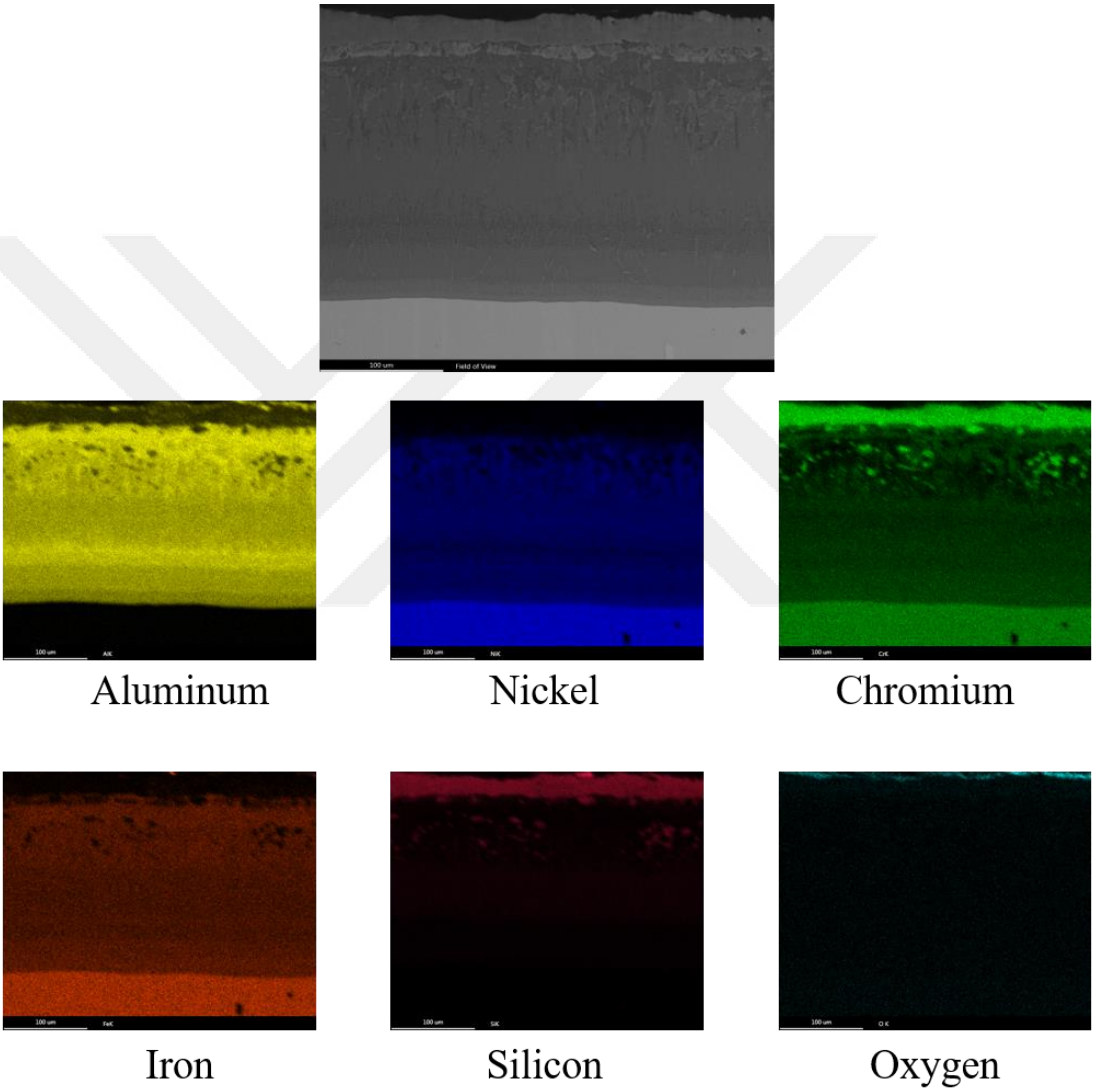

Figure 6.12 : Elemental mapping EDS analyse.

6.2.3 X-Ray diffraction analyses

To examine all of the layer, HDA+DA sample were grinded and again X-ray diffraction pattern were obtained step by step. Sensitive micrometer was used to measure thickness of sample to determinate layers. In Figure 6.13, distance from surface and XRD pattern were shown for HDA+DA sample. As expected, XRD peaks has consistently proved that outward diffusion of Ni has increased after diffusion annealing compared to hot-dip aluminized sample. Nickel-aluminides were observed in form of main precipitation strengthening γ' (Ni_3Al) phases that has advantages of coherency with bare Inconel 718 matrix.

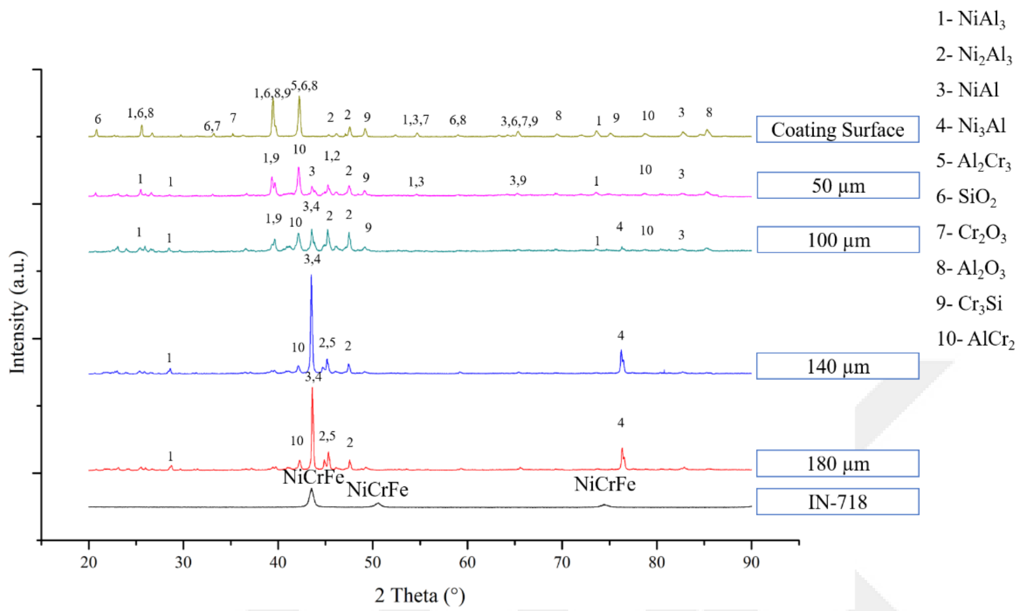

Figure 6.13 : XRD results of bare Inconel 718, hot-dip aluminized sample and diffusion annealed sample

Not only $NiAl_3$ and Ni_2Al_3 peaks were also observed similar to HDA samples, but also the NiAl phases which has highest melting point within Ni-Al phases were detected. According the intensity of peaks close to surface, amount of Al decreased compared to hot-dip aluminized samples due to Cr and Si coming has preferentially tendency to diffuse surface to generate protective oxide scale.

6.2.4 Hardness measurements

Hardness results is given in Figure 6.14. Basically, outward diffusion of nickel to top of surface has been detected according to EDS and XRD results supported by hardness results. Outer layer of surface has shown remarkable rises due to ceramic based phases Al_2O_3, Cr_2O_3, SiO_2. Outer layer IDZ has tendency to exhibit different hardness values due to cumulative distribution of elements. Middle layer exhibit more harder values compared to HDA samples.

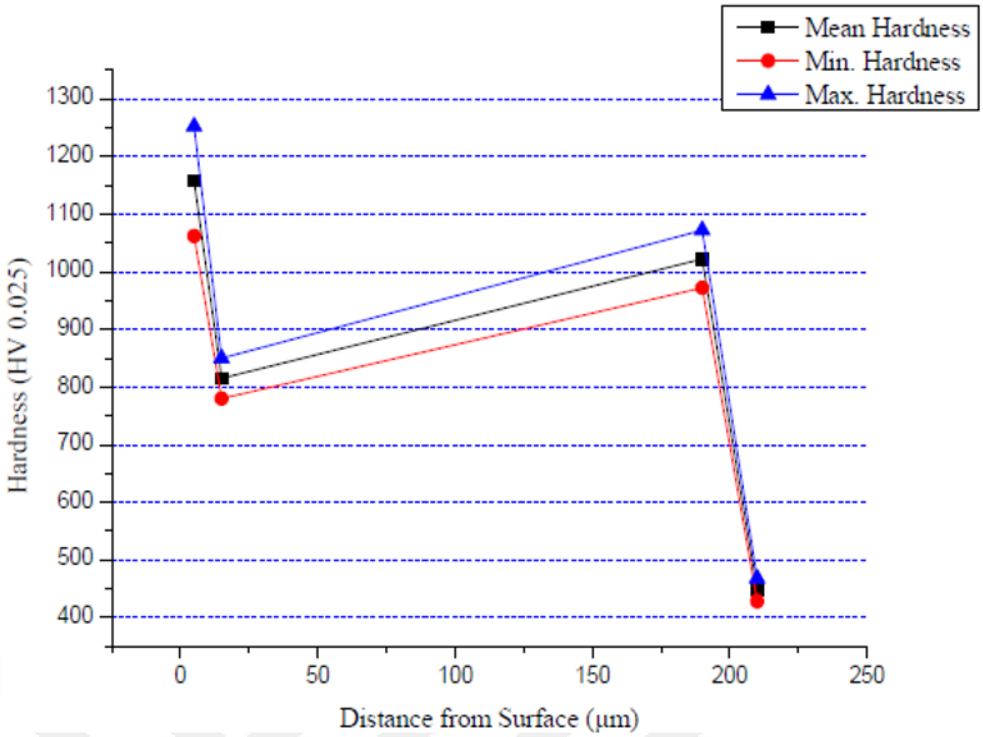

AREA	HV 0.025
Outer Layer	1157±95
Middle layer	815±35
Inter-Diffusion Zone	1022±50
IN718 substrate	448±20

Figure 6.14 : Hardness results of diffusion annealed sample.

6.3 Wear Tests Results

6.3.1 Results of structural analyses

Arithmetical mean wear tracks' depth and width graphs of samples tested at the temperature of 25°C, 300°C and 600°C were given in Figure 6.15. According to samples tested at room temperature, lowest wear width and depth were observed in HDA+DA samples compared to bare and HDA samples by wear tracks taken from 2-D profilometer. In HDA and bare samples, similar depth and width values were detected.

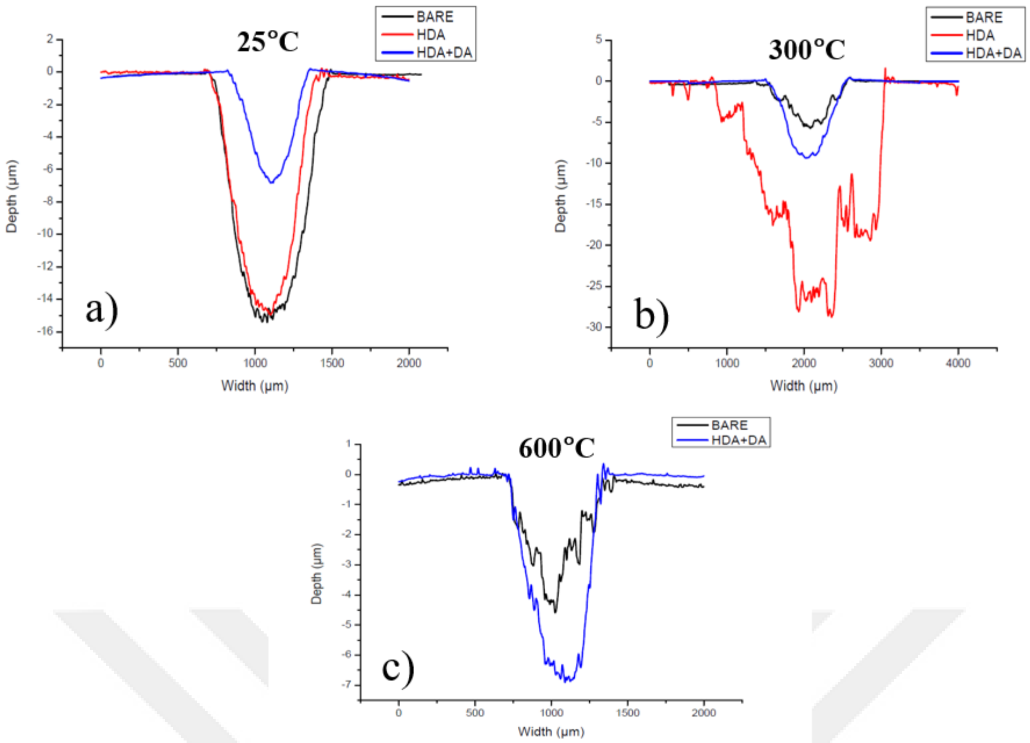

Figure 6.15 : Worn surface depth and width graphs of a) 25°C, b) 300°C and c) 600°C wear tests for bare Inconel 718, HDA and HDA+DA samples.

Highest wear area was detected for bare Inconel 718. 2-D profiles taken from wear tracks of the samples tested at 300°C was shown in Figure revealed that lowest wear depth is observed in bare substrate. Highest wear depth and width was observed for HDA samples among all wear tests. According to samples that tested at 600°C temperature, lower wear width was observed for HDA+DA sample, although bare substrate showed lower wear depth. Also, it was observed that HDA+DA samples tested at 300°C has showed higher wear track depth compared to HDA+DA samples tested at 600°C.

In the Table 6.1, average measurements of wear track width, area and depth were given with wear rate at 25°C, 300°C and 600°C temperature for bare Inconel 718, hot-dip aluminized and hot-dip aluminized plus diffusion annealed samples. 2-D stylus type surface profilometer (Veeco Dektak 6M) is used to analyze.

Table 6.1 : Wear rates and average measurements of wear track width, area and depth.

Wear Test Temp.	Samples	Wear Tracks Width (µm)	Wear Tracks Area (µm)	Wear Tracks Depth (µm)	WEAR RATE $10^{-3}\times(mm^3/N.m)$
25°C	BARE IN-718	661	7340	15,2	0,69
	HDA	589	6210	14,8	0,58
	HDA+DA	443	1992	6,8	0,18
300°C	BARE IN-718	529	2687	7,6	0,25
	HDA	1686	34064	25,7	3,21
	HDA+DA	565,8	3652	9,88	0,34
600°C	BARE IN-718	601	1538	7,1	0,14
	HDA+DA	557	2549	7,3	0,24

At room temperature wear tests, HDA samples wear rate were measured lower than bare Inconel 718. HDA+DA samples showed best performance approximately three times higher than HDA samples. Similar studies have revealed that HDA samples wear rate were lower compared to bare substrate.

At 300°C temperature wear tests, highest wear rate was obtained by HDA samples due to high content aluminum layer that has deleterious effects at high temperature. Yet, HDA+DA samples showed better properties compared to HDA samples, even though wear rate of HDA+DA and bare Inconel 718 is close to each other.

At 600°C temperature wear tests, HDA+DA samples showed diffusion annealing would be necessary for high temperature application of hot-dip aluminizing. Although wear rate of HDA+DA sample tested at 300°C has increased according to room temperature test, nevertheless, sample wear tested at 600°C has showed lower wear rate compared to 300° wear test. Wear rates of the samples were given in Figure 6.16.

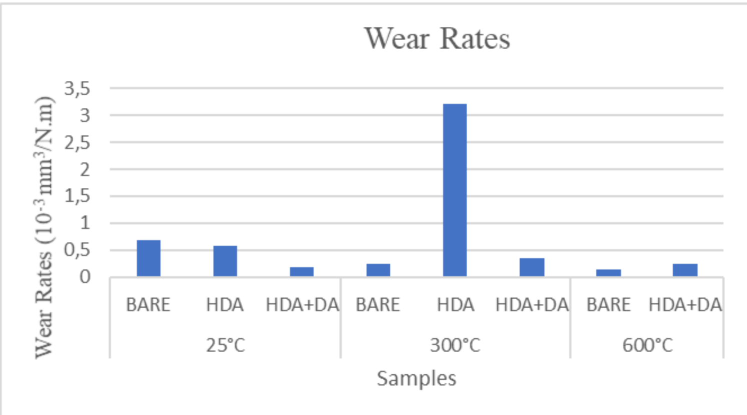

Figure 6.16 : Wear rates of samples.

Advanced three-dimensional profilometer analyses of HDA+DA samples tested at 25°C, 300°C and 600°C were relatively given in Figure 6.17.

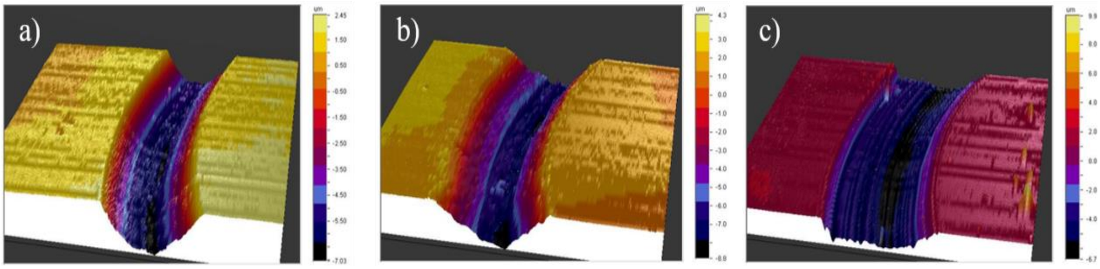

Figure 6.17 : Advanced three-dimensional profilometer analyses of HDA+DA.

6.3.2 Friction coefficient analyses

The friction coefficient and sliding distance graphs which were obtained by ball-on-disc wear tests of the samples at the temperature of 25 °C, 300 °C, and 600 °C were shown in Figure 6.18.

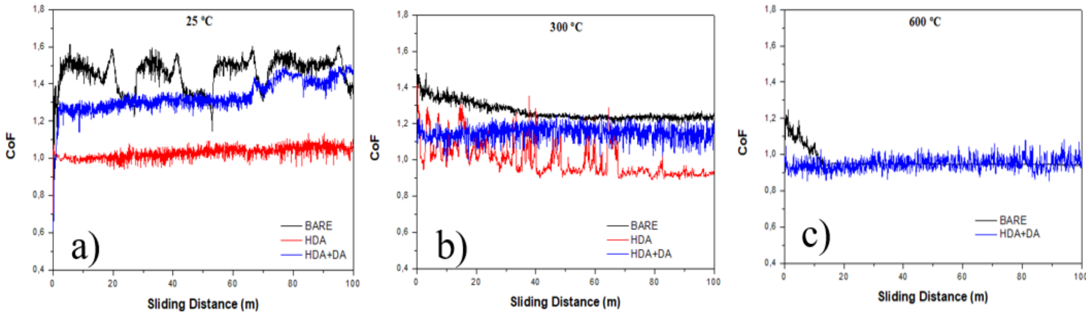

Figure 6.18 : Friction coefficient and sliding distance graphs of a) 25°C, b) 300°C and c) 600°C wear tests for bare Inconel 718, HDA and HDA+DA samples.

For 25°C wear test, in the beginning, sudden rise of CoF (coefficient of friction) can be associated with the cleaning of roughness for bare Inconel 718. Bare Inconel 718 friction coefficient coming from results has showed fluctuation line due to formation and removal of oxide scale in the surface during sliding, as a result of kinetic energy transformation to heat input generated by friction. Incline is occurred when oxide formed on surface. Reversely, decline means oxide scale removals. It is well-known that many studies have indicated that oxides formed during wear reduce the CoF and thus wear rate. Relatively the oxide film formed on surface during sliding play lubricant role [88]. Cr is the main protective oxide former for bare substrate, so it can be inferred that Cr has tendency to form oxide layer then remove. HDA+DA samples has showed increasing friction coefficient through last sliding distances.

Wear tests at 300°C, fluctuated friction coefficient was not detected for bare Inconel 718 compared to room temperature wear tests due to continuous oxide formed by higher temperature. In the beginning of wear test, CoF graph showed decline until 40 meters, afterwards exhibited more straight line. HDA samples showed fluctuated line due to oxide formation and removal. For HDA+DA samples, it was observed that stability of friction coefficient is sustained although temperature is relatively higher compared to 25°C.

Wear test at 600°C, bare Inconel 718 has similarly exhibited moderate decline until 20 meters compared to 300°C wear test. This can be attributed to faster oxide formation by higher heat input. HDA+DA samples has relatively showed lower friction coefficient compared to 300°C that proves diffusion annealing of HDA samples is inevitable at high temperature applications. For HDA+DA samples, stabile friction coefficient was detected with relatively straight line. Also minimum CoF values were detected despite elevated temperature.

6.3.3 Microstructural analyses of wear tests

6.3.3.1 Wear tests at 25°C

SEM images of top view of wear track obtained from 25°C wear tests were given in Figure 6.19. Intense oxide scale formations in the form of granular oxide patches were observed in worn bare Inconel 718. In the rest of oxide area, wear particles could possibly be exposed to rolling that tend to reduce friction coefficient. Rolling of wear particles between the surfaces that are ruptured from materials could provide lower the friction coefficient. Abrasive wear mechanism was detected with the presence of fine abrasive micro grooves. In the worn surface of HDA sample, delamination and flakes were seen. In HDA+DA samples, delamination regions were detected in worn surface. Comparatively, clustered oxide scales in the worn surface of HDA+DA samples were found much lower.

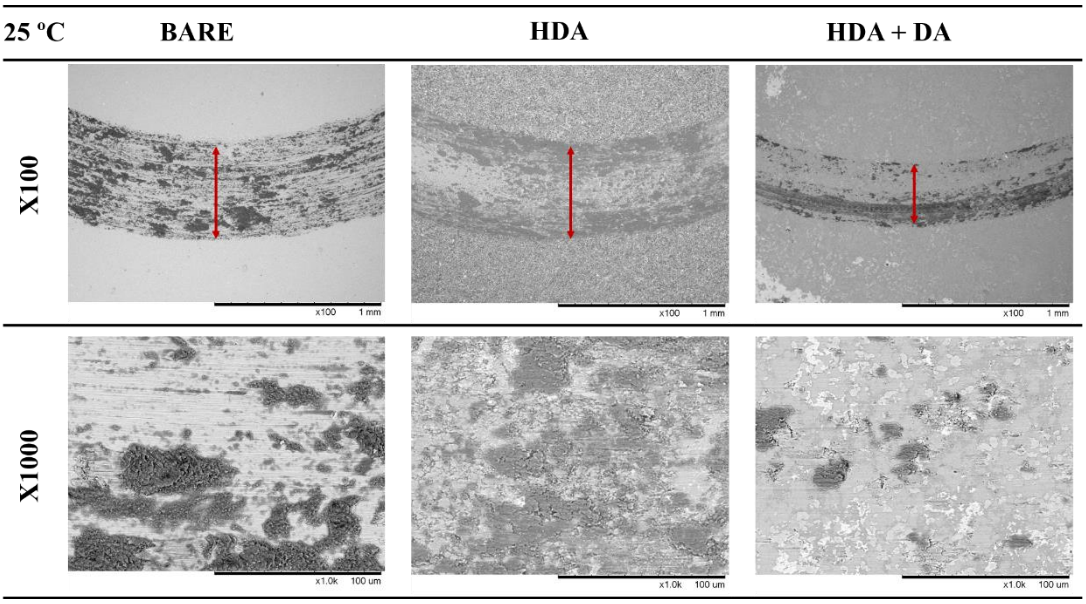

Figure 6.19 : SEM images of top view of wear track of samples tested at 25°C for bare sample , HDA sample and HDA+DA sample.

For wear tests at 25°C, cross-sectional SEM images of bare Inconel 718 wear tracks were shown in Figure 6.20. Protrusions formed on tribo-chemical layer were observed. For bare Inconel, fine oxide scale was observed. Less penetration of abrasive ball to sample can be represented as increase of hardness, thus led to less wear rate [89]. In first frame, crack initiation as shear lip was observed. It is estimated that this oxide scale is composed of chromia shown in second frame. It is obvious that delamination occurred during sliding wear test that showed up in third frame. In fourth frame crack draws attention. Flakes can be seen in fifth frame.

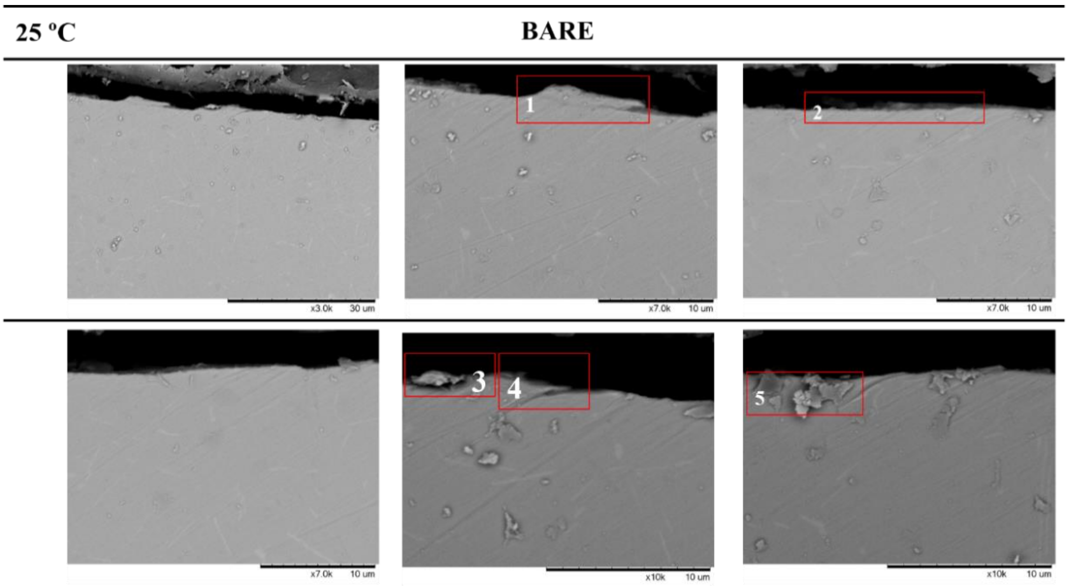

Figure 6.20 : Cross-sectional SEM images of worn surfaces of bare Inconel 718 sample tested at room temperature (25°C).

Cross-sectional SEM images of bare Inconel 718 wear tracks were shown in Figure 6.21. According to first image, it can be seen that abrasive ball almost reached to substrate by passing through coating layer. High amount of delaminated region and chip formation were observed.

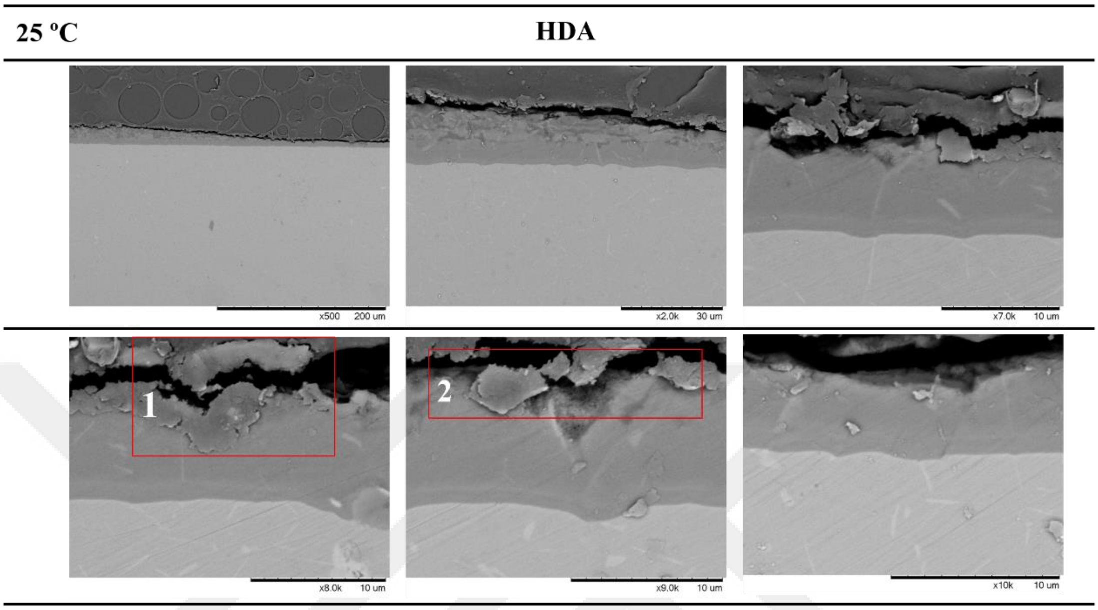

Figure 6.21 : Cross-sectional SEM images of worn surfaces of HDA sample tested at room temperature (25°C).

Cross-sectional worn surface images of HDA+DA given in Figure 6.22 showed that wear depth was not as much as bare and hot-dip aluminized samples. In first frame delaminated region were shown that can be ruptured away. In second frame, discarded chip can be seen that can possibly be called stuck blocky debris defect.

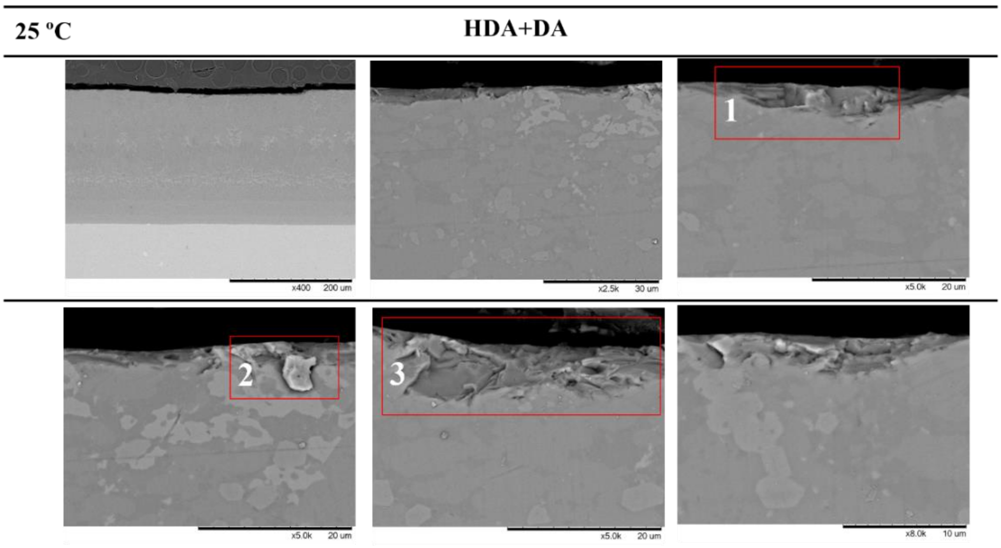

Figure 6.22 : Cross-sectional SEM images of worn surfaces of HDA+DA sample tested at room temperature (25°C).

Point EDS analyses were done for samples that tested at room temperature given in Figure 6.23. According to EDS results, oxygen elements were mostly detected in the dark regions. For bare substrate, it is estimated that oxides were composed of chromium, iron and nickel. Also, highest intensity of oxides was comparatively detected for bare substrate. Lowest oxygen intensity was found in HDA+DA sample for lighter color of wear track SEM images. Additionally, oxide scales were locally observed for bare substrate, while continuous oxide scales were linearly observed for HDA+DA sample. Homogenously distributed oxide scales were found in HDA. Highest content of aluminum was detected in HDA+DA sample.

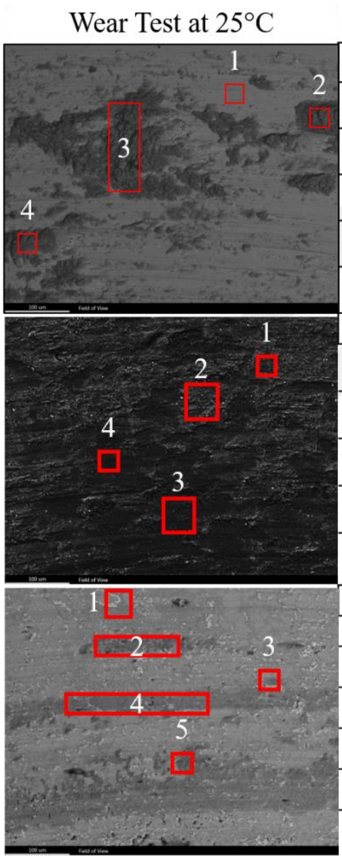

BARE INCONEL 718							
Point	Ni	Cr	Fe	Nb	Mo	Ti	O
1	46,13	18,46	16,05	2,14	1,23	1,24	14,74
2	22,35	9,02	7,89	1,04	0,52	0,58	58,61
3	21,89	8,94	7,74	1,11	0,62	0,55	59,15
4	19,43	7,87	6,85	0,94	0,49	0,45	63,97

HDA									
Point	Ni	Al	Cr	Si	Fe	Nb	Mo	Ti	O
1	2,44	57,68	6,36	12,38	3,71	1,26	0,61	0,63	14,93
2	1,14	52,33	6,29	17,58	2,78	1,15	0,53	0,66	17,53
3	1,78	45,76	3,09	9,99	0,37	0,89	0,35	0,5	37,27
4	1,78	9,12	0,25	0,84	1,51	0,33	0,45	2,74	41,24

HDA+DA									
Point	Ni	Al	Cr	Si	Fe	Nb	Mo	Ti	O
1	21,25	71,18	1,62	2,26	2,03	0,1	0,14	0,12	1,31
2	8,74	39,38	2,76	4	2,33	0,13	0,16	0,15	42,34
3	20,55	71,86	0,33	1	0,92	0,57	0,07	0,4	4,31
4	11,63	45,04	1,16	1,61	1,34	0,07	0,06	0,08	39,01
5	9,84	40,06	1,61	2,94	1,76	0,18	0,12	0,14	43,34

Figure 6.23 : Wear track point energy dispersive x-ray spectroscopy analyses of Inconel 718 (BARE), hot-dip aluminized Inconel 718 (HDA) and hot-dip aluminized+diffusion annealed Inconel 718 (HDA+DA) tested at 25°C.

Optical microscope images of counter-face ball and stereo microscope image of worn surfaces were given in Figure 6.24. Darker regions are generally related to adhesion of materials that comes from worn surfaces. Darker regions were observed in bare Inconel 718 images which can possibly be associated that adhesive wear mechanism. Dark regions were lowest detected at HDA+DA samples. HDA samples had moderate dark regions.

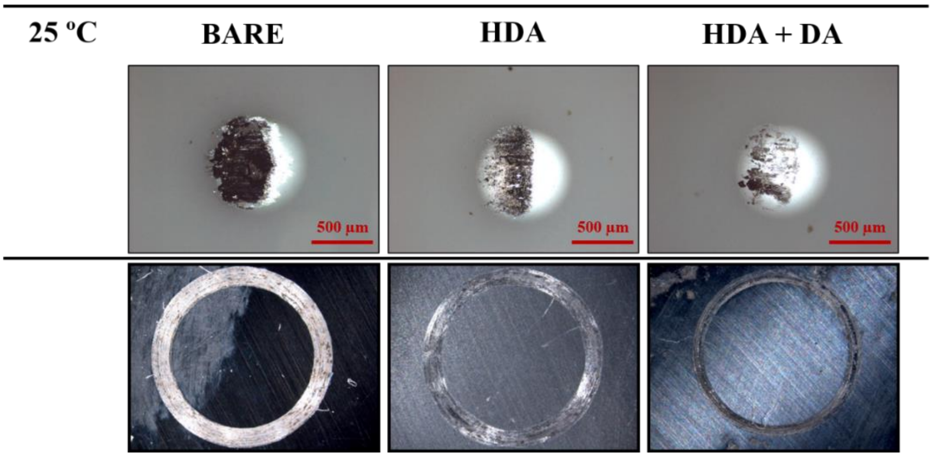

Figure 6.24 : Optical microscope images of counter-face ball and stereo microscope image of worn surfaces for 25°C wear tests.

6.3.3.2 Wear tests at 300°C

SEM images of wear tests at 300°C were given in Figure 6.25. According to top view images of wear tracks, tribo-chemical layer was obviously seen for bare Inconel 718. It was observed that areas of protrusive tribo-chemical layers were obviously increased for bare and HDA sample with the presence of intense oxide layer. It is important to noting that fish scale trace was detected that implies typical plastically tearing characteristic wear [90]. Oxide layer formation has influenced surface properties with deleterious intense plastic deformation. Large scale of delamination was detected for HDA samples with the presence of metal oxides on the top of surface. Plastically tearing vestiges and grooves were existed on the worn surface. HDA+DA samples wear images showed that worn surface has comparatively lower oxide scale and any other defects.

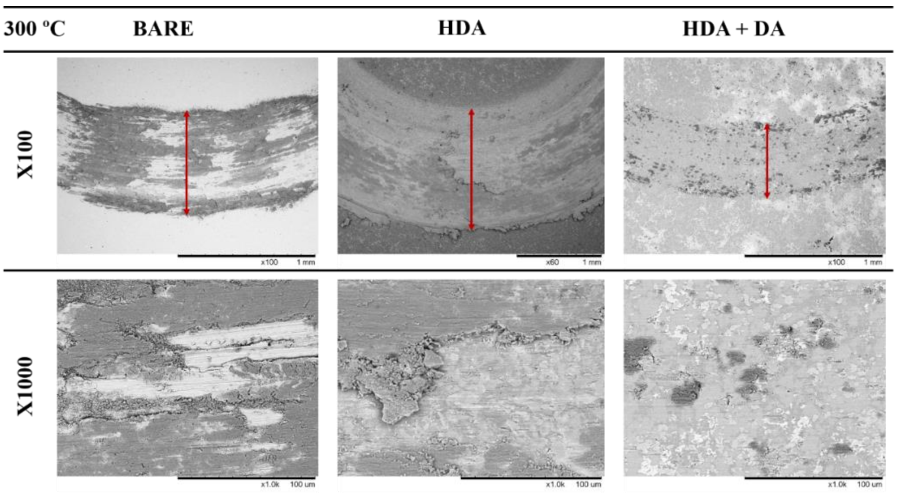

Figure 6.25 : SEM images of top view of wear track of samples tested at 300°C for bare sample , HDA sample and HDA+DA sample.

For wear tests at 300°C, cross-sectional SEM images of wear tracks were shown in Figure 6.26. In bare substrate images, it was observed that there is part chip in rupture stage in first frame. It was also observed that color contrast can be represented as mechanically mixed layer (MML) [91]. In second frame, ruptured parts can clearly be seen and be also seen zoomed image in sixth frame. Cracks and delaminated regions were detected where intense of tribo-chemical layer were increased. In fourth frame, it is obvious that delaminated flake has darker color due to form oxides.

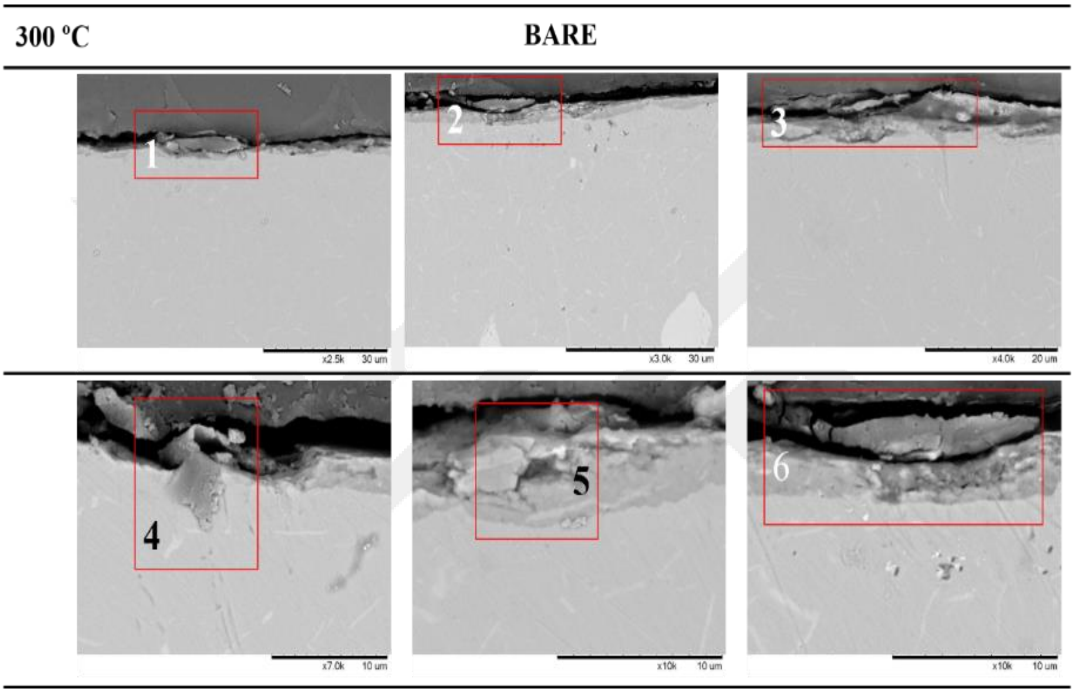

Figure 6.26 : Cross-sectional SEM images of worn surfaces of bare Inconel 718 sample tested at 300°C.

For HDA samples images tested at 300°C given in Figure 6.27, it was seen by low magnificated images and first frame that abrasive ball has sink more than half of coating thickness by smearing the material. High amount of peeling and plastically deformed region were detected in the worn surface. Also, thick and deleterious cracks can be distinguished. In second frame, ruptured region was observed while crack initiation was detected at third frame.

Wear track cross-sectional images of HDA+DA samples tested at 300°C were given in Figure 6.28, deep crack was observed in first frame. Intense delaminated regions were also detected.

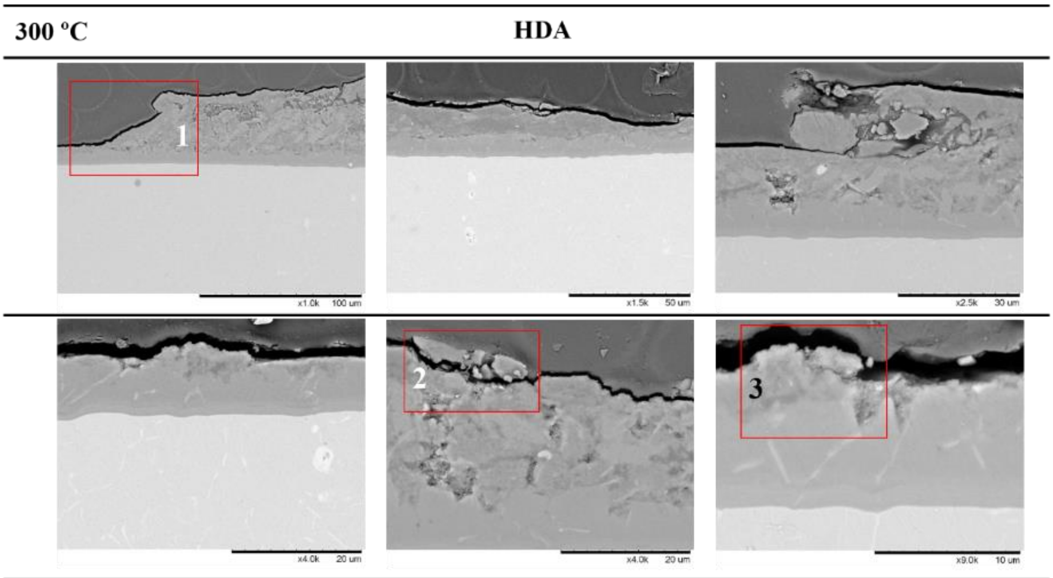

Figure 6.27 : Cross-sectional SEM images of worn surfaces of HDA sample tested at 300°C.

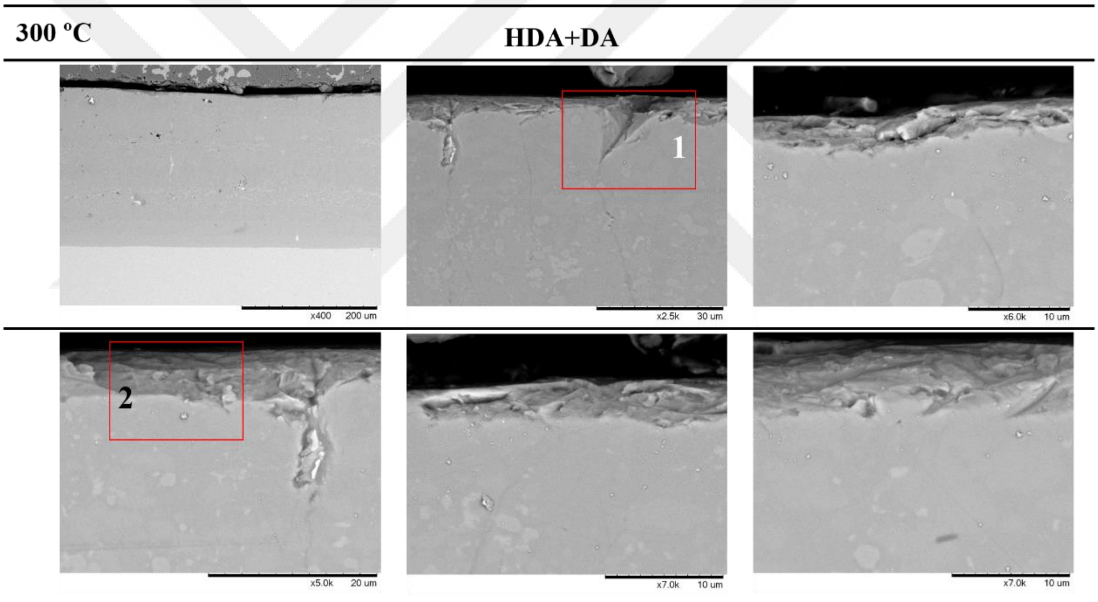

Figure 6.28 : Cross-sectional SEM images of worn surfaces of HDA sample tested at 300°C.

Point EDS analyses were done for samples that tested at 300°C temperature given in Figure 6.29. According to distribution of darker regions that indicates presence of oxides, local distribution was detected for bare substrate similar to tests at room temperature. For HDA sample, linear and continuous oxide scales were observed. For HDA+DA sample wear tracks EDS results, oxide scales were observed as tiny clustered compared to room temperature wear tests. Also, highest oxygen intensity was taken from results for HDA+DA sample. Additionally, it was resulted that effect of diffusion and higher temperature tests has increased amount of nickel on the surface.

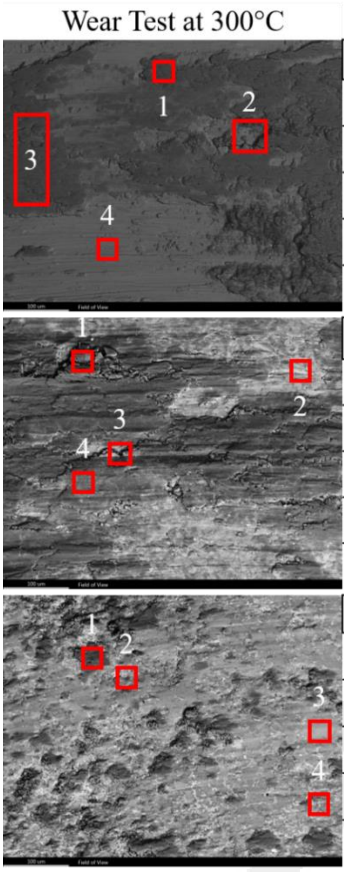

Intensity of elements (in at. %)

BARE INCONEL 718							
Point	Ni	Cr	Fe	Nb	Mo	Ti	O
1	28,6	11,6	10,05	1,45	0,74	0,77	46,79
2	34,08	13,81	12	1,56	0,83	1,02	36,68
3	28,92	11,75	10,14	1,5	0,8	0,82	46,07
4	50,43	20,08	17,41	2,57	1,4	1,31	6,8

HDA									
Point	Ni	Al	Cr	Si	Fe	Nb	Mo	Ti	O
1	1,08	40,46	3,65	11,2	0,29	0,93	0,41	0,43	41,55
2	4,1	59,56	6,97	17,07	2,1	1,58	0,68	0,69	7,25
3	1,56	55,34	7,18	13,38	2,29	1,19	0,59	0,65	17,82
4	1,35	44,56	4,14	11,64	0,35	1,02	0,48	0,58	35,88

HDA+DA									
Point	Ni	Al	Cr	Si	Fe	Nb	Mo	Ti	O
1	4,69	35,99	3,12	4,16	2,52	0,42	0,2	0,24	48,67
2	10,41	47,04	8,59	7,99	5,36	8,27	1,52	1,64	9,17
3	12,11	67,35	3,34	8,22	4,83	0,7	0,32	0,31	2,83
4	6,77	63,18	5,42	7,22	4,48	1	0,43	0,46	11,04

Figure 6.29 : Wear track point energy dispersive x-ray spectroscopy analyses of bare Inconel 718 (BARE), hot-dip aluminized Inconel 718 (HDA) and hot-dip aluminized+diffusion annealed Inconel 718 (HDA+DA) tested at 300°C.

Optical microscope images of counter-face ball and stereo microscope image of worn surfaces were given in Figure 6.30. According to images, ball surface of tested for bare Inconel 718 were seen as darker as coated and annealed samples.

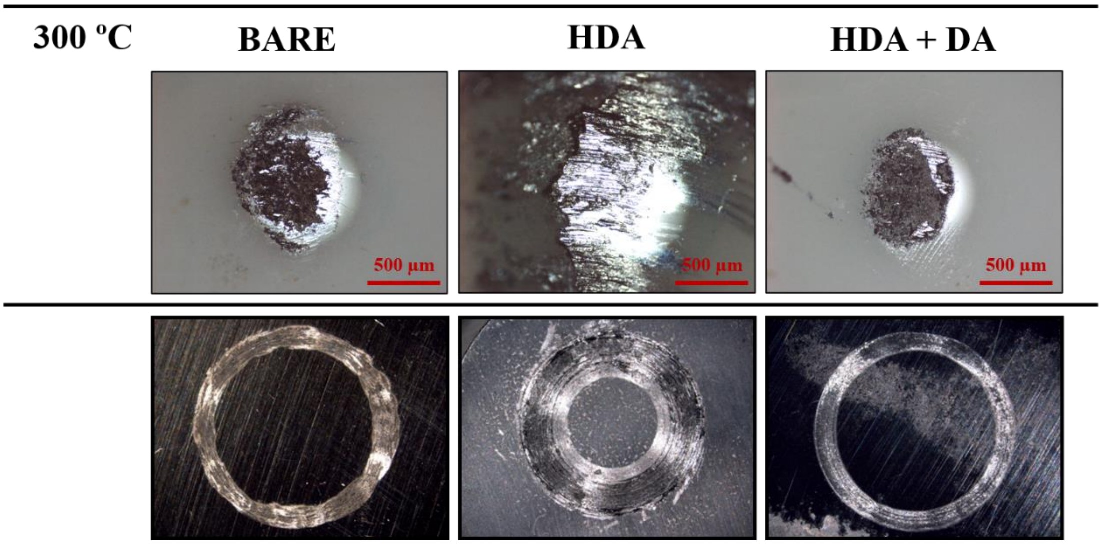

Figure 6.30 : Optical microscope images of counter-face ball and stereo microscope image of worn surfaces for 300°C wear tests.

6.3.3.3 Wear tests at 600°C

Bare Inconel 718 and HDA+DA SEM images of wear tests at 600°C were given in Figure 6.31. For the top view of wear tracks, rough and large oxide scale of bare substrate is observed that leads to delamination with plastic deformation. Dominant wear mechanism was detected as oxidative for bare Inconel 718. There can be seen particles that peeled off in HDA+DA with the low intense of grooves. The mechanism of abrasive wear draws attention with presence of micro-grooves. Nevertheless it can be inferred that diffusion annealing becomes a necessary process after coating.

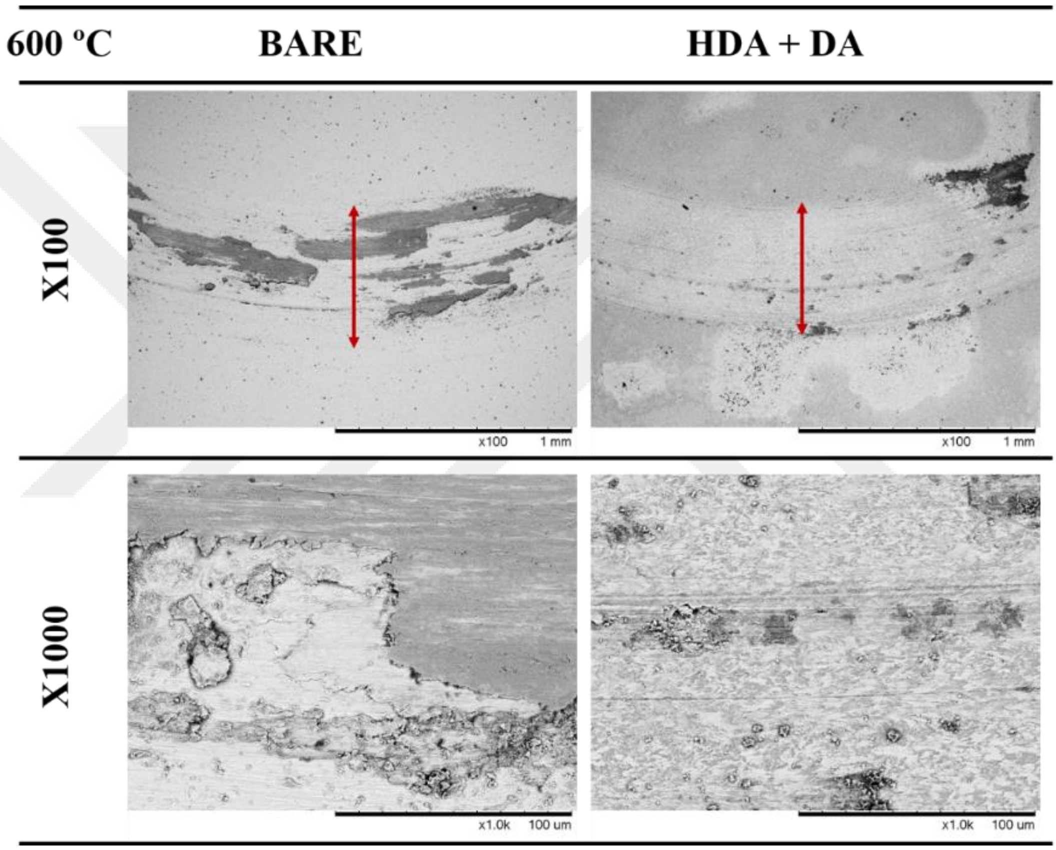

Figure 6.31 : SEM images of top view of wear track of samples tested at 600°C for bare sample and HDA+DA sample.

For wear tests at 600°C, cross-sectional SEM images of wear tracks of bare Inconel 718 were shown in Figure 6.32. In bare Inconel wear tests images, although second and third frame show crack initiation of materials from substrate, peeled of chip can be observed in first frame. Compared to low temperature wear tests, relatively continuous and smooth oxide layer were detected that supported by top image of worn surface. This tribo-chemical layer can be seen in fourth frame.

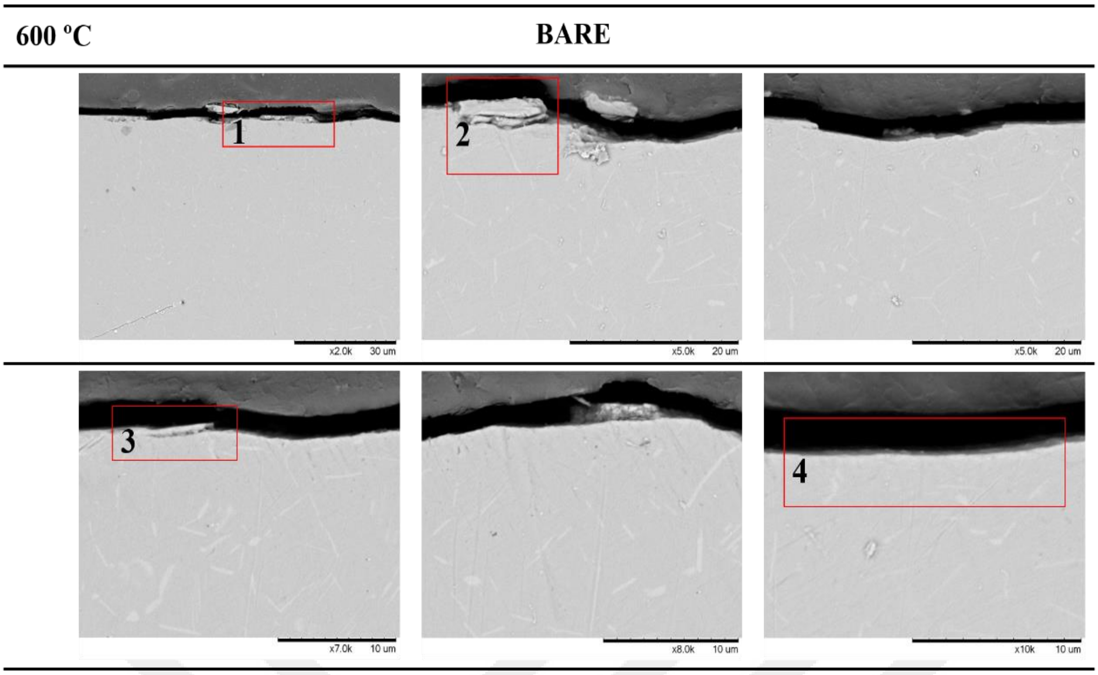

Figure 6.32 : Cross-sectional SEM images of worn surfaces of bare Inconel 718 sample tested at 600°C.

For wear tests at 600°C, cross-sectional SEM images of wear tracks of HDA+DA were shown in Figure 6.33. Peeled off particles can be seen in first and second frames. In first image, it was observed that wear depth was low. Delaminated region was detected which can possibly be affected by steps of crack formation such as initiation and propagation in third frame.

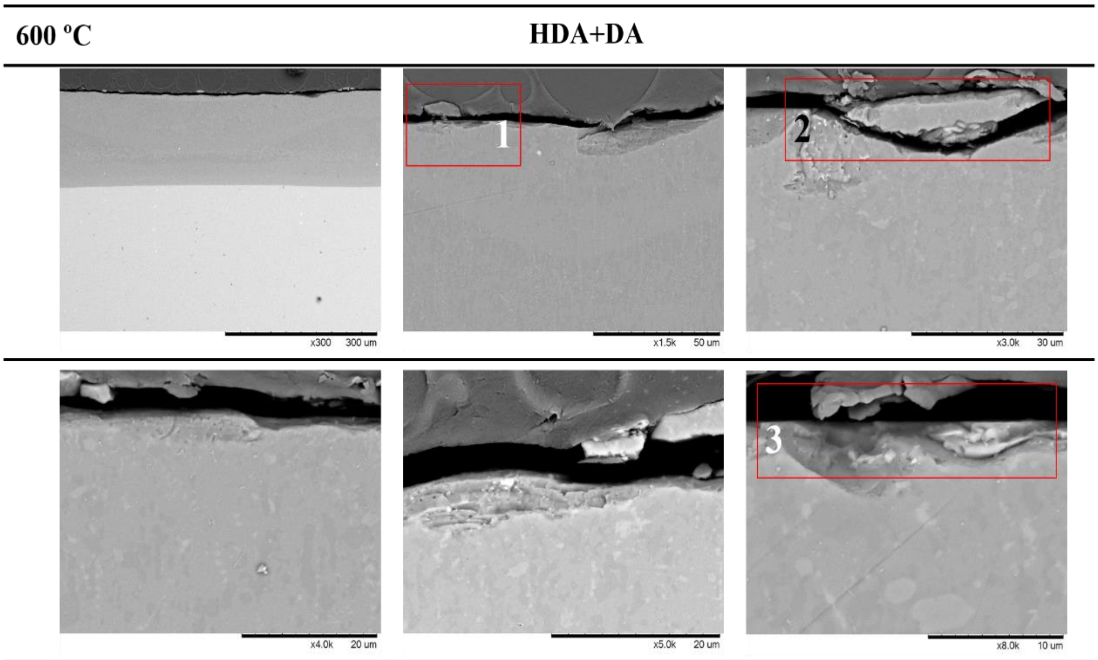

Figure 6.33 : Cross-sectional SEM images of worn surfaces of HDA+DA samples tested at 600°C.

Point EDS analyses were done for samples that tested at 600°C temperature given in Figure 6.34. For bare substrate, oxides were found linear. Compared to room temperature and 300°C wear tests, as expected, wide distribution of oxide scales was observed due to increasing of oxygen affinity of chromium. For HDA+DA sample, higher intensity of oxygen was detected in the darker regions. Also, in the third point of HDA+DA sample, higher silicon intensity was taken in from eds results due to high temperature wear test has been increasing diffusion of silicon on the surface.

Wear Test at 600°C

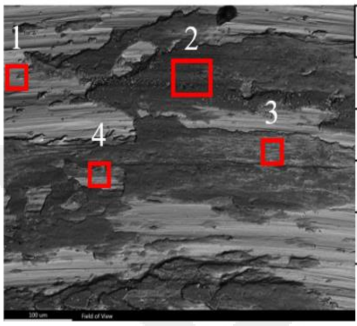

Intensity of elements (in at. %)

BARE INCONEL 718							
Point	Ni	Cr	Fe	Nb	Mo	Ti	O
1	46,97	19,02	16,6	2,18	1,31	1,2	12,72
2	24,16	9,72	8,91	1,3	0,7	0,61	54,59
3	31,53	13	10,54	1,66	0,92	1,12	41,24
4	46,97	18,93	16,35	2,35	1,32	1,23	12,85

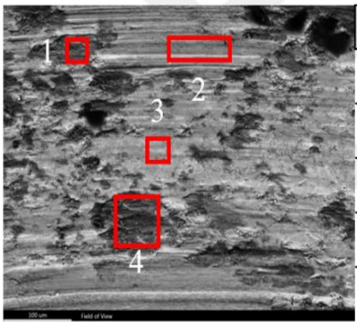

HDA+DA									
Point	Ni	Al	Cr	Si	Fe	Nb	Mo	Ti	O
1	7,14	37,45	5,83	7,45	2,2	0,51	0,35	0,43	38,63
2	13,75	61,22	4,46	8,62	3,1	0,61	0,36	0,3	7,58
3	4,21	29,51	15,46	29,95	0,37	2,38	1,26	1,4	15,46
4	3,52	27,42	7,15	11,33	0,91	1,14	0,52	0,79	47,2

Figure 6.34 : Wear track point energy dispersive x-ray spectroscopy analyses of bare Inconel 718 (BARE), hot-dip aluminized Inconel 718 (HDA) and hot-dip aluminized+diffusion annealed Inconel 718 (HDA+DA) tested at 600°C.

Optical microscope images of counter-face ball and stereo microscope image of worn surfaces were given in Figure 6.35. According to optical microscope images taken from alumina ball that is used for wear tests analyzing, adhesive wear mechanism was qualitatively observed for HDA+DA samples due to darker regions appearance. When samples exposed to higher temperature during wear tests, adhesive wear mechanism can easily be seen from images of alumina ball for HDA+DA sample. But for bare sample, majority of lighter regions was observed which means adhesive wear mechanism was not dominant for this sample.

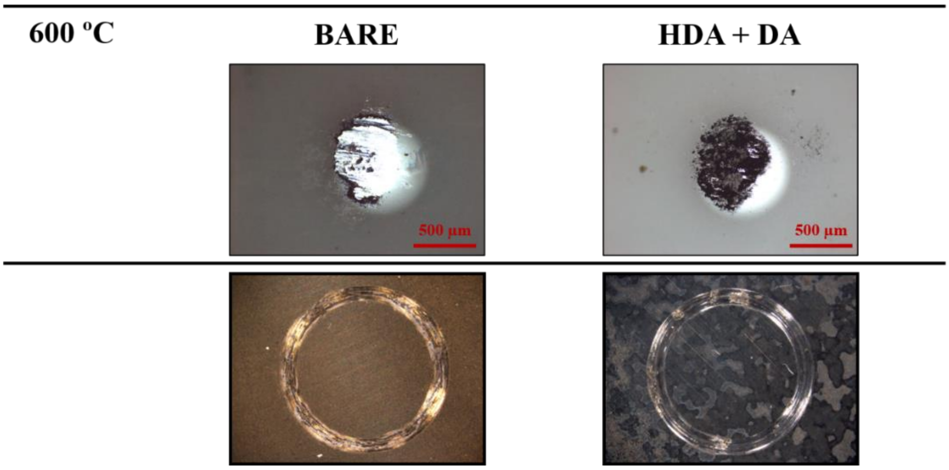

Figure 6.35 : Optical microscope images of counter-face ball and stereo microscope image of worn surfaces for 25°C wear tests.

6.4 Oxıdatıon Tests Results

Isothermal oxidation tests were carried out at 800°C for 100 and 300 hours in steam and carbon dioxide atmosphere for each sample.

6.4.1 Oxidation of bare inconel 718

Cross-sectional scanning electron microscope images of 100 and 300 hours oxidized bare Inconel 718 were given in Figure 6.36. It was observed that oxide layer was composed of $NiCr_2O_4$ and Cr_2O_3 that is compatible with the previous studies [35]. The oxides at the surface were porous, contains some cracks and were not continuous.

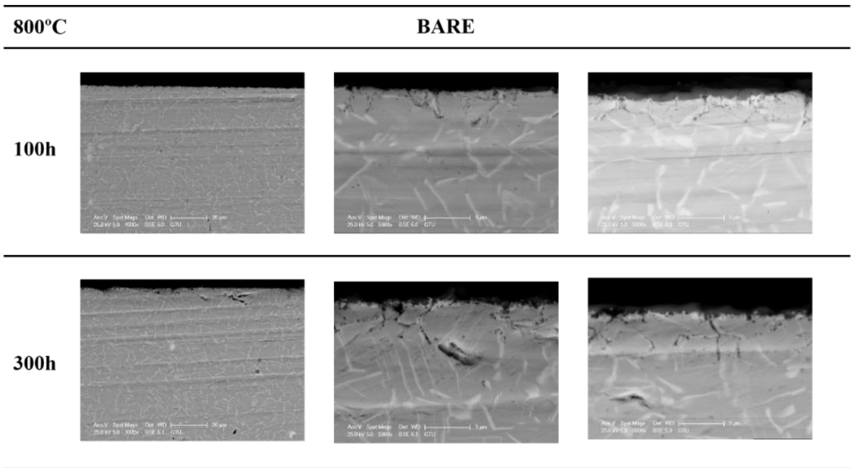

Figure 6.36 : Cross-sectional SEM images of 100 and 300 hours oxidized for bare Inconel 718.

X-Ray diffraction patterns of bare, 100 hours and 300 hours oxidized Inconel 718 were given in Figure 6.37. Results revealed that Ni, Cr, Fe and Nb elements in composition of Inconel 718 has tendency to form oxides. Oxide scales consist of $NiCr_2O_4$, Cr_2O_3 and $Cr_{1.3}Fe_{0.7}O_3$. It is possible to associate that decrease of intensity of characteristic peaks that were existed in 100h oxidized sample is due to increase of surface roughness.

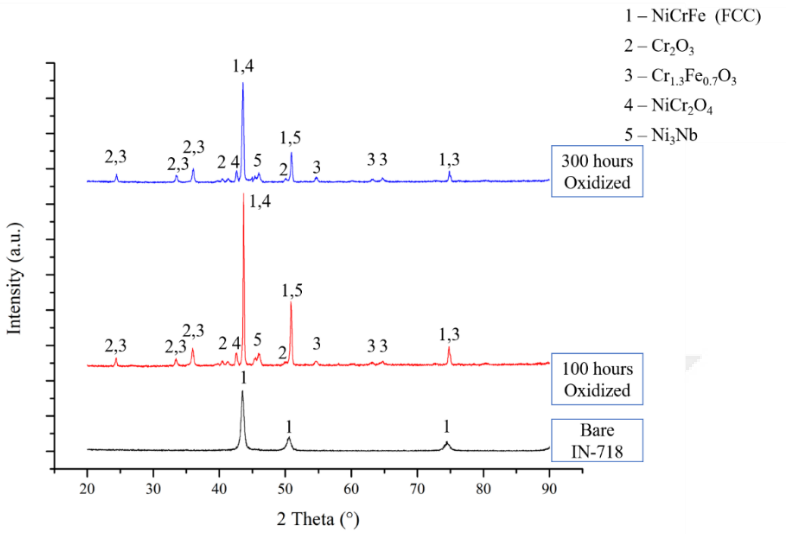

Figure 6.37 : X-Ray diffraction pattern of 100 and 300 hours oxidized bare Inconel 718.

Surface roughness were measured for oxidized bare Inconel 718 as given in Figure 6.38. It is seen that surface roughness (Ra) increases with increasing oxidation time. Quantitatively, it was detected that mean surface roughness of 300 hours oxidation test for bare Inconel 718 is at least two times higher than that of 100 hours oxidation test.

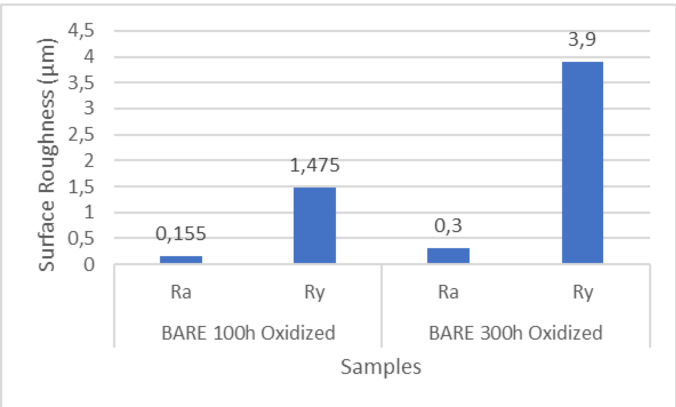

Figure 6.38 : Surface rougness values of 100 and 300 hours oxidized bare Inconel 718.

According to oxidized bare Inconel 718 Rockwell adhesion test SEM images given in Figure 6.39, both 100 and 300 hour oxidized sample can be categorized as HF-2 which is acceptable failure due to low number of micro-cracks.

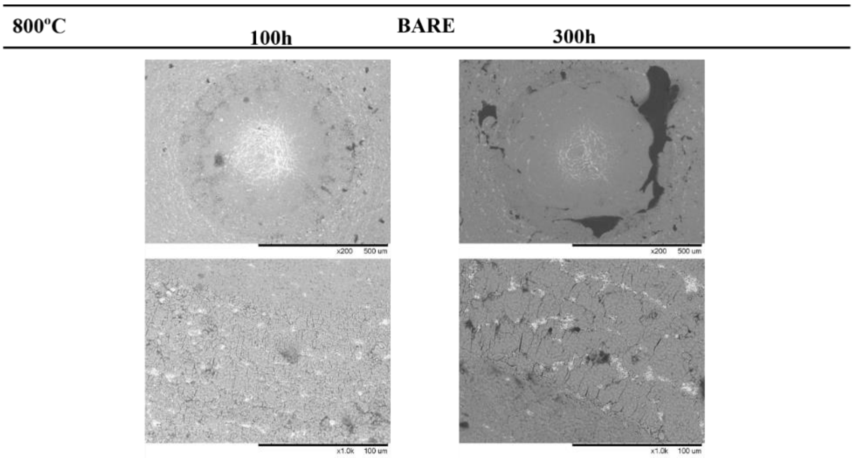

Figure 6.39 : 100 and 300 hours oxidized bare Inconel 718 samples Rockwell adhesion test SEM images.

6.4.2 Oxidation of hot-dip aluminized samples

Scanning electron microscope images were given in Figure 6.40 for bare Inconel 718 that oxidized at 800°C for 100 and 300 hours. According to images, it was expected that thickness of coating will be increased by heat input of oxidation test. It was detected that total thickness of coating increased approximately three times more than only-coated sample thickness. The oxide scale formed on the surface has a porous structure. Also, discontinuous and fluctuated scale formation were observed. After 300 hours oxidation tests, although total thickness coating layer is 135-145 µm, thickness of coating was measured as 165-175 µm for 100 hours test. It was observed oxygen diffusion led to formation of porous microstructure approximately 30µm toward surface. Simply, decrease of thickness coating could possibly be associated that as the oxidation time increases material loss from surface increases as breakaway of layers.

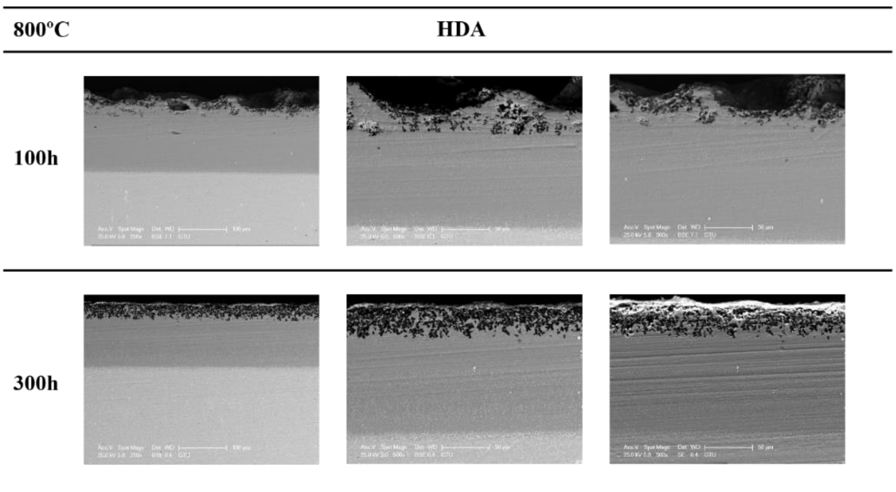

Figure 6.40 : Cross-sectional SEM images of 100 and 300 hours oxidized at 800°C for HDA sample.

According to fluctuated oxide layers, it can possibly be inferred that spallation occurred in some area. Cavities in outer layer could be affected by Ni and Al diffusion characteristics. Nevertheless, there are no cavities formed by Kirkendall effect in the middle layer of coating. Al rich regions in outer layer tend to cause scale debonding [34]. As the oxidation time increases, intensity of cavities and porosities increased. It is significant to indicate that selective oxidation was seen for 100 hours oxidation of HDA samples although homogeneous distribution of oxidated region was detected for 300 hours oxidation.

EDS analyses of HDA samples that were oxidized at 800°C for 100 hours were given in Figure 6.41. Low content of aluminum zones tends to increase chromium solubility that causes cavities. Local delamination in oxide scales takes places when chromium form cavities, but, it should be necessarily noted that chromia nuclei leads to nucleation of corundum alumina [92]. In second area, cavities could be related to low content of aluminum and high content of chromium. In first area, low content of nickel has possibility to supports breakaway of oxide scale.

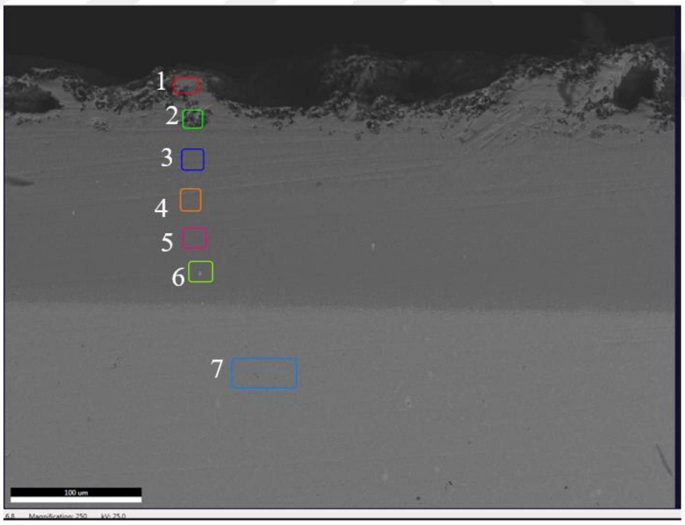

Chemical Composition (in at. %)

	Al	Ni	Cr	Si	Fe	Nb	Mo	Ti	O
1	55,11	25,68	1,53	2,32	3,84	0,14	0,16	0,08	11,14
2	35,13	9,12	7,67	7,42	4,01	0,88	0,39	0,48	34,91
3	50,92	27,18	5,03	5,59	8,18	0,63	0,31	0,37	1,78
4	45,01	23,8	10,04	7,97	7,89	1,29	0,64	0,69	2,67
5	47,25	22,51	11,45	5,14	7,5	1,23	0,64	0,47	3,81
6	53,34	24,1	6,9	0,49	8,54	3,09	0,66	0,6	2,28
7	1,4	49,83	20,14	0,22	17,68	2,68	1,35	1,31	5,39

Figure 6.41 : Point EDS results of 100 hours oxidized HDA samples.

EDS analyses of HDA samples that were oxidized at 800°C for 300 hours were given in Figure 6.42. In first and second area, oxygen contents were high due to oxide scale formation of chromia, alumina and silica. In middle layer, high amount of nickel in third, fourth and fifth area represents proper outward diffusion of nickel carried out without leading to Kirkendall porosities. Silicon elements tend to diffuse outer layer due to oxygen affinity. Additionally, higher content of silicon and chromium in location 1 could have capability to stabilize oxygen penetration and homogeneous homogenous distribution.

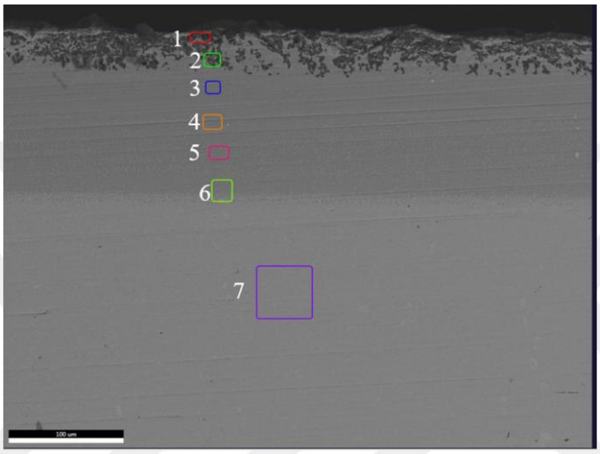

Chemical Composition (in at. %)

	Al	Ni	Cr	Si	Fe	Nb	Mo	Ti	O
1	26,49	3,81	5,09	8,32	3,12	1,74	0,64	0,67	50,13
2	33,75	4,19	5,49	6,24	2,94	0,72	0,43	0,35	45,9
3	46,13	29,73	6,15	5,52	9,68	0,48	0,29	0,47	1,55
4	38,64	25,67	12,13	7,6	9,41	1,65	0,78	1	3,12
5	47,15	28,44	6,23	2,35	10,92	1,35	0,73	0,38	2,46
6	42,03	39,49	8,05	0,11	5,34	1,35	0,59	0,58	2,48
7	1,43	50,88	20,27	0,17	17,43	2,71	1,47	1,46	4,19

Figure 6.42 : Point EDS results of 100 hours oxidized HDA sample.

Between second and third area there are high nickel content change draws attention. Highest aluminum content was show up in second area and highest nickel content were detected in third area in coating.

XRD patterns of HDA samples that oxidized at 800°C for 100 and 300 hours were given in Figure 6.43. According to oxide peaks, longer oxidation duration has increased oxide formation of aluminum, chromium and silicon that can be associated with EDS results. Presence of Ni-Al phases were mostly appeared in form of Ni_2Al_3. As the oxidation time increases, it was also detected that intensity of Ni-Al phases increased.

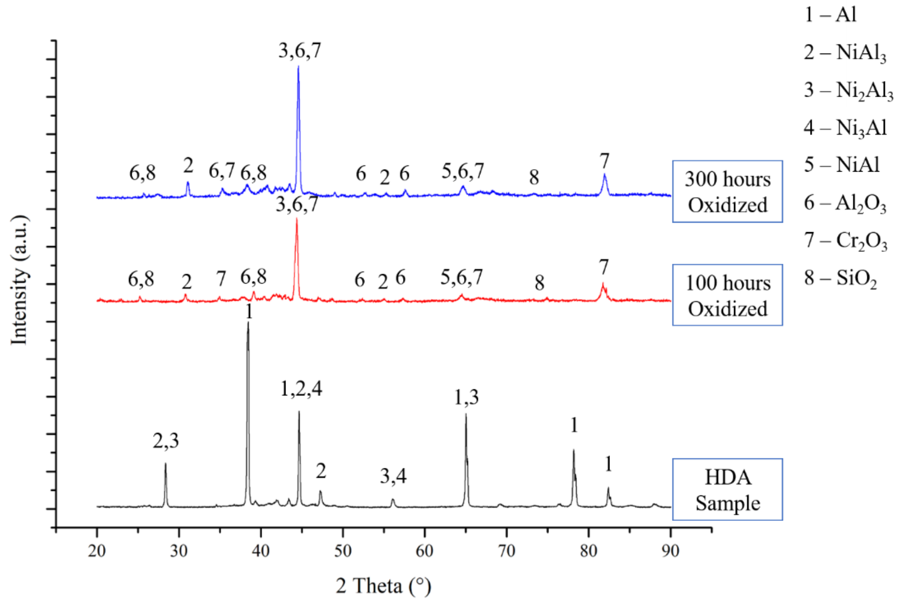

Figure 6.43 : X-Ray diffraction pattern of 100 and 300 hours oxidized HDA Inconel 718.

Surface roughness were measured for oxidized hot-dip aluminized samples as given in Figure 6.44. As the oxidation time increases surface roughness parameters (Ra and Ry) increase. Maximum roughness were obtained for oxidized HDA samples with respect to the other oxidized samples.

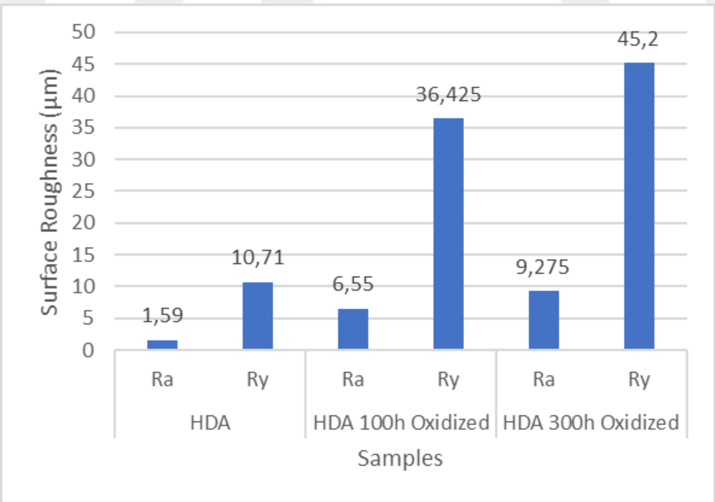

Figure 6.44 : Surface rougness values of 100 and 300 hours oxidized HDA Inconel 718.

According to oxidized bare Inconel 718 Rockwell adhesion test SEM images given in Figure 6.45, 100 hour oxidized sample can be categorized as HF-3 which is acceptable failure due to low content of micro-cracks and moderate content of delaminated sites. 300 hours oxidized sample can be categorized as HF-4 due to high content of micro-cracks and high content of delamination.

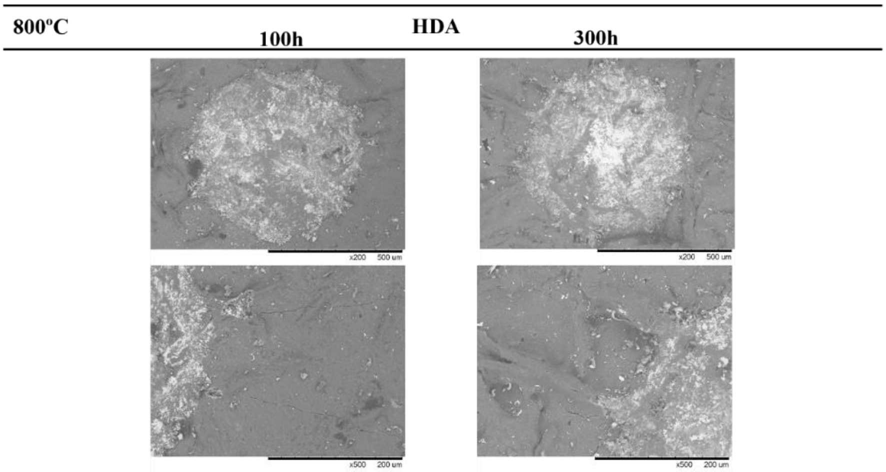

Figure 6.45 : 100 and 300 hours oxidized HDA Inconel 718 samples Rockwell adhesion test SEM images.

6.4.3 Oxidation of hot-dip aluminized and diffusion annealed samples

SEM micrographs of HDA+DA samples that were oxidized at 800°C for 100 and 300 hours were given in Figure 6.46 with different magnification. Coating thickness of 100 and 300 oxidized samples were approximately measured as 310 μm and 270 μm relatively. There can be seen oxidized area beneath outer layer due to diffusion of oxygen atoms toward surface. In 100 hours oxidation images, it was detected that cavities were existed in upper parts of coating at least 100 μm. Besides, it was also observed that cavities were existed along 60 μm in upper parts of coating for 300 hours oxidated samples. Nevertheless, unbroken durable region can be seen among cavities.

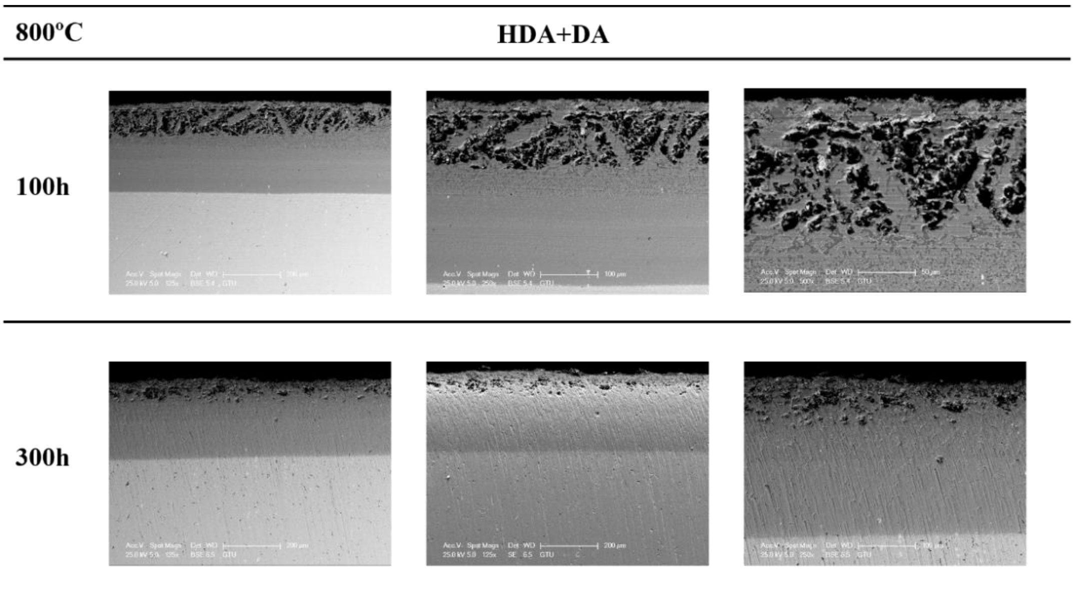

Figure 6.46 : Cross-sectional SEM images of 100 and 300 hours oxidized for bare Inconel 718.

EDS analyses of HDA+DA samples that were oxidized at 800°C for 100 hours were given in Figure 6.47. It was clear that outer layer mostly consists of Al, Cr and Si for hot-dip aluminized and diffusion annealed sample. According to outer layer point EDS analysis, intensities of these elements were seen similar. High amount of Nb content in first area draws attention that can be attributed to preference to form oxides for Nb. High oxygen content was found in second area that contains porosities and cavities and lower Cr content were detected compared to first area.

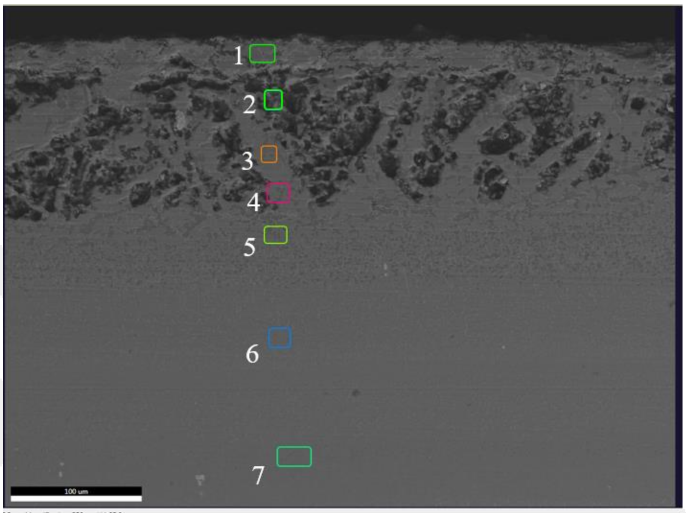

Chemical Composition (in at. %)

	Al	Ni	Cr	Si	Fe	Nb	Mo	Ti	O
1	19,62	0,44	22,46	40,76	0,51	3,57	2,55	1,71	8,37
2	40,51	5,66	4,34	6,05	4,62	0,59	0,13	0,28	37,82
3	58,55	30,81	1,75	3,75	3,01	0,23	0,04	0,18	1,68
4	56,82	24,81	3,57	6,71	5,1	0,49	0,2	0,27	2,03
5	53,07	20,69	6,53	9,06	6,75	0,83	0,43	0,38	2,26
6	46,83	23,05	7,94	10,64	6,82	1	0,84	0,57	2,31
7	52,37	28,23	4,31	5	7,18	0,46	0,27	0,41	1,77

Figure 6.47 : Point EDS results of 100 hours oxidized HDA+DA samples.

Nevertheless, there can be seen no-degraded regions among cavities that stands out with specifical durable structure. When the areas were checked with EDS analysis of these regions, it was observed that high content of Ni has played important role to prevent crack initiation or cavities with the presence of aluminum.

EDS mapping images of view was shown in Figure 6.48. Aluminum elements were homogenously distributed in the middle area of coating. Additionally, Al elements were detected in upper outer layer. Nickel distribution were also seen among all middle layers. Accordance between nickel and aluminum elements led to prevent crack or formation of cavities due to increase of aluminum solubility in nickel tend to decrease chromium content in these regions. Chromium contents in surface draws attention to former of oxide scale as well as silicon. Although silicon has preferentially diffused into outer layer of coating surface, chromium has showed up in whole coating structure in addition to presence in outer layer. Diffusion of iron elements were limited during oxidation. Niobium and molybdenum elements were seen in outer layer with the capability to form oxides $CrNbO_4$ and $MoCrO_3$. Oxygen elements were observed near to delaminated regions that are beneath outer layer.

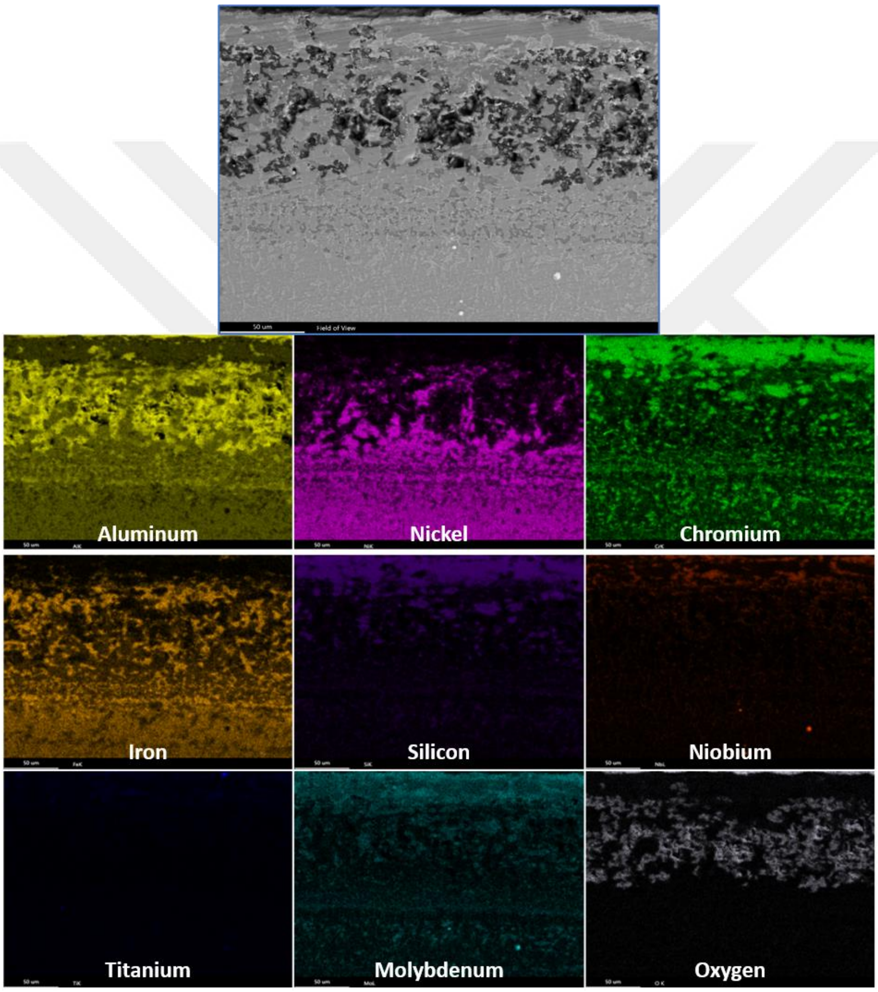

Figure 6.48 : Mapping EDS results of 100 hours oxidized HDA+DA samples.

Colored elemental distribution of mapping EDS results of 100 hours oxidized HDA+DA sample were given in Figure 6.49. Outer layer mostly consists of Si, Cr, Al and Mo with yellow color. It is clearly seen that upper middle layer is composed of green and red. Red colored region contains Al, Cr, Si, Fe and O elements. In addition to red colored region, green color extra contains Ni. It was detected that bottom of middle layer consists of blue that contains Al, Ni, Cr and Fe elements.

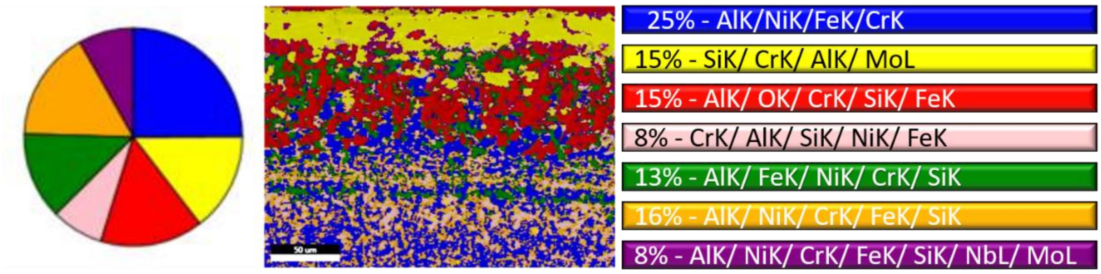

Figure 6.49 : Colored elemental distribution of mapping EDS results of 100 hours oxidized HDA+DA sample.

Distribution of elements mapping EDS results of 100 hours oxidized HDA+DA sample were given in Figure 6.50. It was observed that chromium tends to arrive surface owing to diffusion. Aluminum was not only found in the outer layer to form protective oxide layer, but also it was existed in the middle layer. Major content of silicon was seen in the outer layer colored dark blue region. It can be seen that niobium was preferentially diffused to beneath outer layer.

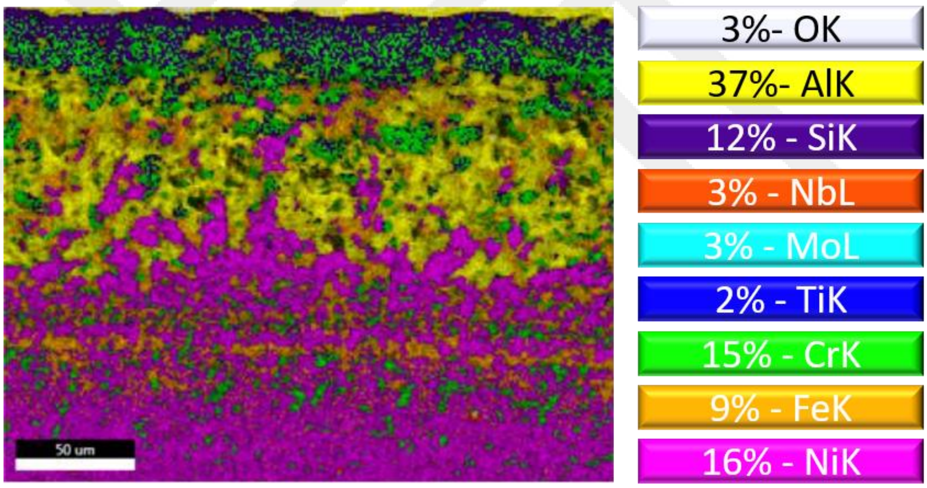

Figure 6.50 : Distribution of elements mapping EDS results of 100 hours oxidized HDA+DA.

EDS analyses of HDA+DA samples that were oxidized at 800°C for 300 hours were given in Figure 6.51. Aluminum content were between 25-40% in the areas. For first area, oxide intensity was found to be high with the form of alumina, chromia and silica. Gradually decreasing content of nickel from substrate to outer layer triggered decrease of aluminum solubility of aluminum. There is inevitable fact that aluminum poor areas occurs when chromium content is increased in the outer layer that forms cavities. Silicon preferentially tends to diffuse outer layer as the oxidation time increases. In location 4, high content of niobium stands out with the form of cluster.

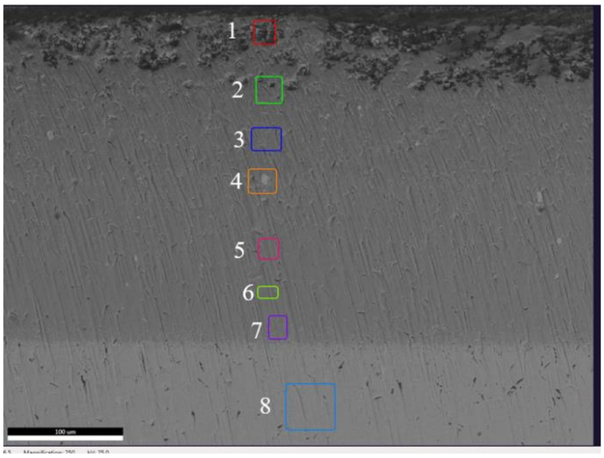

Chemical Composition (in at. %)

	Al	Ni	Cr	Si	Fe	Nb	Mo	Ti	O
1	26,82	3,52	7,98	11,94	1,64	1,21	0,61	0,5	45,79
2	42,8	23,32	7,81	13,19	8	0,79	0,58	0,36	3,17
3	42,03	23,09	8,8	13,53	7,6	1,21	0,64	0,54	2,55
4	39,87	22,79	7,64	9,59	7,23	6,72	0,56	1,51	4,08
5	49,44	22,86	10,28	4,12	7,57	1,23	0,64	0,48	3,37
6	54,35	23,33	8,83	0,27	8,06	1,25	0,64	0,47	2,79
7	52,29	28,83	6,62	0,51	8,18	0,81	0,48	0,27	2,02
8	1,26	50,42	20,34	0,26	17,75	2,5	1,36	1,25	4,85

Figure 6.51 : Point EDS results of 300 hours oxidized HDA+DA sample.

XRD patterns of HDA sample and HDA samples that oxidized at 800°C for 100 and 300 hours were given in Figure 6.52. It is detected that alumina peaks started to disappear as the oxidation time increases. It is also detected that intensity of the SiO_2 and Al_2O_3 peaks decreased as the oxidation duration increases. For 300 hours oxidation, increase of Ni_2Al_3 peaks was minimally observed compared to 100 hours.

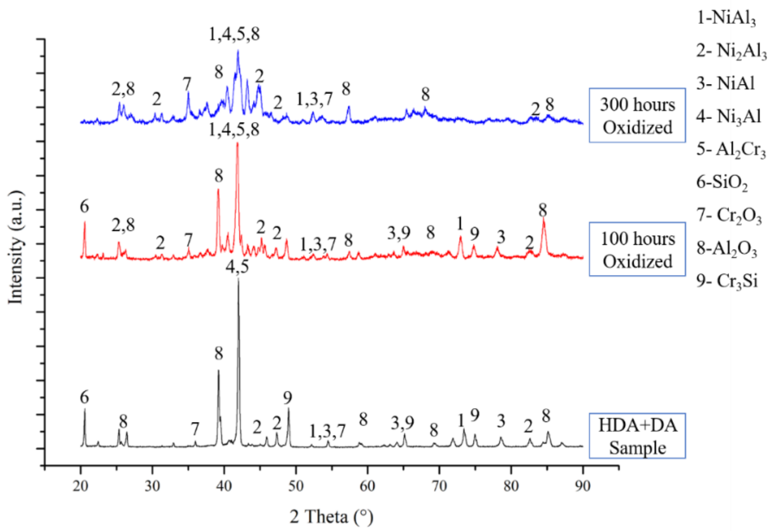

Figure 6.52 : X-Ray diffraction pattern of 100 and 300 hours oxidized HDA+DA Inconel 718.

Surface roughness was measured for oxidized hot-dip aluminized and samples as given in Figure 6.53. As the oxidation time increases, surface roughness (Ra and Ry) increases. Increase in surface roughness were not as much as oxidized HDA sample.

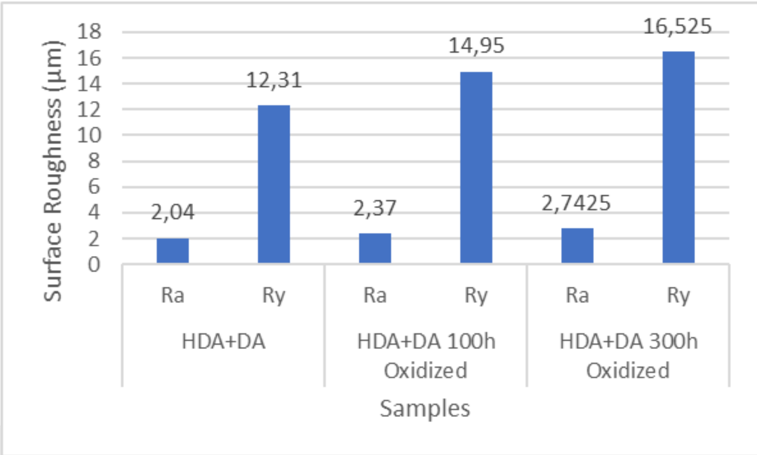

Figure 6.53 : Surface rougness values of 100 and 300 hours oxidized HDA+DA Inconel 718 sample.

SEM images of HDA+DA samples that are subjected to Rockwell adhesion test were given in Figure 6.54. According to Rockwell adhesion test 100 hours oxidized HDA+DA samples images taken from SEM could be categorized in HF-5 due to deep cracks and delamination showed up inside of hole. For 300 hours oxidized HDA+DA sample images, it can be also referred as HF-4 type similar with 100 hours oxidized HDA+DA sample.

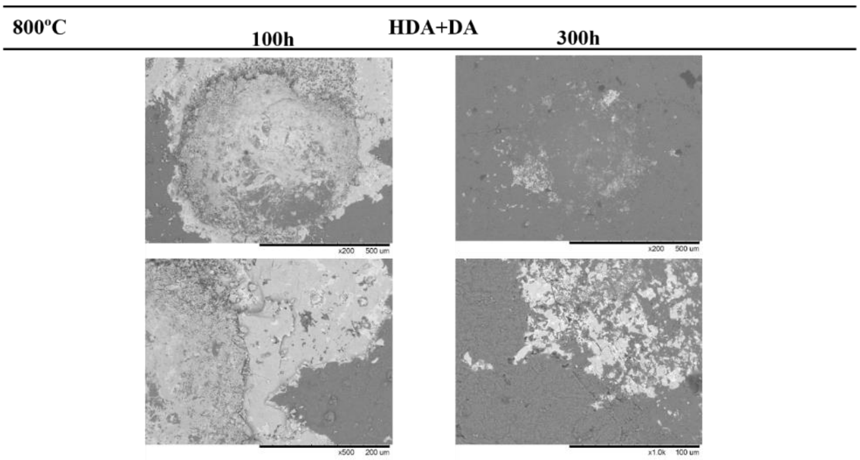

Figure 6.54 : 100 and 300 hours oxidized HDA Inconel 718 samples Rockwell adhesion test SEM images.

7. CONCLUSION

Inconel 718 superalloy was aluminized by the hot-dip process at 700°C for 2 minutes and air cooled to room temperature. Following aluminizing, samples were diffusion annealed at 700°C for 10 hours. Ball on disc wear test were done at 25°C, 300°C and 600°C and isothermal oxidation tests were carried out at 800°C for 100 and 300 hours in steam and carbon dioxide atmosphere for bare Inconel 718 samples (BARE), hot-dip aluminized samples (HDA) and hot-dip aluminized plus diffusion annealed samples (HDA+DA). Results coming from quantitative and qualitative analyses has revealed that:

Hot-dip aluminizing process were successfully applied to Inconel 718 superalloy. Non-porous middle layer, smooth outer layer and inter-diffusion zone were obtained. Elemental distribution showed that inward diffusion of Al and outward diffusion of Ni taken place with the presence of $NiAl_3$ and Ni_2Al_3. XRD results were detected to be compatible with EDS analyses. Diffusion annealing process were applied as a part of HDA. Eventually, not only higher hardness values for wear resistance were obtained, but also presence of Ni-Al phases for oxidation resistance were structurally detected.

Wear tests at room temperature showed that the wear rate of the HDA+DA was approximately found to be three times less than the HDA and four times less than bare Inconel 718 as well as HDA samples wear rate were measured lower than bare Inconel 718. It is revealed that as the wear test temperature increases, wear rate of bare Inconel 718 decreases up to five-fold. Although wear rate of HDA+DA samples were found to be increased for 300°C, lower wear rate was obtained by wear tests at 600°C. It was detected that applying diffusion annealing to HDA samples prominently led to reduce wear rate.

For room temperature wear tests, fluctuations in graph of friction coefficient were seen for bare Inconel 718 due to formation and deterioration of oxide. It can be associated with granular oxide patches formation. Lowest CoF value was detected for HDA sample. HDA+DA samples has showed moderate CoF compared to HDA and bare Inconel 718. Tests at 300°C showed that fluctuations were disappeared in bare Inconel

718 due to continuous and sustainable oxide formation by heat input. Wear tests at 600°C showed that decline of graph in the beginning can be related with oxide formation that led to lower friction coefficient for bare substrate. In general, as the wear temperature increases, it was detected that CoF of bare and HDA+DA Inconel 718 samples decreases except for HDA samples.

When the worn surfaces are examined with scanning electron microscopy, oxidative wear mechanisms were mostly found dominant in HDA and bare Inconel 718 samples. It was revealed that applying diffusion annealing process has capability to prevent the oxidative wear mechanism, for this reason abrasive wear mechanisms were generally seen in HDA+DA samples.

In the surface of oxidized bare Inconel 718, porous and partially cracked structure were seen that are composed of $NiCr_2O_4$, Cr_2O_3 and $Cr_{1.3}Fe_{0.7}O_3$ according to SEM and XRD analyses. High increase in surface roughness were detected between 100 and 300 hours testing for bare Inconel 718 compared to HDA and HDA+DA samples due to acicular morphology. It was also detected that optimal adhesion were obtained in oxidized bare Inconel 718 for both oxidation time by Rockwell-C test adhesion test.

When oxidized HDA sample coating surface were structurally examined it was observed that oxygen atoms have preferentially diffused beneath outer layer, then led to selective oxidation for 100 hours oxidation that caused to corrugated oxide structure. It was also observed that as the oxidation time increased, selective oxidation transformed to homogeneous oxidation with the increase of Ni-Al phases peaks coming from XRD results.

Although cavities were detected in the upper part of coating layer, HDA+DA sample outer layer showed durable structure against for 100 hours oxidation without breakaway. Decrease in total thickness was observed with the formation of oxidative breakaway after 100 hours oxidation. Nevertheless, HDA+DA samples showed relatively better oxidation performance by preventing penetration or diffusion of oxygen to substrate thanks to surface coating compared to bare and HDA Inconel 718.

REFERENCES

[1] **S. J. D. Matthew J. Donachie**, (2002). A Technical Guide, in *SUPERALLOYS*, 2nd Editio., 2002, pp. 1–4.

[2] **A. Kracke**, (2010). Superalloys, the most successful alloy system of modern times - Past, present and future, in *7th International Symposium on Superalloy 718 and Derivatives 2010*, vol. 1, pp. 13–50. doi: 10.1002/ 9781118495223.ch2.

[3] **L. Huang, X. F. Sun, H. R. Guan, and Z. Q. Hu**, (2006). Effect of rhenium addition on isothermal oxidation behavior of single-crystal Ni-based superalloy, *Surf. Coatings Technol.*, vol. 200, no. 24, pp. 6863–6870, doi: 10.1016/j.surfcoat.2005.10.037.

[4] **Y. M. Wang-Koh**, (2016). Materials Science and Technology Understanding the yield behaviour of L1 2-ordered alloys, doi:10.1080/02670836.2016. 1215961.

[5] **J. Belan**, (2016). GCP and TCP Phases Presented in Nickel-base Superalloys, in *Materials Today: Proceedings*, Jan. 2016, vol. 3, no. 4, pp. 936–941. doi: 10.1016/j.matpr.2016.03.024.

[6] **J. Wang and H. Sehitoglu**, (2014). Dislocation slip and twinning in Ni-based L12 type alloys, *Intermetallics*, vol. 52, pp. 20–31, doi: 10.1016/j.intermet. 2014.03.009.

[7] **Y. Nunomura, Y. Kaneno, H. Tsuda, and T. Takasugi**, (2004). Phase relation and microstructure in multi-phase intermetallic alloys based on Ni3Al-Ni3Ti-Ni3V pseudo-ternary alloy system, *Intermetallics*, vol. 12, no. 4, pp. 389–399, doi: 10.1016/j.intermet.2003.12.011.

[8] **A. S. Wilson**, (2017). Formation and effect of topologically close-packed phases in nickel-base superalloys, *Materials Science and Technology (United Kingdom)*, vol. 33, no. 9. Taylor and Francis Ltd., pp. 1108–1118, Jun. 13, 2017. doi: 10.1080/02670836.2016.1187335.

[9] **C. Rae, M. Karunaratne, C. Small, R. Broomfield, C. Jones, and R. Reed**, (2000). Topologically Close Packed Phases in An Experimental Rhenium-Containing Single Crystal Superalloy, in *Superalloys 2000 (Ninth International Symposium)*, 2000, pp. 767–776.

[10] **Url-1** < https://www.sciencedirect.com/topics/materials-science/adhesive-wear>, (accessed Aug. 10, 2021).

[11] **T. Hammerschmidt, B. Seiser, R. Drautz, and D. G. Pettifor**, (2008). Modeling topologically close-packed phases in superalloys: Valence-dependent bond-order potentials based on ab-initio calculations, *Proc. Int. Symp. Superalloys*, no. January, pp. 847–853, doi: 10.7449/2008/superalloys_ 2008_847_853.

[12] **M. Pohl, O. Storz, and T. Glogowski**, (2008). σ-phase morphologies and their effect on mechanical properties of duplex stainless steels, *Zeitschrift fuer Met. Res. Adv. Tech.*, vol. 99, no. 10, pp. 1163–1170, doi: 10.3139/146.101738.

[13] **X. Z. Qin, J. T. Guo, C. Yuan, G. X. Yang, L. Z. Zhou, and H. Q. Ye**, (2009). μ-Phase behavior in a cast Ni-base superalloy, *J. Mater. Sci.*, vol. 44, no. 18, pp. 4840–4847, doi: 10.1007/s10853-009-3738-7.

[14] **P. A. Carvalho, H. S. D. Haarsma, B. J. Kooi, P. M. Bronsveld, and J. T. M. De Hosson**, (2000). HRTEM study of Co7W6 and its typical defect structure, *Acta Mater.*, vol. 48, no. 10, pp. 2703–2712, doi: 10.1016/S1359-6454(00)00064-1.

[15] **X. Z. Qin, J. T. Guo, C. Yuan, G. X. Yang, L. Z. Zhou, and H. Q. Ye**, (2009). μ-Phase behavior in a cast Ni-base superalloy, *J. Mater. Sci.*, vol. 44, no. 18, pp. 4840–4847, doi: 10.1007/s10853-009-3738-7.

[16] **C. H. Radha, K. Shna, and K. P. Rao**, (1997). The formation and control of Laves phase in superalloy 718 welds.

[17] **J. Sato, T. Omori, K. Oikawa, I. Ohnuma, R. Kainuma, and K. Ishida**, (2006). Cobalt-base high-temperature alloys, *Science (80-.).*, vol. 312, no. 5770, pp. 90–91, doi: 10.1126/science.1121738.

[18] **A. Suzuki and T. M. Pollock**, (2008). High-temperature strength and deformation of γ/γ′ two-phase Co-Al-W-base alloys, *Acta Mater.*, vol. 56, no. 6, pp. 1288–1297, doi: 10.1016/j.actamat.2007.11.014.

[19] **C. Cui, D. Ping, Y. Gu, and H. Harada**, (2006). A new co-base superalloy strengthened by γ′ phase, *Mater. Trans.*, vol. 47, no. 8, pp. 2099–2102, doi: 10.2320/matertrans.47.2099.

[20] **C. T. Sims**, (1984). A HISTORY OF SUPERALLOY METALLURGY FOR SUPERALLOY METALLURGISTS. doi:10.7449/1984/Superalloys _ 1984_399_419.

[21] **C. Wang, Y. Wu, Y. A. Guo, J. Guo, and L. Zhou**, (2019). Precipitation behavior of sigma phase and its influence on mechanical properties of a Ni-Fe based alloy, *J. Alloys Compd.*, vol. 784, pp. 266–275, doi: 10.1016/j.jallcom.2019.01.048.

[22] **A. I. Epishin, N. V Petrushin, T. Link, G. Nolze, Y. V Loshchinin, and G. Gerstein**, (2015). Thermal Stability of the Structure of a Heat-Resistant Cobalt Alloy Hardened with Intermetallic γ'-Phase Precipitates, vol. 2016, no. 4, pp. 17–22, doi: 10.1134/S0036029516040078.

[23] **A. Thomas, M. El-Wahabi, J. M. Cabrera, and J. M. Prado**, (2006). High temperature deformation of Inconel 718, *J. Mater. Process. Technol.*, vol. 177, no. 1–3, pp. 469–472, doi: 10.1016/j.jmatprotec.2006.04.072.

[24] **J. Zhao, Z. Liu, B. Wang, Y. Hua, and Q. Wang**, (2018). Cutting temperature measurement using an improved two-color infrared thermometer in turning Inconel 718 with whisker-reinforced ceramic tools, *Ceram. Int.*, vol. 44, no. 15, pp. 19002–19007, doi: 10.1016/j.ceramint.2018.07.142.

[25] **K. A. Al-Hatab • *et al.***, (2011). Cyclic Oxidation Behavior of IN 718 Superalloy in Air at High Temperatures, *Oxid Met*, vol. 75, pp. 209–228, doi: 10.1007/s11085-010-9230-6.

[26] **J. R. Nicholls**, (2000). Designing oxidation-resistant coatings, *J. Miner. Met. Mater. Soc.*, vol. 52, no.1, pp. 28–35, doi:10.1007/s11837-000-0112-2.

[27] **R. C. Reed and C. M. F. Rae**, (2014). Physical Metallurgy of the Nickel-Based Superalloys, in *Physical Metallurgy: Fifth Edition*, vol. 1, Elsevier Inc., 2014, pp. 2215–2290. doi: 10.1016/B978-0-444-53770-6.00022-8.

[28] **M. Shourgeshty, M. Aliofkhazraei, and M. M. Alipour**, (2016). Introduction to High- Temperature Coatings, in *High Temperature Corrosion*, InTech, 2016. doi: 10.5772/64282.

[29] **R. Sitek, T. Bolek, R. Dobosz, T. Plocinski, and J. Mizera**, (2016). Microstructure and oxidation resistance of aluminide layer produced on Inconel 100 nickel alloy by CVD method, *Surf. Coatings Technol.*, vol. 304, pp. 584–591, doi: 10.1016/j.surfcoat.2016.07.072.

[30] **X. Gong, H. Peng, Y. Ma, H. Guo, and S. Gong**, (2016). Microstructure evolution of an EB-PVD NiAl coating and its underlying single crystal superalloy substrate, *J. Alloys Compd.*, vol. 672, pp. 36–44, doi: 10.1016/j.jallcom.2016.02.115.

[31] **C. Lyphout, P. Nylén, A. Manescu, and T. Pirling**, (2008). Residual stresses distribution through thick HVOF sprayed inconel 718 coatings, in *Journal of Thermal Spray Technology*, Nov. 2008, vol. 17, no. 5–6, pp. 915–923. doi: 10.1007/s11666-008-9242-9.

[32] **R. Singh, S. Schruefer, S. Wilson, J. Gibmeier, and R. Vassen**, (2018). Influence of coating thickness on residual stress and adhesion-strength of cold-sprayed Inconel 718 coatings, *Surf. Coatings Technol.*, vol. 350, pp. 64–73, doi: 10.1016/j.surfcoat.2018.06.080.

[33] **C. S. Ramesh, D. S. Devaraj, R. Keshavamurthy, and B. R. Sridhar**, (2011). Slurry erosive wear behaviour of thermally sprayed Inconel-718 coatings by APS process, *Wear*, vol. 271, no. 9–10, pp. 1365–1371, doi: 10.1016/j.wear.2011.01.057.

[34] **P. K. Koech and C. J. Wang**, (2019). Performance Characteristics of Hot-dip and Plasma Spray Aluminide Coated Nickel-Based Superalloy 718 under Cyclic Oxidation in Water Vapour, *Medziagotyra*, vol. 25, no. 4, pp. 413–421, doi: 10.5755/j01.ms.25.4.21334.

[35] **C. J. Wang and S. M. Chen**, (2006). Microstructure and cyclic oxidation behavior of hot dip aluminized coating on Ni-base superalloy Inconel 718, *Surf. Coatings Technol.*, vol. 201, no. 7 SPEC. ISS., pp. 3862–3866, doi: 10.1016/j.surfcoat.2006.07.242.

[36] **P. K. Koech and C. J. Wang**, (2019). Performance Characteristics of Hot-dip and Plasma Spray Aluminide Coated Nickel-Based Superalloy 718 under Cyclic Oxidation in Water Vapour, *Medziagotyra*, vol. 25, no. 4, pp. 413–421, doi: 10.5755/j01.ms.25.4.21334.

[37] **U. Schulz *et al.***, (2003). Some recent trends in research and technology of advanced thermal barrier coatings, *Aerosp. Sci. Technol.*, vol. **7**, no. 1, pp. 73–80, doi: 10.1016/S1270-9638(02)00003-2.

[38] **G. W. Goward and D. H. Boone**, (1971). Mechanisms of formation of diffusion aluminide coatings on nickel-base superalloys, *Oxid. Met.*, vol. 3, no. 5, pp. 475–495, doi: 10.1007/BF00604047.

[39] **H. W. Grünling and R. Bauer**, (1982). The role of silicon in corrosion-resistant high temperature coatings, *Thin Solid Films*, vol. 95, no. 1, pp. 3–20, doi: 10.1016/0040-6090(82)90578-8.

[40] **N. Eliaz, G. Shemesh, and R. M. Latanision**, (2000). Hot corrosion in gas turbine components, *Eng. Fail. Anal.*, vol. 9, pp. 31–43, Accessed: May 04, 2021. [Online]. Available: www.elsevier.com/locate/engfailanal

[41] **G. W. Goward and D. H. Boone**, (1971). Mechanisms of Formation of Diffusion Aluminide Coatings on Nickel-Base Superalloys, *Oxid. Met.*, vol. 3, no. 5.

[42] **W. T. Griffiths and L. B. Pfeil**, (1937).

[43] **G. W. Goward**, (1998). Progress in coatings for gas turbine airfoils.

[44] **M. C. Galetz**, (2015). Coatings for Superalloys, in *Superalloys*, InTech, 2015. doi: 10.5772/61141.

[45] **R. A. Miller**, Thermal Barrier Coatings for Aircraft Engines: History and Directions.

[46] **B. A. Pint, I. G. Wright, and W. J. Brindley**, (2000). Evaluation of thermal barrier coating systems on novel substrates, *J. Therm. Spray Technol.*, vol. 9, no. 2, pp. 198–203, doi: 10.1361/105996300770349926.

[47] **D. R. Clarke and S. R. Phillpot**, (2005). Thermal barrier coating materials, *Mater. Today*, vol. 8, no. 6, pp. 22–29, doi: 10.1016/S1369-7021(05)70934-2.

[48] **M. Daroonparvar *et al.***, (2013). Improvement of thermally grown oxide layer in thermal barrier coating systems with nano alumina as third layer, *Trans. Nonferrous Met. Soc. China (English Ed.*, vol. 23, no. 5, pp. 1322–1333, doi: 10.1016/S1003-6326(13)62600-X.

[49] **B. M. Warnes**, (2003). Improved aluminide/MCrAlX coating systems for super alloys using CVD low activity aluminizing, *Surf. Coatings Technol.*, vol. 163–164, pp. 106–111, doi: 10.1016/S0257-8972(02)00602-3.

[50] **H. M. Tawancy, N. M. Abbas, and A. Bennett**, (1994). Role of Y during high temperature oxidation of an M-Cr-Al-Y coating on an Ni-base superalloy, *Surf. Coatings Technol.*, vol. 68–69, no. C, pp. 10–16, doi: 10.1016/0257-8972(94)90130-9.

[51] **U. Schulz *et al.***, (2003). Some recent trends in research and technology of advanced thermal barrier coatings, *Aerosp. Sci. Technol.*, vol. 7, no. 1, pp. 73–80, doi: 10.1016/S1270-9638(02)00003-2.

[52] **N. M. Yanar, G. Kim, S. Hamano, F. S. Pettit, and G. H. Meier**, (2014). Materials at High Temperatures Microstructural characterization of the failures of thermal barrier coatings on Ni-base superalloys, doi: 10.1179/mht.2003.058.

[53] **A. K. Ray *et al.***, (2007). Fatigue behavior of a thermal barrier coated superalloy at 800 °C, *Mater. Sci. Eng. A*, vol. 448, no. 1–2, pp. 294–298, doi: 10.1016/j.msea.2006.10.035.

[54] **E. Pauletti and A. S. C. M. d'Oliveira**, (2018). Study on the mechanisms of formation of aluminized diffusion coatings on a Ni-base superalloy using different pack aluminization procedures, *J. Vac. Sci. Technol. A*, vol. 36, no. 4, p. 041504, doi: 10.1116/1.5026272.

[55] **Z. D. Xiang, J. S. Burnell-Gray, and P. K. Datta**, (2001). Aluminide coating formation on nickel-base superalloys by pack cementation process, *J. Mater. Sci.*, vol. 36, no. 23, pp. 5673–5682, doi: 10.1023/ A:1012534220165.

[56] **S. Kumar, B. Satapathy, D. Pradhan, and G. S. Mahobia**, (2019). Effect of surface modification on the hot corrosion resistance of Inconel 718 at 700 °c, *Mater. Res. Express*, vol. 6, no. 8, p. 086549, doi: 10.1088/2053-1591/ab1dc7.

[57] **G. W. Goward and D. H. Boone**, (1971). Mechanisms of Formation of Diffusion Aluminide Coatings on Nickel-Base Superalloys.

[58] **Z. Yu, D. D. Hass, and H. N. G. Wadley**, (2005). NiAl bond coats made by a directed vapor deposition approach, *Mater. Sci. Eng. A*, vol. 394, pp. 43–52, doi: 10.1016/j.msea.2004.11.017.

[59] **R. F. Glória, N. Chaia, A. W. da Cruz, L. B. Alckmin, C. A. Nunes, and G. Rodrigues**, (2021). Aluminide coating on Mar-M246 nickel superalloy by halide activated pack cementation (HAPC), *Surf. Coatings Technol.*, vol. 411, p. 126999, doi: 10.1016/j.surfcoat.2021.126999.

[60] **L. Tong, Y. Dengzun, and Z. Chungen**, (2010). Low-temperature Formation of Aluminide Coatings on Ni-base Superalloys by Pack Cementation Process, *Chinese J. Aeronaut.*, vol. 23, pp. 381–385, doi:10.1016/ S1000-9361(09)60231-4.

[61] **Url-2** < https://www.azonano.com/article.aspx?ArticleID=3427 >, (accessed May 09, 2021).

[62] **M. Yavorska and J. Sieniawski**, (2011). Oxidation behaviour of platinum modified aluminide coatings deposited by CVD method on nickel-based superalloys under air atmosphere Manufacturing and processing Manufacturing and processing. Accessed: May 09, 2021. [Online]. Available: www.journalamme.org

[63] **V. G. Shmorgun, A. I. Bogdanov, V. P. Kulevich, L. D. Iskhakova, and A. O. Taube**, (2021). Microstructure and phase composition of diffusion coating formed in NiCr alloys by hot-dip aluminizing, *Surfaces and Interfaces*, vol. 23, p. 100988, doi: 10.1016/j.surfin.2021.100988.

[64] **W. J. Cheng and C. J. Wang**, (2013). Effect of chromium on the formation of intermetallic phases in hot-dipped aluminide Cr-Mo steels, *Appl. Surf. Sci.*, vol. 277, pp. 139–145, doi: 10.1016/j.apsusc.2013.04.015.

[65] **W. Deqing, S. Ziyuan, and T. Yingli**, (2005). Microstructure and oxidation of hot-dip aluminized titanium at high temperature, *Appl. Surf. Sci.*, vol. 250, no. 1–4, pp. 238–246, doi: 10.1016/j.apsusc.2005.01.002.

[66] **Y. Wang, J. Xiong, J. Yan, H. Fan, and J. Wang**, (2011). Oxidation resistance and corrosion behavior of hot-dip aluminized coatings on commercial-purity titanium, *Surf. Coatings Technol.*, vol. 206, no. 6, pp. 1277–1282, doi: 10.1016/j.surfcoat.2011.08.042.

[67] **G. H. Awan and F. ul Hasan**, (2008). The morphology of coating/substrate interface in hot-dip-aluminized steels, *Mater. Sci. Eng. A*, vol. 472, no. 1–2, pp. 157–165, doi: 10.1016/j.msea.2007.03.013.

[68] **P. Patel, N. I. Jamnapara, A. Zala, and S. D. Kahar**, (2020). Investigation of hot-dip aluminized Ti6Al4V alloy processed by different thermal treatments in an oxidizing atmosphere, *Surf. Coatings Technol.*, vol. 385, p. 125323, doi: 10.1016/j.surfcoat.2019.125323.

[69] **Z. G. Zhang, Y. P. Peng, Y. L. Mao, C. J. Pang, and L. Y. Lu**, (2012). Effect of hot-dip aluminizing on the oxidation resistance of Ti-6Al-4V alloy at high temperatures, *Corros. Sci.*, vol. 55, pp. 187–193, doi: 10.1016/j.corsci.2011.10.029.

[70] **J. R. Nicholls, K. J. Lawson, A. Johnstone, and D. S. Rickerby**, (2002). Methods to reduce the thermal conductivity of EB-PVD TBCs, *Surf. Coatings Technol.*, vol. 151–152, pp. 383–391, doi: 10.1016/S0257-8972(01)01651-6.

[71] **B. Swain, S. Bhuyan, R. Behera, S. Sanjeeb Mohapatra, and A. Behera**, (2021). Wear: A Serious Problem in Industry, in *Tribology in Materials and Manufacturing - Wear, Friction and Lubrication*, IntechOpen, 2021. doi: 10.5772/intechopen.94211.

[72] **M. Shibata, S. Kuroda, H. Murakami, M. Ode, M. Watanabe, and Y. Sakamoto**, (2006). Comparison of microstructure and oxidation behavior of CoNiCrAlY bond coatings prepared by different thermal spray processes, in *Materials Transactions*, Jul. 2006, vol. 47, no. 7, pp. 1638–1642. doi: 10.2320/matertrans.47.1638.

[73] **G. W. Stachowiak**, (2017). How tribology has been helping us to advance and to survive, *Friction*, vol. 5, no. 3. Tsinghua University Press, pp. 233–247, Sep. 01, 2017. doi: 10.1007/s40544-017-0173-7.

[74] **K. Holmberg and A. Erdemir**, (2017). Influence of tribology on global energy consumption, costs and emissions, *Friction*, vol. 5, no. 3. Tsinghua University Press, pp. 263–284, Sep. 01, 2017. doi: 10.1007/s40544-017-0183-5.

[75] **M. T. Devlin**, (2020). Tribology and Wear Modeling and Testing, in *Reference Module in Materials Science and Materials Engineering*, Elsevier, 2020. doi: 10.1016/b978-0-12-819726-4.00056-9.

[76] **Url-3** <https://www.substech.com/dokuwikir>, (accessed Jun. 08, 2021).

[77] **A. S. Khanna**, (2016). Fundamentals of High Temperature Oxidation/Corrosion, *High Temp. Corros.*, pp. 1–31, doi: 10.1142/9789814675239_0001.

[78] **V. Asokan, J. Eklund, S. Bigdeli, and T. Jonsson**, (2021). The influence of Si on the primary protection of lean FeCrAl model alloys in O2 and O2+H2O at 600 °C—A microstructural investigation, *Corros. Sci.*, vol. 179, p. 109155, doi: 10.1016/j.corsci.2020.109155.

[79] **L. Geng, Y. S. Na, and N. K. Park**, (2007). Oxidation behavior of Alloy 718 at a high temperature, *Mater. Des.*, vol. 28, no. 3, pp. 978–981, doi: 10.1016/J.MATDES.2005.11.020.

[80] **S. Cruchley, M. P. Taylor, H. E. Evans, M. C. Hardy, and D. J. Child**, (2014). Characterisation of subsurface oxidation damage in Ni based superalloy, RR1000, *Mater. Sci. Technol. (United Kingdom)*, vol. 30, no. 15, pp. 1884–1889, doi: 10.1179/1743284714Y.0000000541.

[81] **B. GÜLEÇ**, (2019). Effect of diffusion annealing on the surface properties of hot dip aluminized Inconel 718 superalloy, İstanbul Technical University.

[82] **G. H. Awan, F. Ahmed, L. Ali, M. S. Shuja, and F. Hasan**, (2008). Effect of Coating-thickness on the Formability of Hot Dip Aluminized Steel, *Pak. J. Engg. Appl. Sci*, vol. 2.

[83] **J. Zang *et al.***, (2016). Oxidation behaviour of the nickel-based superalloy DZ125 hot-dipped with Al coatings doped by Si, *Corros. Sci.*, vol. 112, no. July 2016, pp. 170–179, doi: 10.1016/j.corsci.2016.07.020.

[84]**S. Rashidi, J. P. Choi, J. W. Stevenson, A. Pandey, and R. K. Gupta**, (2020). High temperature oxidation behavior of aluminized Haynes 230, *Corros. Sci.*, vol. 174, p. 108835, doi:10.1016/J.CORSCI.2020. 108835.

[85] **K. Kishore, S. Chhangani, M. J. N. V Prasad, and K. Bhanumurthy**, (2021). Microstructure evolution and hardness of hot dip aluminized coating on pure iron and EUROFER 97 steel: Effect of substrate chemistry and heat treatment, *Surf. Coat. Technol.*, vol. 409, p. 126783, doi: 10.1016/j.surfcoat.2020.126783.

[86] **S. Bose**, (2017). *High Temperature Coatings*, 2nd ed. 2017.

[87] **T. Sand *et al.***, (2021). Exploring the Effect of Silicon on the High Temperature Corrosion of Lean FeCrAl Alloys in Humid Air, *Oxid. Met.*, doi: 10.1007/s11085-020-10019-2.

[88] **F. Aydin, A. Ayday, M. E. Turan, and H. Zengin**, (2019). Role of graphene additive on wear and electrochemical corrosion behaviour of plasma electrolytic oxidation (PEO) coatings on Mg–MWCNT nanocomposite, *https://doi.org/10.1080/02670844.2019.1689640*, vol. 36, no. 8, pp. 791–799, doi: 10.1080/02670844.2019.1689640.

[89] **A. Günen, K. M. Döleker, M. E. Korkmaz, M. S. Gök, and A. Erdogan**, (2021). Characteristics, high temperature wear and oxidation behavior of boride layer grown on nimonic 80A Ni-based superalloy, *Surf. Coatings Technol.*, vol. 409, p. 126906, doi: 10.1016/J.SURFCOAT. 2021.126906.

[90] **Q. Y. Zhang *et al.***, Wear Behavior and Mechanism of Fe-Al Intermetallic Coating Prepared by Hot-Dip Aluminizing and Diffusion, *Metall. Mater. Trans. A*, vol. 47, doi: 10.1007/s11661-016-3414-x.

[91] **I. Ganesh and I. Advanced**, (2016). Correlation between the characteristics of the mechanically mixed layer and wear behaviour of aluminium , Al-7075 alloy and Al-MMCs and wear behaviour of aluminium , Al-7075 alloy and Al-MMCs, *Wear*, vol. 245, no. July, pp. 22–38.

[92] **J.-M. Brossard, J. Balmain, F. Sanchette, and G. Bonnet**, (2005). High-Temperature Oxidation of an Aluminized NiCr Alloy formed by a Magnetron-Sputtered Al Diffusion Coating, *Oxid. Met. 2005 641*, vol. 64, no. 1, pp. 43–61, doi: 10.1007/S11085-005-5705-2.

CURRICULUM VITAE

Name Surname : Ahmet KAVUKCU

EDUCATION

- **B.Sc. : 2013-2018** Yıldız Technical University, *Metallurgy and Material Engineering*
- **M.Sc. : 2018-2020** İstanbul Technical University, *Materials Engineering*

PROFESSIONAL EXPERIENCE

- **01.2020 - Still :** Gebze Technical University – *Research Assistant*